Jagiellonian University
Faculty of Physics, Astronomy and Applied Computer Science

DOCTORAL THESIS

Feasibility study of lesion detection by means of Total-Body Jagiellonian Positron Emission Tomography scanner

Author:
Meysam Dadgar

Supervisor:
Prof. Dr. Hab. Paweł Moskal

Kraków
October, 2022

Declaration

Wydział Fizyki, Astronomii i Informatyki Stosowanej, Uniwersytet Jagiellonski ´

Oswiadczenie ´

Ja nizej podpisany Meysam Dadgar doktorant (nr indeksu:1161055) ˙ Wydziału Fizyki, Astronomii i Informatyki Stosowanej Uniwersytetu Jagiellonskiego oświadczam, że przedłożona przeze mnie rozprawa doktorska pt. „Assesment of lession detection by means of Total-Body J-PET Jagiellonian Positron Emission Tomography scanner", jest oryginalna i przedstawia wyniki badań wykonanych przeze mnie osobiście, pod kierunkiem prof. dr. hab. Pawła Moskala. Prace napisałem samodzielnie. Oświadczam, że moja rozprawa doktorska została opracowana zgodnie z Ustawą o prawie autorskim i prawach pokrewnych z dnia 4 lutego 1994 r. (Dziennik Ustaw 1994 nr 24 poz. 83 wraz z ́óźniejszymi zmianami).

Jestem świadom, że niezgodność niniejszego oświadczenia z prawdą ujawniona w dowolnym czasie, niezaleznie od skutków prawnych wynikających z ww. ustawy, może spowodować unieważnienie stopnia nabytego na podstawie tej rozprawy.

Author: Meysam Dadgar

Signed:

Acknowledgements

First of all, I would like to express my gratitude to Professor Pawel Moskal, who, like a compassionate and kind person, supported me during my Ph.D. study.

He turned my experience as a doctoral student in the J-PET group into a unique position in academic life by providing unlimited research equipment and financial support. I appreciate all those moments he was there to support me and make me a better version of myself in science.

I want to thank my dear friend and colleague, Mr. Szymon Parzych, who was motivating me with excellent ideas for the research and was helping me with his kind heart.

I would also like to thank my all colleagues from the J-PET collaboration: Dr. Baran, Dr. Czerwiński, Dr. Dulski, Dr. Gajos, Dr. Kaplon, Dr. Krzemien, Dr. Niedzwiecki, Dr. Sharma, Dr. Perez del Rio, Dr. Shopa, Dr. Skurzok, Dr. Curceanu, S. Shivani and K. Tayefi Ardebili. I thank all of them for their companionship and for providing a friendly work atmosphere.

Most importantly, I dedicated this work to my beloved spouse Ms. Faranak Tayefi Ardebilli, who has been and will remain my only love and companion in my personal and academic life. I was lucky to have her with my self as colleague in J-PET collaboration as well. She is a strong and passionate wife, a kind mother, and a hard-working colleague who always encouraged me on the path of excellence in life. I am grateful for her presence and the life she gave to Diana, my sweet daughter, and the reason for my happiness.

My special thanks will go to my mother and father; being far from them was difficult for all of us, but they supported me with their kind hearts.

This work was supported by Foundation for Polish Science through TEAM POIR .04.04.00 − 00 − 4204/17, the National Science Centre, Poland (NCN) through grant No. 2021/42/A/ST2/00423, PRELUDIUM 19, agreement No. UMO − 2020/37/N/NZ7/04106. The work also has been supported by a grant from the SciMat and qLife Priority Research Areas under the Strategic Programme Excellence Initiative at the Jagiellonian University.

Abstract

Metastasis as the major reason for 90 % of cancer-related deaths, occurs when cancerous cells detach from their primary tissue and spread to the other part of the body through blood vessels or the lymphatic system. Detection of these malignant lesions in their early stages can increase the patient's survival rate by taking proper treatment strategies. Due to their low sensitivity, conventional PET scanners cannot detect metastatic lesions in the early stages.

In 2019, a new Total-Body PET (TB PET) scanner called uEXPLORER with higher sensitivity thanks to the full detector coverage along the patient's body was constructed. The main obstacle in the worldwide utilization of this generation of scanners is their higher construction and maintenance price. Since 2013, there has been continuous research to develop a novel economic type of PET scanner named Jagiellonian Positron Emission Tomography (J-PET) based on plastic scintillators. This technology, by providing a cost-efficient solution in the construction of the Total-Body PET scanners opens possibilities for worldwide utilization of these systems and improves the survival rate of patients significantly with precise diagnosis. The research presented in this thesis evaluated the lesion detectability of Total-Body J-PET scanners by accomplishing the GATE simulation from XCAT anthropomorphic digital phantoms. This thesis's main aim is to investigate the lesion detectability of the Total-Body J-PET scanner and improve this feature by optimizing event selection criteria and the spatial resolution of the tomograph. The liver is the organ under study to determine the lesion detectability of Total-Body J-PET.

For the case of the presented thesis, a series of simulations with point sources and cylindrical phantoms has been performed for the determination of optimum characteristics of Total-Body J-PET. The second group of the simulations has been performed by utilization of human-grade XCAT anthropomorphic phantoms. The results of the simulations have been analyzed by Gate Output J-PET Analyzer (Goja) which has been developed by the J-PET collaboration. Due to the unique configuration of the J-PET-based scanners and their special detection principle, conventional image reconstruction software could not be compatible. In the case of the image reconstruction Quantitative Emission Tomography Iterative Reconstruction (QETIR) in collaboration with the Medisip research group from Gent, Belgium has been used.

The results showed that the Total-Body J-PET tomograph can detect centimeter-grade lesions in the various ranges of the XCAT phantoms with different body mass index (BMI). However applying acceptance angle criteria to remove the contribution of the most oblique coincidences in the image reconstruction, provided the possibility of detecting sub-centimeter (5mm) lesions in a higher number of the iterations of image reconstruction.

Contents

List of Tables

1 Introduction

The aim of this thesis is to assess the detectability of the lesions by means of the cost-effective Total-Body PET scanner based on plastic scintillators [1–5].

Metastasis as the major reason for 90 % of cancer-related deaths, occurs when cancerous cells detach from their primary tissue and spread to the other part of the body [6]. This transmission proceeds via the circulatory system or lymphatic vessels [7]. Larger lesions can be diagnosed based on their symptoms or by means of non-invasive clinical-imaging modalities such as MRI, CT, and PET scans. Contrast-enhanced MRI is typically the preferred choice because of its higher sensitivity and specificity; PET/CT, which is highly accessible and has lower operating costs, is used more widely [8]. Although these imaging modalities can detect large lesions caused by metastases, they are not offering the necessary sensitivity to detect smaller lesions that are in their early stages.

Localizing lesions in organs helps plan personalized treatment procedures to achieve the best results for the patient. A new Total-Body PET (TB PET) scanner was designed and constructed at California University (USA), the first TB PET scanner with 2m axial FOV, called EXPLORER [9]. It can cover the whole patient's body at once and has a sensitivity that is 40 times larger than current clinical PET scanners. Utilization of this generation of PET scanners provides the possibility for accurate and personalized diagnosis as the essential steps for successful treatment procedures. [10].

The main constraint of TB PET scans such as EXPLORER is the construction cost of these scanners, which limits public accessibility [11]. Since 2013, there has been continuing research to develop a novel type of PET scanner named, Jagiellonian Positron Emission Tomography (J-PET). J-PET technology is based on plastic scintillator strips arranged parallel with the axial axis of the scanner, where each end of the strip is equipped with SiPM [3]. Exclusive principle of detection, the arrangement of SiPM, and electronic readouts alongside plastic scintillators make it possible to extend axial FOV without adding any detection modules, just by increasing the length of the plastic scintillator to prepare the large area of detection. Total-Body J-PET, as the newest prototype of J-PET technology, will provide 2m axial FOV [1].

In this thesis, a series of simulations with the GATE software has been performed to assess the lesion detectability of Total-Body J-PET. GATE is software used to simulate interactions between radiation and matter [12]. It is well adapted to nuclear medicine imaging principles and widely simulates a set of tomography geometries with various sources and phantoms, such as XCAT digital phantoms [13].

The XCAT anthropomorphic phantom has been developed to provide virtual patients with medical imaging. Users can define numerous parameters to create normal and abnormal anatomical and motion variations to generate patient populations for medical imaging research [13]. In the presented thesis, studies of lesion detectability are performed. As the example, the liver has been

chosen to investigate the lesion detectability of Total-Body J-PET. due to the high mortality rate of liver cancer-related death. To achieve this goal, characteristics of the J-PET technology in view of small lesion detection as an essential early diagnostic indication will be elaborated. For this case lesions with 5 mm (as small lesions), 10 mm (as minimum considerable dimensions for lesions in clinics), and 20 mm (as the large lesions) with 8:1 amounts of activity in comparison to the background tissue, will be investigated.

The main aim of this research is to determine J-PET lesion detection characteristics as a function of properties of detectors such as the configuration of the scanner, cross-section of the plastic strips, axial and radial position resolution, lesion size, and the patient's body mass index (BMI). For this case, the first set of the simulation was performed to determine optimal detector parameters. By fixing the condition, lesion detectability of the Total-Body J-PET is investigated by XCAT anthropomorphic phantoms. Figure 1 is a schematic illustration of the workflow conducted to investigate the first group of simulations.

Due to the specific arrangement of the detector with multilayer geometry in the TB J-PET scanner, the currently available image reconstruction software could not be used to reconstruct images with this geometry. For this reason, we are developing a new image reconstruction software (called QETIR) in collaboration with Medisip Ghent University Hospital [14].

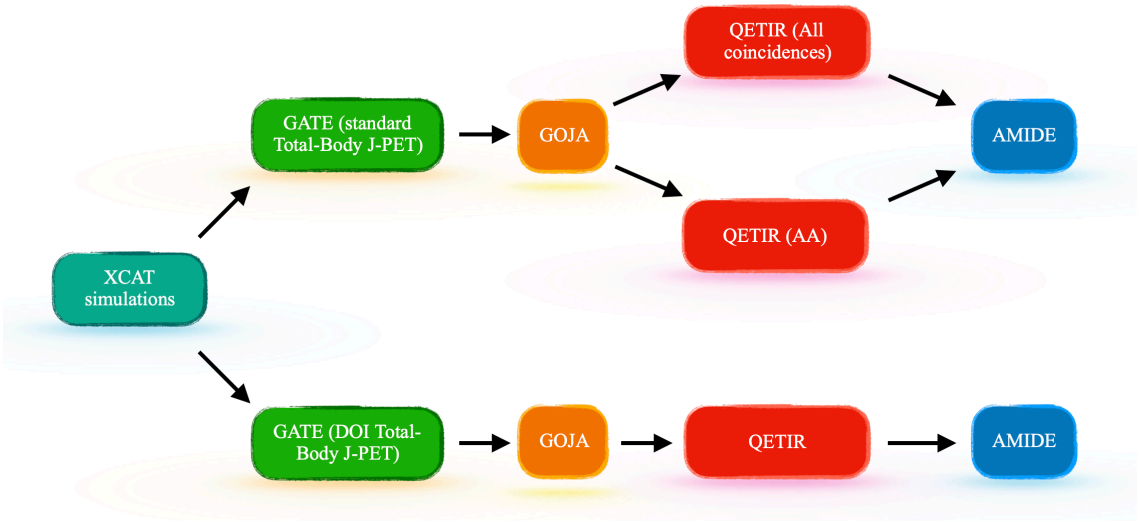

Figure 1: A schematic illustration of the workflow of performed simulations image reconstruction and analysis. The electron-positron annihilation density distribution in the patients was simulated using XCAT software. The emitted gamma photons from the simulations of the tomograph have been performed using the GATE package. The simulated data were analyzed by means of GOJA software. As a result, the list-mode including the position and time of the gamma photons was generated. The selected list-mode data were used to reconstruct images by QETIR software. The reconstructed images were visualized by Amide software.

In the presented thesis, two groups of investigations have been performed, first to determine optimum characteristics of the Total-Body J-PET, then lesion detectability of aforesaid scanner by XCAT anthropomorphic phantoms as shown in Figure 1. To determine the optimum acceptance angle cut in the Total-Body J-PET, 10 series of simulation has been performed. Each of the outputs has been analyzed with 11 different analysis conditions. From the results of each separate analysis, list-mode data has been extracted and the 24 number of the reconstruction has been performed for each one of them. After fixing the condition of Total-Body J-PET, five XCAT phantoms have been chosen to investigate the lesion detectability of the Total-Body J-PET. The lesion detectability of Total-Body J-PET has been determined by the analysis of 126 reconstructed images of XCAT phantoms.

The basics of cancer and its classification are described in Chapter 2, where the anatomy and physiology of the liver, oncological abnormalities, and its diagnostic methods as an organ of the study have been characterized. The principle operations of the J-PET technology and its advantage as a promising alternative for conventional tomographs are described in Chapter 3. The simulation toolkit, event selection criteria, and characteristics of the utilized XCAT phantoms are described in Chapter 4. The results obtained in this simulation-based study have been presented in Chapter 5. The conclusion of the proposed simulation-based study and methods to enhance lesion detectability of the Total-Body J-PET are described in Chapter 6.

Author contribution:

It is relevant to describe in this thesis the articles with the main contribution of the author of the thesis. In those articles (1st-6th), preparation of the simulations, image reconstructions, and processing has been performed by the author of the thesis.

During the past four years of the Ph.D. study, the author of the thesis also contributed as the co-author (articles listed as 7th- 14th) in the data analysis/ image reconstruction/ performing GATE simulations.

1. **M. Dadgar**, et al. ”Comparative studies of the sensitivity of sparse and full geometries of Total-Body PET scanners built from crystals and plastic scintillators” submitted to EJNMMI Physics, 2022.

2. **M. Dadgar**, F. Tayefi Ardebili, et al., ”Simulation based investigation of the DOI capable Total-Body J-PET in the framework of the parallax issue,” submitted to in IEEE Transactions on Radiation and Plasma Medical Sciences, 2022.

3. **M. Dadgar**, S. Parzych and F. Tayefi Ardebili, ”Introduction of the DOI capable Total-Body J-PET, a simulation study,” Journal of Nuclear Medicine, 63 (supplement 2) 3316, June 2022.

4. **M. Dadgar**, S. Parzych and F. Tayefi Ardebili, et al., ”Investigation of novel preclinical Total Body PET designed with J-PET technology: A simulation study,” in IEEE Transactions on Radiation and Plasma Medical Sciences, 2022.

5. **M. Dadgar**, S. Parzych and F. Tayefi Ardebili, ”A Simulation Study to Estimate Optimum LOR Angular Acceptance for the Image Reconstruction with the Total-Body J-PET” Lecture Notes in Computer Science 12722 (2021) 189-200.

6. **M. Dadgar**, P. Kowalski ”Gate simulation study of the 24-module J-PET scanner: data analysis and image reconstruction” Acta Phys. Pol. B 51 (2020) 309.

7. P. Moskal, ..., **M. Dadgar** et al. ”Positronium imaging with the novel multiphoton PET scanner”, Science Advances 7(2021) eabh4394.

8. P. Moskal, ..., **M. Dadgar** et al. ”Testing CPT symmetry in ortho-positronium decays with positronium annihilation tomography” Nature Communications 12 (2021) 5658.

9. P. Moskal, ..., **M. Dadgar** et al. ”Simulating NEMA characteristics of the modular total-body J-PET scanner - an economic total-body PET from plastic scintillators” Phys. Med. Biol. 66 (2021) 175015.

10. K. Dulski, ..., **M. Dadgar** et al. ”The J-PET detector-a tool for precision studies of ortho-positronium decays” Nuclear Inst. and Methods in Physics Research, A 1008 (2021) 165452.

11. R. Shopa, ..., **M. Dadgar** et al. ”Optimisation of the event-based TOF filtered back-projection for online imaging in total-body J-PET” Medical Image Analysis 73 (2021) 102199.

12. P. Moskal, ..., **M. Dadgar** et al. ”Synchronisation and calibration of the 24-modules J-PET prototype with 300 mm axial field of view” IEEE Transactions on Instrumentation and Measurement 70 (2021) 2000810.

13. P. Moskal, ..., **M. Dadgar** et al.” Performance assessment of the 2gamma positronium imaging with the total-body PET scanners” EJNMMI Phys. 7 (2020) 44.

14. S. Sharma, ..., **M. Dadgar** et al.” Estimating relationship between the Time Over Threshold and energy loss by photons in plastic scintillators used in the J-PET scanner”EJNMMI Phys. 7 (2020) 39.

2 Basic of the cancer and its classification

2.1 Cancer

Cancer, known as one of the main reasons of death worldwide, originates from failure during cell duplication procedures [15]. Cells can be introduced as the smallest living structure in the body, and their accumulation forms tissue and organs [7]. According to its natural physiology, the human body constantly generates new cells while older cells fall in their mortality cycle. This process is a part of the body's normal physiology for repairing and growing [16].

According to the aforesaid continuous duplication process, the production of any abnormal cells can provide the possibility of duplication of a series of cells with abnormality. The accumulation of dedicated cells in an organ creates an object called a tumor [17]. There is many reasons for such abnormal cell production cycle, such as family history, alcohol, smoking, lack of physical activity, inappropriate living style, etc. Involving the person with one or more parameters mentioned above will not lead to cancer necessarily, but they can boost the probability by affecting the human body's immune system [18].

The tumors can have different physiology, such as growth rate and pattern, differentiation from background tissue, etc. Based on these characteristics, tumors can be classified into two groups: benign and malignant [19].

2.1.1 Benign tumor

Benign tumors refer to masses of abnormally duplicated cells with slow-growing patterns and differentiable structures from surrounding tissue. These tumors, categorized as noncancerous tumors, are noninvasive and remain in their primary location without spreading to other organs (Figure 2). In most cases, a patient with a benign tumor has no symptoms. These tumors are primarily diagnosed for some unrelated reasons during ultrasound or radiography [20].

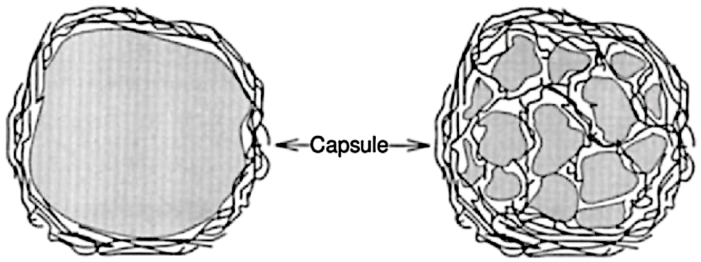

Figure 2: Schematic illustration of the benign tumor in a capsulized shape, including a single lesion (left) and multiple lesions (right). The figure is adopted from [21].

While benign tumors do not show aggressive behavior, in some cases, if the treatment is not

performed, they can spread to the body's other organs. Depending on the hosting organ of the benign tumor, the specialist decides what type of treatment is necessary. Surgery is the most common procedure of treatment for benign tumors [22].

2.1.2 Malignant tumor

Malignant tumors refer to tumors with aggressive behavior and a fast growth rate. The structure of their textures is indistinguishable in very early cases, reducing the chance of diagnosing the malignant tumor in irrelevant examinations [23]. They can involve nearby tissue or spread into the farther organs in the body under the procedure known as metastasis [24]. A schematic illustration of the formation of a malignant lesion and its spread to other organs via the blood vessels system is shown in Figure 3 [25].

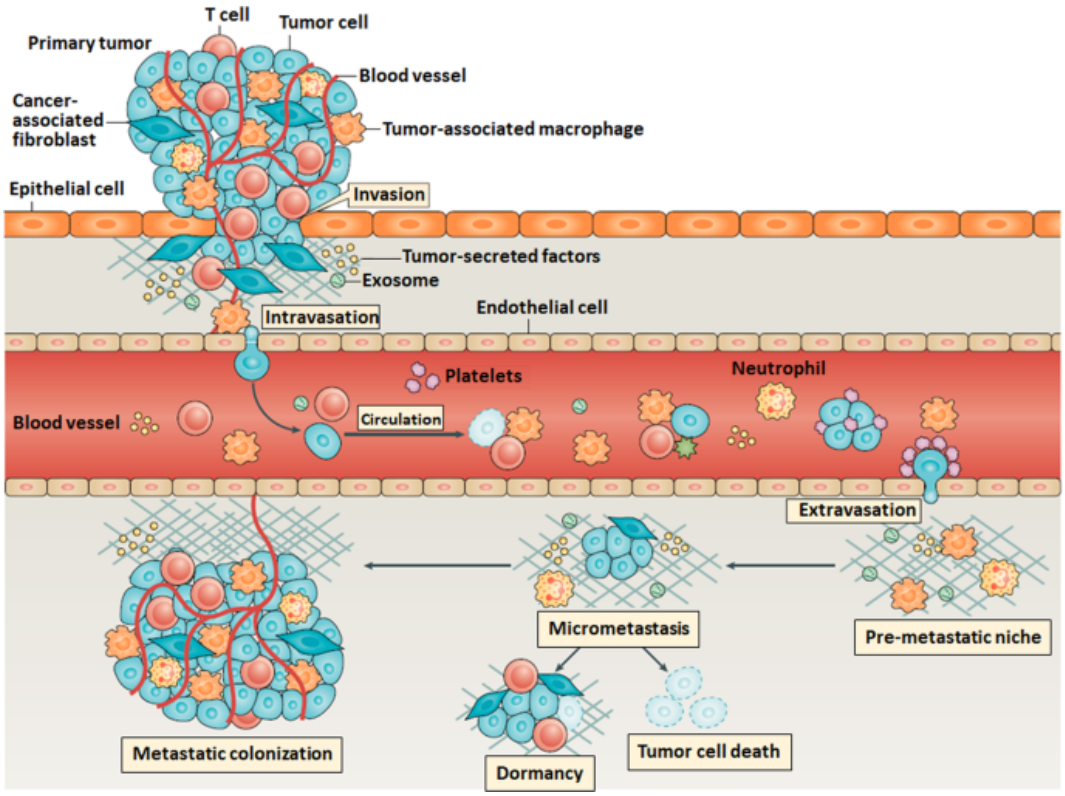

Figure 3: Schematic illustration of the malignant lesion formation and its spread to other body organs via blood vessels. The figure is adopted from Reference [25].

Malignant tumors are categorized as those which can cause cancers in the patient body. Usually, specialists simultaneously apply hybrid treatment strategies, such as surgery and chemotherapy [26].

2.1.3 Type of the cancers

Cancer in each organ can be classified depending on the origin of cancer. There is 2 group of cancers, primary and secondary. Primary cancers in each specific organ refer to the condition that occurs in that organ for the first time. Diagnostic of the primary cancers can enhance the patient's survival rate due to the possibility of a positive body response to a wide range of treatment planning.

Secondary cancers, as the consequence of the metastasis from different organs, result in growing of the tumor in another organ [27].

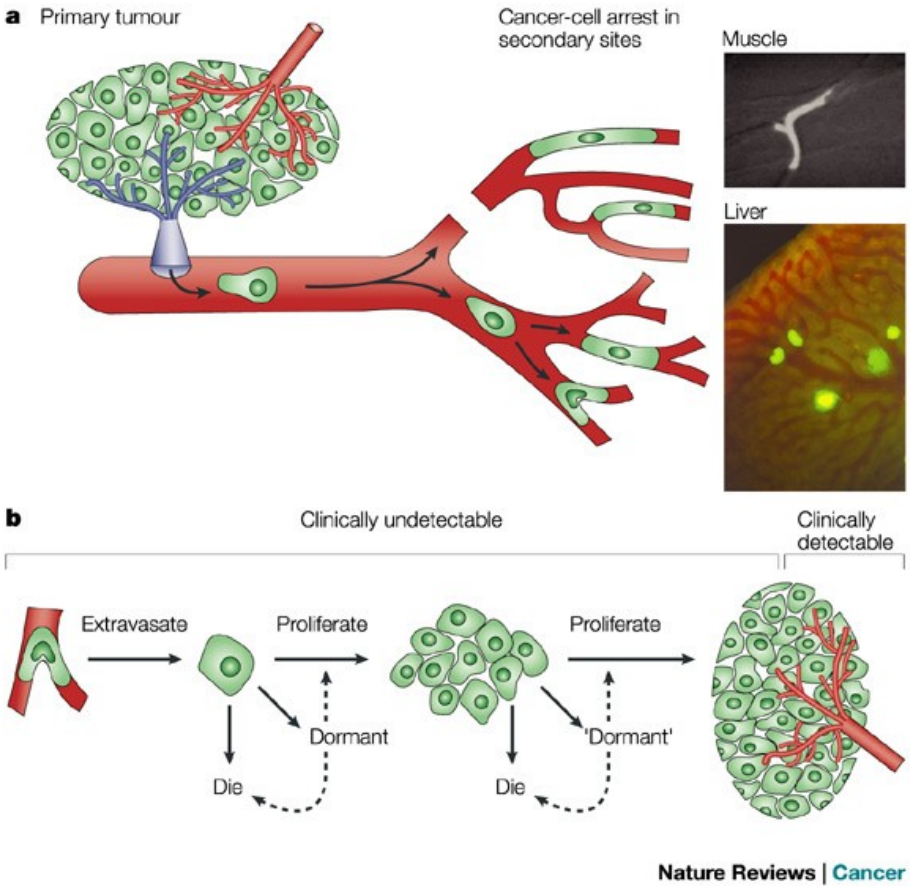

Figure 4: Schematic visualization of the (a) primary malignant tumor and breaking down in its structure and spreading via blood vessels. (b) These cells host in other organs and form lesions categorized as secondary tumors. The figure is adopted from Reference [28].

Secondary cancer usually has been observed in cancer survivors, particularly in pediatric patients and young adults with long life expectancy's who have been already treated for cancers [29]. This group of patients needs frequent whole-body monitoring for early diagnosis of any possible tumors. The main worldwide obstacle to precise and routine monitoring is the cost of performing corresponding diagnoses.

2.1.4 Tumor grading

Tumors depend to their characteristics such as host organ, shape, size etc., have various behaviour. This divergent emphasize on the importance of determination of a metric to categorize them. Tumor grading are used to predict lesions behaviour and apply proper treatment planing by exchanging the knowledge between the clinics [30]. Figure 5 is an exemplary grading diagram showing the cells' structure in each different phase. The G1 where the normal cells with a major population have a uniform structure in the tissue. From the G2 stage, the abnormal cells change their shape and distribution of the cells. This procedure continues up to G5 where the abnormal cells become a major population and affect the physiology of the tissue and organ.

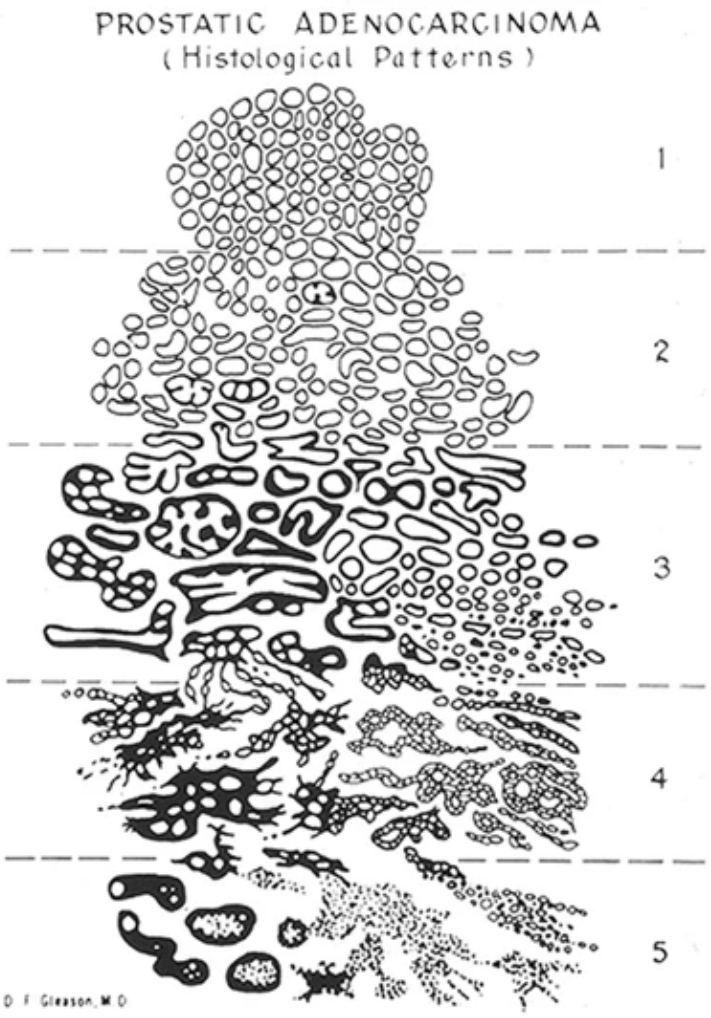

Figure 5: An exemplary grading diagram of histological pattern of prostate adenocarcinoma that structure of the cells changes in each different level. The figure is adopted from Reference [31].

2.2 Liver

As a vital organ in the vertebrate body, the liver is responsible for several physiological processes, including strengthening the immune system, clearing the blood of toxins, and actively participating in the digestive system [32]. Furthermore, the liver is the glucose storage source in the form of glycogen, which can provide the human body's energy during the necessary fasting [33]. One of the essential functions of the liver is the production of bile, which, by breaking parts of the fats, facilitates their digestion [34]. One of the unique features of the liver is its self-healing ability. This organ can growth even with 20% of its volume and form a normal size liver.

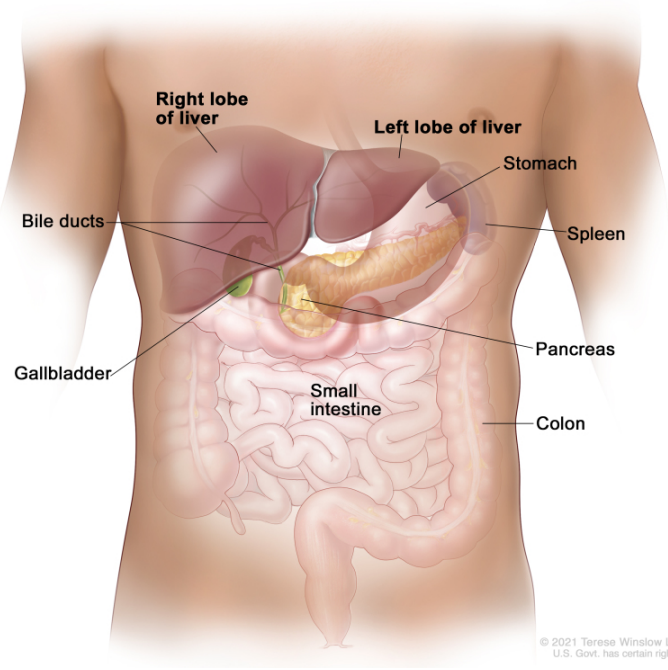

Figure 6: Schematic illustration of the liver in thorax cavity and nearby organs. The figure is adopted from Reference [35].

The contribution of the liver to a wide range of essential physiology of the human body and its location in contact with other organs in the abdominal cavity has caused exposure to a wide range of diseases. According to the importance of the liver in the body, recognizing its exact structure and physiology and the organs and blood vessels connected to it can speed up accurately diagnosing possible abnormalities [36].

2.2.1 Anatomy of the liver

The liver, as the largest organ in the body, has an asymmetrical structure due to its position in the upper part of the abdominal cavity. The liver is located in the upper part of the abdominal cavity

near the diaphragm, and its other surfaces are next to the visceral organs [37, 38]. The movement of the diaphragm during inhalation and exhalation affects the position of the liver.

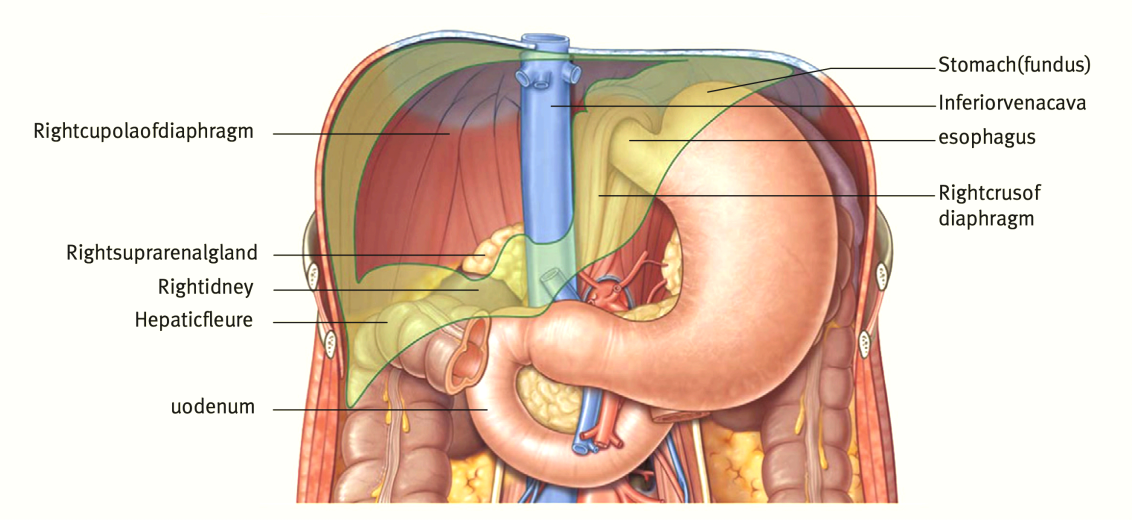

Figure 7: A detailed schematic illustration of the liver's nearby organs. The figure is adopted from Reference [38].

The liver is generally divided into left and right lobes, which have veins and arteries. These lobes are distinct by eight sections with independent vessels and arteries. This unique feature allows regrowth after partial liver removal surgery [38].

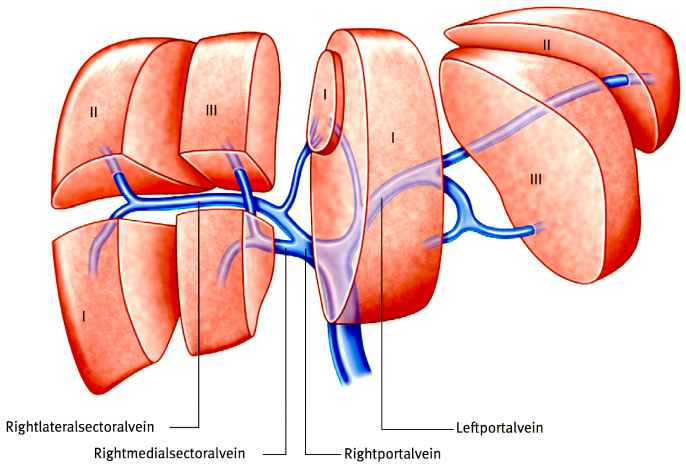

Figure 8: The segmental anatomy of the liver and corresponding vessels. The figure adopted from Reference [38].

2.2.2 Physiology of the liver

The liver is a critical organ responsible for various functions such as the immune system, glucose storage, digestive system, etc. Its wide range of metabolism causes a connection via the metabolic network with many organs in the human body [39].

Any functional defect due to illness can threaten a person's health. This fact emphasizes the importance of monitoring in the early detection of any abnormality in the liver anatomy and physiology.

2.2.3 Common disease of the liver

Any disorder in the liver's functionality significantly influences other body organs and the patient's general health condition. According to the breathing pattern and novel precise diagnosis devices, the number of patients diagnosed with liver issues is increasing [40]. Among the various diseases that affect the liver, fatty liver, alcoholic liver disease, and carcinoma in liver cells can be mentioned as the most common.

2.3 Tumors

Cell proliferation is a part of the standard organ cycle, in which new cells are replaced in the tissue. Abnormal growth and proliferation of cells can lead to the formation of dense tissue from these defective cells, called a tumor. The liver, the largest endocrine gland in the human body, is made up of several different types of cells, each one of which can cause a tumor if it multiplies abnormally [41].

In general, tumors can be categorise into two types, benign and malignant, which have different invasive patterns depending on the type and origin of their formation. Diagnosis of the type of the tumor and determination of its origin is vital in obtaining treatment planning [42].

2.3.1 Tumors in the liver

In addition to whether the tumor is benign or malignant as the general classification, other components can be crucial in choosing the diagnosis method, appropriate treatment planning, and periodic patient care monitoring. The most important of these characteristics are histological grade and tumor stage. Benign tumors can generally result from liver repair in response to injury or abnormal growth of neoplastic cells. These tumors can form all over the liver and even in the bile ducts and are known as non-invasive tumors [43].

Nowadays, the incidence of benign liver tumors is increasing due to the widespread use of imaging techniques, such as ultrasound. The most common kinds of benign liver tumors are heman-

giomas, focal nodular hyperplasia (FNH), and hepatic adenoma (HCA). The benignity of tumors can be determined using biopsy or advanced imaging techniques. The diameter of benign tumors can vary from 1 cm to 10 cm. While these tumors are often asymptomatic, early action against them in susceptible patients، can prevent them from becoming aggressive [44].

2.4 Diagnostic tools of livers tumor

The liver in cancerous patients is known as a high-risk organ for the formation of tumors due to its anatomy and multi-task physiology. Malignant tumors can be formed in the liver or due to metastasis from other organs such colon, breast, etc. In these patients, frequent monitoring methods of the liver for diagnosis of any malignant lesion, such as positron emission tomography (PET), magnetic resonance imaging (MRI), computed tomography (CT), is recommended [45]. In the following, the advantages and disadvantages of each of the methods mentioned above will be explained by considering their reliability in monitoring high-risk patients.

2.4.1 Computed Tomography scan

Computed tomography, an imaging modality based on X-ray radiation, is one of the most commonly used imaging systems for various diseases. Transmission X-rays are attenuated due to their interaction with matter. The non-uniform structure of the body caused different attenuation based on the parameters such as the density of the tissue [46]. The CT scan, by performing 360-degree projection from the patient's body, can generate a high-quality image from the inner organs of the human body [47, 48].

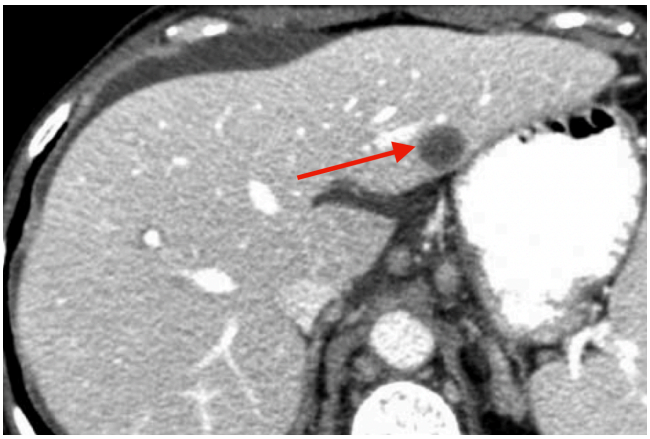

Figure 9: An example CT scan of a liver with an abnormal lesion (pointed with a red arrow). Figure adopted from the Reference [48].

CT scan is a reliable diagnostic technique that operates with a low dose. It is able to detect lesions with a minimum diameter of 2-3 mm, but the main disadvantage of this method is the inability to

provide accurate physiological images that makes benign and malignant tumors indifferent to each other [49]. Figure 9 illustrates a CT scan of the liver while an abnormal lesion (pointed with a red arrow) is visible. Due to the lack of the lesion's physiological data, specialists recommend follow-up diagnosis with other imaging modalities.

Although methods such as CT scans provide the possibility of performing imaging by utilization of contrast agent substance to differentiate benign tumors from malignant lesions, due to the presence of the iodine in this material, it causes nephrological side effects in cancerous patients [48].

2.4.2 Magnetic Resonance Imaging

MRI is a non-invasive imaging method that is a suitable imaging modality for frequent patient monitoring due to the lack of ionizing radiation during the imaging process. Dissimilar to a CT scan that uses X-rays, the MRI utilized a strong external magnetic field around the patient's body, which does not have the side effects of ionizing radiation [50]. Figure 10 shows an example MRI image from a liver including a tumor (pointed with a red arrow).

Although MRI imaging does not have side effects caused by ionizing radiation, it has unique risks for operators and patients.

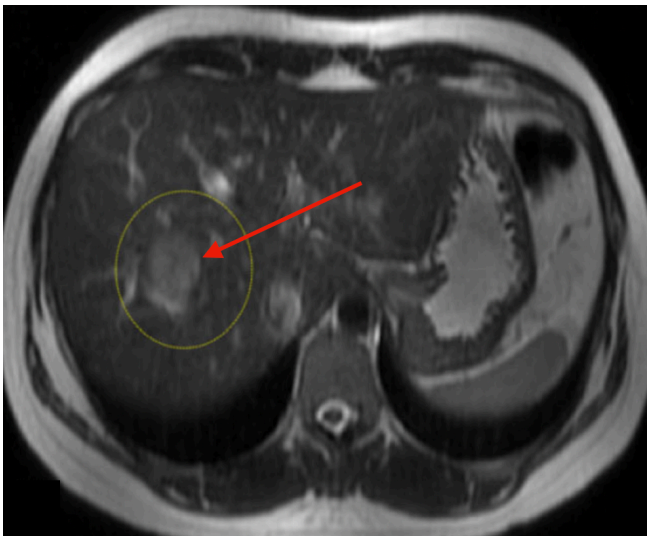

Figure 10: An MRI image of a patient with a considerable lesion in the liver marked with a red arrow.

In patients with an implant or a pacemaker in their body, performing an MRI scan can cause risks such as displacement of the implants and heating the tissue around them, as well as affecting the performance of the pacemaker [51]. However, MRI can provide high-quality images to detect tumors with sub-centimeter dimensions (5 mm lesions), which can provide necessary information about the progress of the disease by performing periodic monitoring [52]. Contrary to the

advantages of MRI, due to its weakness in accurately distinguishing malignant lesions from benign tumors, patients diagnosed with abnormalities are referred to perform other scans, including physiological data.

As mentioned, alongside the advantages of the aforementioned imaging modalities (CT and MRI), these scanners have challenges in detecting oncological abnormal lesions. However, the conventional PET scanners in clinics are a hybrid generation combined with this scanner, such as PET/CT and PET/MRI. The PET scanners, by taking advantage of MRI and CT in the hybrid modalities, broaden their applicability in a wide range of diagnosis fields.

2.4.3 Positron Emission Tomography scan

Positron Emissions Tomography (PET) scan is a molecular imaging modality based on detecting the pair of gamma photons originating from the annihilation of the positron and electron. As a significant part of the imaging procedure, this device, which starts with the injection of the radiopharmaceutic into the patient's body, plays an essential role in diagnosing oncological abnormalities, cardiovascular disease, psychological studies, etc [53]. Figure 11 shows a mass of the malignant tumor in the liver marked by the red arrow.

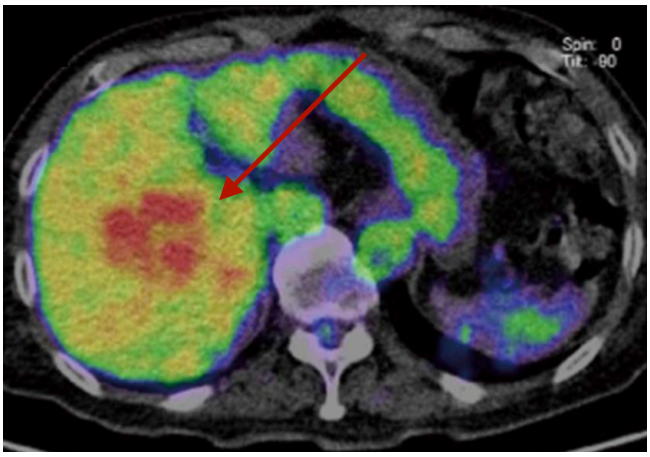

Figure 11: PET images from the liver of a patient with a malignant tumor marked by the red arrow. PET images, by providing physiological pictures of the organs, can differentiate malignant lesions from benign tumors.

The unique features of PET not only have given it a particular function as a diagnostic tool but also caused its wide application in preclinical research on small animals. This issue is essential since it allows researchers to conduct more detailed studies to investigate the performance of various types of radiopharmaceuticals and improve their efficiency for clinical applications. Alongside all privileges of the PET scan, enhancement of the performance of this imaging system for precise diagnosis both from hardware and software points of view has become a hot topic in the nuclear

imaging society [3]. Before addressing this topic, for an accurate understanding of this imaging system, the configuration and principle of operation of PET scan and the function of the radio-pharmaceutics will be discussed.

3 Basic of Positron Emission Tomography

Positron emission tomography consists of series of functions in which the PET device is the central part. In molecular imaging facilities, this procedure begins with the production of the radioizotope by a cyclotron and leads to image reconstruction as the final step. The radiopharmaceutical substance is distributed in the patient body and contributes to the physiology of the cells due to the presence of glucose in its structure. The emitted positron from the radionuclide is annihilated with an electron from surrounding tissue into two 511 KeV gamma photons [54].

As shown in Figure 12 according to the principle of conservation of momentum, gamma photons move away from each other at an angle of 180 degrees. Detection of these photons allows for determining where annihilation of the electron and positron pair occurred.

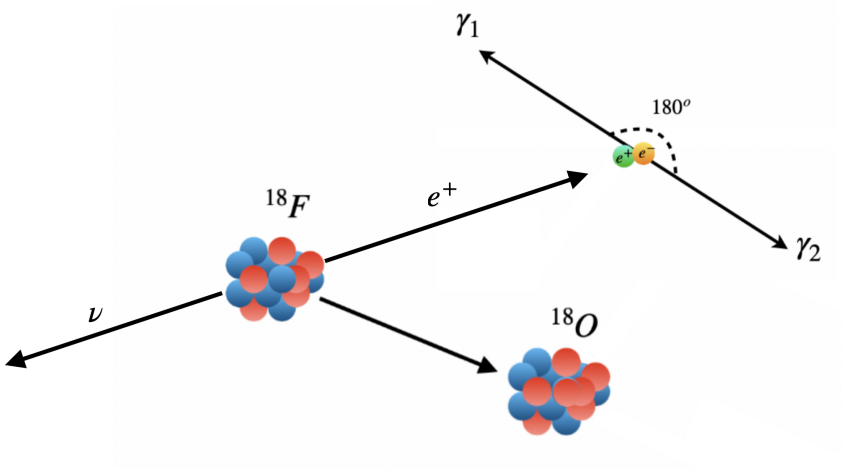

Figure 12: Schematic illustration of the ^{18}F decays by emission of positron particle (green).The blue and red circles indicates protons and neutrons, respectively. Positron interacts with an electron (yellow) according to the pair annihilation process and emits two gamma photons with an energy of 511 KeV.

These 511 keV gamma photons are being detected due to their interaction with matter. Gamma photons with 511 keV, as high frequent ionization radiation, interact with the matter predominantly by Compton and photoelectric effect. The virtual line, which connects two interaction point, called the line of response (LOR), represent all possible place for allocating annihilation (Figure 13).

3.0.1 Components of PET scanner

The PET scan generally consists of 3 main components: gantry, patient bed, and data acquisition system (DAQ). Each of the parts above comprises several sub-structure with an essential role in PET scanning. Gantry is the host of the detector units known as the main part of the tomograph.

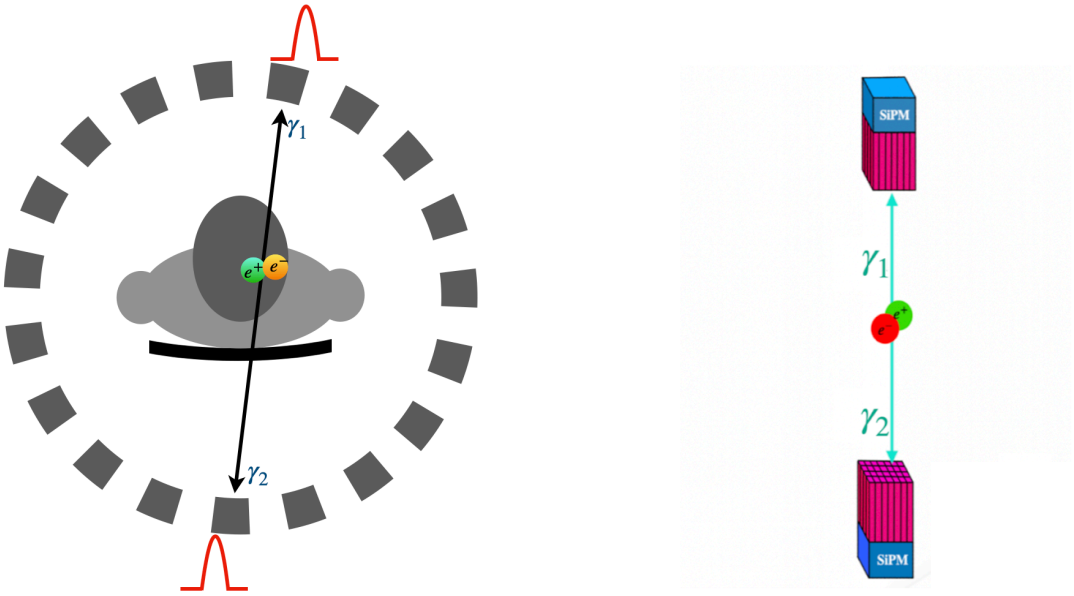

Figure 13: (left) Schematic visualization of the detecting Gamma photons emitted due to the electron and positron annihilation. (Right) illustration of the scintillation crystal (red) and SiPMs (blue) arrangments in conventional PET scanners.

Figure 14 is a schematic illustration of the PET scan and positioning of the patient inside the gantry where the PET and CT are located [55].

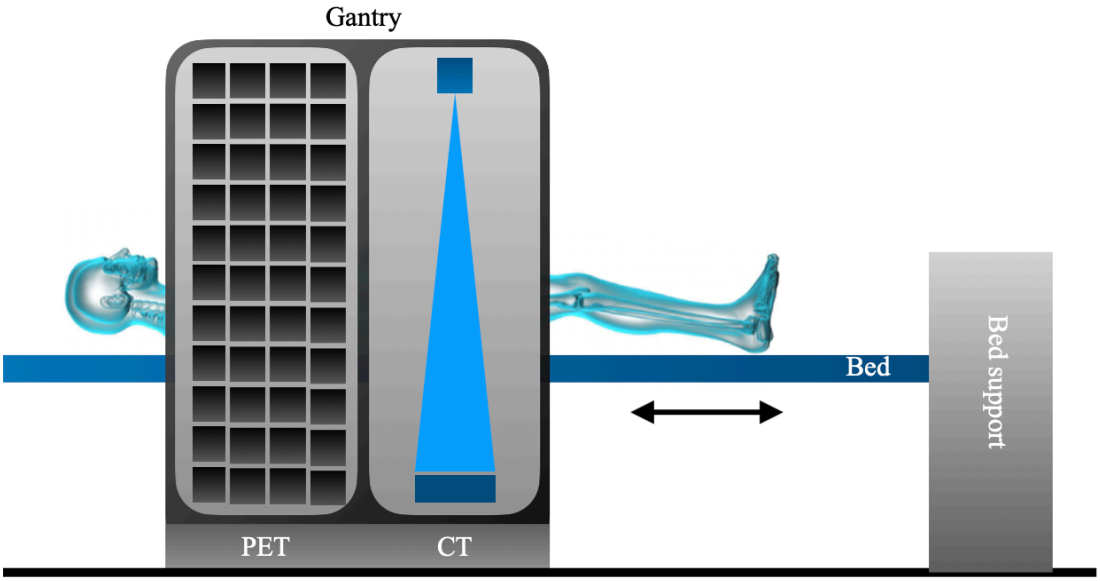

Figure 14: Schematic visualization of the PET/CT scan and positioning of the patient inside the scanner.

In the conventional PET scans to perform whole body scanning, due to the limited coverage

of the gantry along patients, the bed is needed to move and position different parts of the patient body inside the scanner. There is ongoing research for alternative approaches to increase detector coverage along the patient's body known as Total-Body PET scanners, which will be explained explicitly in the following sections [11].

In PET/CT, the CT unit generates an attenuation map of the patient's body for attenuation correction (AC). The CT consists of two main components: an external X-ray source and an array of detectors. These arrays of sensors, by detecting transmitted X-rays, provide a volumetric matrix that includes the attenuation factor of each part of the patient body. Figure 15 shows two different types of CT scanners with stationary detector rings and detector arrays.

The main difference between these two configurations is the number of detector units. While detector array-based CT has less number of detection units, it has complicated structure and engineering due to the rotation of all components.

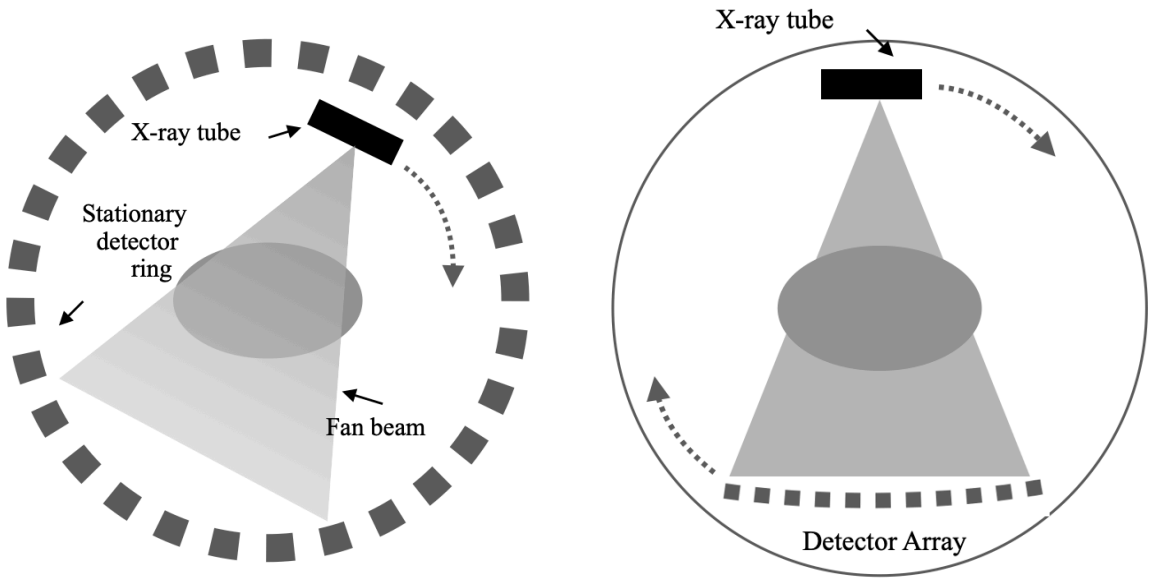

Figure 15: Schematic illustration of the CT scans, (Left) Stationary detector rings are fixed and the X-ray source is rotating around patient body to generate it's attenuation map from different projections, (right) detector array based CT, where the detectors and X-ray tubes are rotating around patients body.

Generating the CT scan in a clinically performed PET/CT scan is an essential step of the tomography to reconstruct high-quality images which can be used to determine amount of attenuation in a different part of the phantom or patient's body [56]. However, in a simulation study, there is no need for this procedure due to the precise knowledge about each specific part of the phantom.

3.0.2 Radiopharmaceuticals

The procedure of a PET scan starts with the injection of the radiopharmaceuticals into the patient's vein, where it goes through the heart and distributes to all body parts. The fluorodeoxyglucose (FDG) is the clinic's most commonly utilized radiopharmaceutical. According to the short half-life (110 minutes), ^{18}F-FDG is produced by cyclotron or linear accelerator in the clinic by bombarding ^{18}O [57]. The short half-life made a suitable tracer for PET scan applications for both clinical and pre-clinical applications [58]. In FDG structure, deoxyglucose is labeled with ^{18}F, that by emission of the positron decays to stable ^{18}O [59].

The basic operation of the ^{18}F-FDG PET is based on the difference in the physiology of the malignant cells with normals. Cancer cells, due to the higher metabolism, has higher glucose consumption. This phenomenon, allows differentiating between normal and malignant cells and can be utilized as a metric to provide information about cell physiology, which is impossible with other diagnostic methods [60].

The ^{18}F-FDG not only is utilized in diagnosing of malignant lesions but also allows for quantification of the metabolic activity of a tumor. This quantitive analytical method prevents unnecessary actions against tumors by providing accurate information about tissue uptakes. This feature, by grading malignant tumors, assists the specialist in performing a proper treatment strategy.

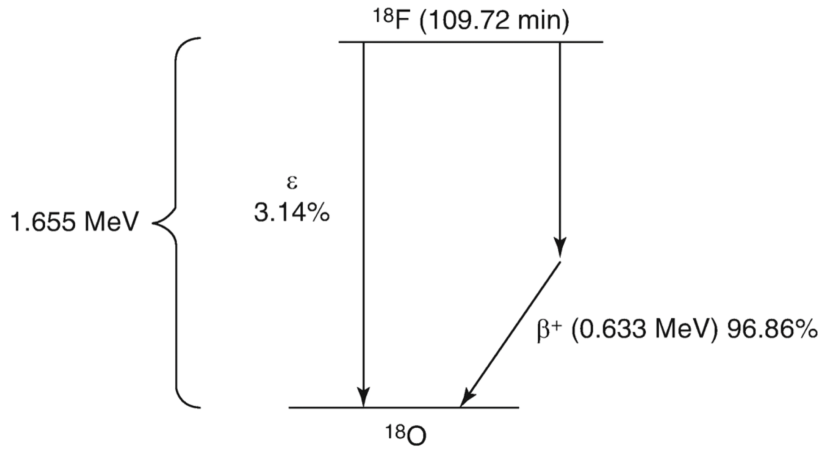

Figure 16: The decay scheme of the ^{18}F. The figure is adopted from Reference [61].

According to the decay scheme illustrated in Figure 16, ^{18}F decays by 96.9 % emission of a positron and 3.1 % by electron capturing processes into the ^{18}O. Due to their energy range, the emitted positron has a maximum of 2.4 mm range in water [62]. Considering spatial resolutions of the PET scanners, this distance made ^{18}F-FDG an ideal tracer for the localization of malignant lesions.

3.1 Lesion detectability by PET scan

The promising performance of the PET scan as a molecular imaging modality motivates numerous research groups to improve its performance. Lesion detectability as the main task of PET with the ability the provide their activity concentration is a distinguishing feature of this device. PET scan provides an image with the absolute distribution of the activity from those parts of the body covered by the field of view of the tomograph [63].

The importance of accurate measurement of the activity concentration in the lesions can be explained due to the utilization of this indicator as a metric not only to differentiate malignant lesions from benign tumors but also for grading them as necessary indexing for further treatment planning [64]

The sensitivity and spatial resolution are the major parameters that influence lesion detectability by PET scan [65]. Nowadays, the conventional tomographs utilized in clinics have a limited AFOV, which can perform only 20 cm images along patient's body [5].

Biograph Vision PET/CT, as one of the advanced PET tomographs, provides 26.1 cm of AFOV [66]. Thanks to the advanced utilizes technology based on the crystal scintillator, it has a sensitivity of $\sim$ 120 (cps/kBq) at the center, as shown in Figure 66 in Appendix A. However, it is able to cover a small fraction of the body, and a multi-bed position is required for full-body scanning. The Biograph Vision, as the advanced version of PET generation, has the 3.6 and 3.5 mm in transverse and axial transverse and axial spatial resolution, respectively.

The impact of these parameters on the system and methods to enhance them will be discussed in further sections.

3.1.1 Sensitivity

The scanner's sensitivity is a parameter that indicates the ability of the system to detect gamma photons emitted from electron and positron annihilation. It is defined as the number of the 511 KeV gamma quanta pairs, detected per time for the activity unit of the utilized source (cps/kBq) [11].

The sensitivity of the PET scanners depend on the geometrical configuration, detection efficiency, time window and dead time of the system. The PET scanner with higher sensitivity provides a higher probability of detecting photons. The photons from the annihilation of the positron-electron are emitted isotropically, as shown in Figure 17. Therefore though, Biograph Vision PET/CT has high sensitivity ($\sim$ 120 (cps/kBq)), due to its limit AFOV (26.1 cm), only small fractions of the patient body benefit from it.

As shown in Figure 17, due to the limited axial coverage of the detectors along patients' bodies, only a small fraction of the photons were detected by the scanner. Extending the axial coverage of the PET scanners improves sensitivities by detecting the higher amount of photons. The impact of

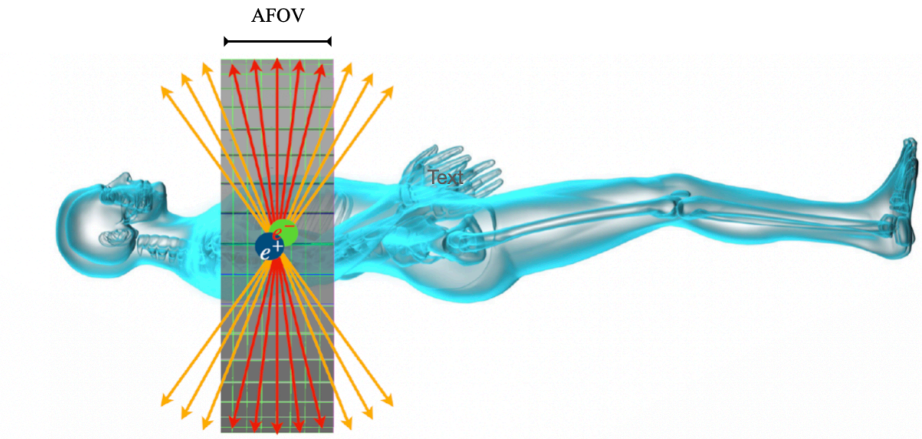

Figure 17: Schematic visualization of a patient inside a PET scanner (gray), which is detecting only a fraction of the emitted gamma photons (red) While the rest escapes without detection (yellow)

enlarging the Axial Field-of-View (AFOV) of the tomographs will be discussed in further sections.

3.1.2 Spatial resolution

The spatial resolution can be defined as the minimum distingushable distance between two annihilation points detected by a scanner. Based on the definition, to achieve high quality and detailed image, a PET scanner with high resolution is needed [67]. The conventional PET scanners, with the best achievable nominal spatial resolution ($\sim$ 3.6 mm) are not a suitable option to detect small lesions in the sub-centimeter grades due to their limited AFOV. The whole body images require longer scan time and can cause patient motion as the consequences.

There is a list of the parameters that specify the spatial resolution of the PET scanners, such as detector size, positron range, noncolinearity of the photons emitted from electron and positron annihilation, and image reconstruction method [68]. By considering the parameters mentioned above, optimizing the design of the detectors and utilization of the appropriate image reconstruction algorithm enhance the spatial resolution of the PET scanner.

3.1.3 Obstacle in currant clinical PET scans

Currently, available PET scanners, due to their limited AFOV, cover a small fraction of the patient body, and as a consequence, most of the photons escape without detection. Consequently, the lower sensitivity of these generations of PET scanners reduces the chance of detecting smaller lesions and low uptake tumors. Furthermore, for whole body scanning, multiple bed positioning methods apply, which require longer scanning time and a higher dose for the patients [69].

Extending AFOV of PET scanner to provide larger detector coverage along the patient's body has been proposed as a solution since the nineties [70]. The specific configuration of the detec-

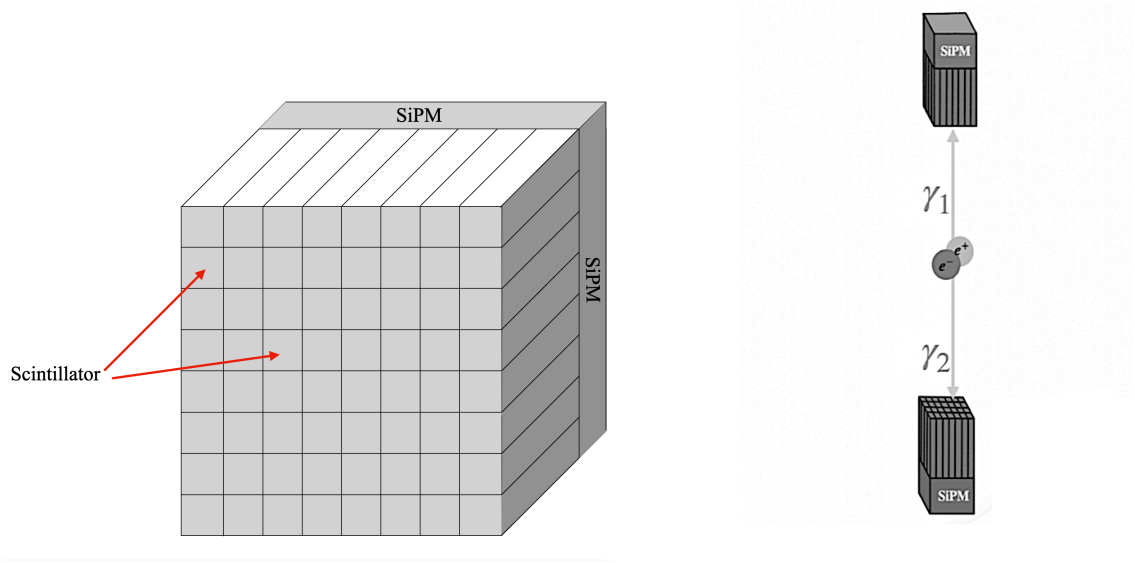

Figure 18: (Left) Schematic illustration of an array of crystal scintillators coupled radially with SiPM. (Right) arrangement a pair of the detectors and their interaction with gamma photons while coupled radially with SiPMs.

tors with the crystal array coupled with the SiPM increases (Fig 18) the construction cost of the large AFOV PET scanner. The considerable construction cost of the large AFOV PET scanners based on the current technology will prevent their worldwide use in medical centers and research institutions [11].

3.2 Total Body PET scans

The Total body PET scanner term refers to a new generation of tomographs with a large AFOV capable of simultaneous imaging of the entire patient's body [71]. Due to the large AFOV, total body pet scanners have more sensitivity compared to conventional tomographs, which enhances the possibility of detecting smaller lesions [72]. Total-Body PET scanners extended the applicability of molecular imaging to a wider range of fields such as cardiovascular disease, multi-organ imaging, physiological study, treatment monitoring, whole-body dynamic imaging, etc., which are not possible with current tomographs due to their limited AFOV. The promising performance of the Total Body PET scanners led to extending their utilization in both clinical and preclinical applications [11].

3.2.1 Human grade Total Body PET scan

The greater coverage over the human body by Total Body PET scanners with respect to the standard clinically available tomographs not only enhances the scanner's sensitivity but also enables the dynamic imaging [73].

The first Total-Body PET with 194.8 cm of AFOV has been constructed in California UC Davis by utilization of crystal scintillators [9,10]. This scanner provides the sensitivity of ~ 230 (cps/kBq) in larger flaten area (~ 100 cm) along its AFOV as shown in Figure 66 in Appendix A, in comparision to the Biograph Vision as a representative from conventional PET scanners [10].

This large AFOV in uEXPLORER has been provided by equipping scanners with multiple units with large amounts of scintillation crystals, SiPM and electronics (as shown in Figure 19) which increased significantly construction price in comparison to current clinical PET scanners [73] .

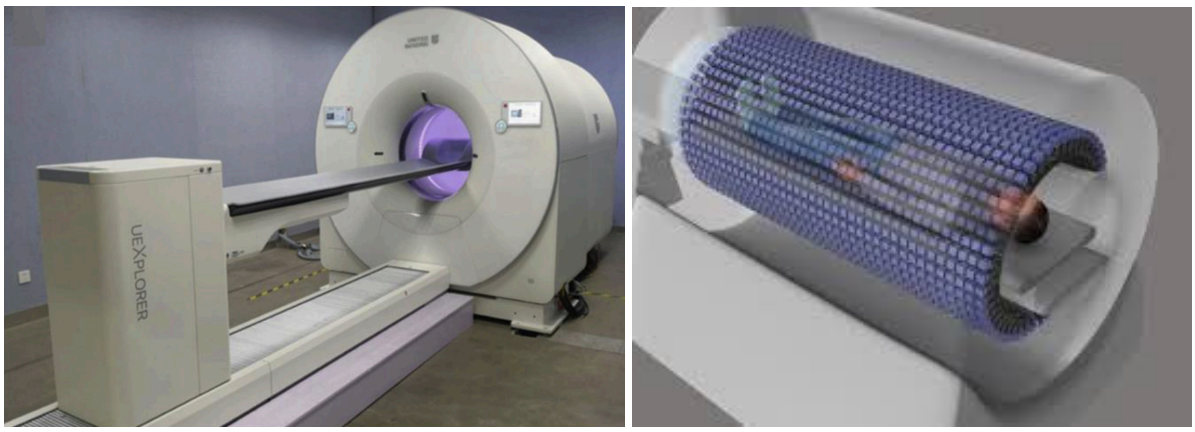

Figure 19: (Left) uEXPLORER Total-Body PET scaner. (Right) schematic illustration of the uEXPLORER Total-Body PET shows arrangement of the detectors. The figures is adopted from References [9] and [73].

The detection principle of current clinical tomographs and arrangement of scintillation crystals and SiPMs prevents researchers from developing cost-effective TB PET scanners. TB PET scanners can deliver excellent new diagnostics features such as parametric imaging, and dynamic imaging, resulting in better specificity for distinguishing between cancer and inflammations. But the construction cost is the main obstacle preventing uEXPLORER from broad dissemination in the hospitals.

Alongside the wide range of applications and benefits of Total-Body PET imaging, the high cost of employing per unit reduces the hopes for comprehensive usage in clinics. This problem emphasizes the demand to find alternative technology for the development of affordable TB PET to make it publicly available in clinics [3].

To map the substantial consequences of the high construction cost of TB PET with traditional technology, it is important to consider it as the main barrier to the possible function of these types

of scanners in medical research clinics.

3.3 Tumor to background ratio

Tumor to background ratio (TBR) is a metric that expresses the lesions' contrast to the surrounding physiologically healthy tissue [74]. TBR is the ratio between the maximum standard uptake value (SUV_{Max}) of the detected lesions to the SUV_{Mean} of the healthy tissue from the same tissue, or organ [75]. TBR is expressed according to the equation 1:

$$TBR = \frac{SUV_{Max}}{SUV_{Mean}} \tag{1}$$

To calculate TBR, first, a region of interest (ROI) will be drawn over the lesions in the reconstructed image. This region includes all the tumors and a small margin to ensure that the lesion is inside the ROI as shown in Figure 20.

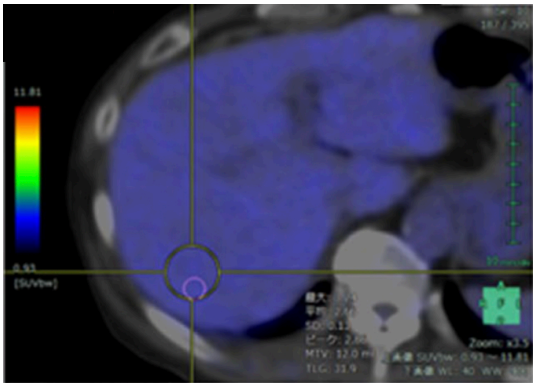

Figure 20: Exemplary illustration of the ROI in the liver. The figure is adopted from Reference [76].

The SUV_{Max} is calculated based on the maximum SUV inside the ROI of the tumor. To calculate The SUV_{Mean}, a 50 mm diameter of the ROI in the normal region of the background tissue with uniform physiological structure will be draw. The mean value of the SUV in this ROI will be used as the SUV_{Mean} [76].

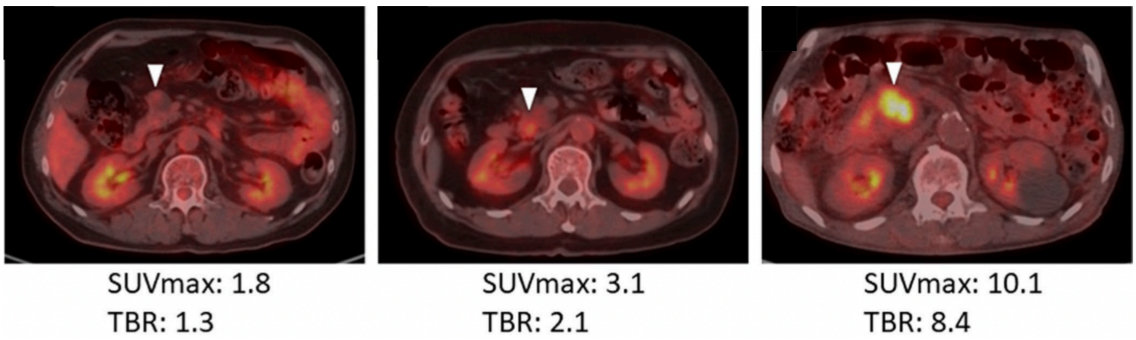

Figure 21: An example of the relation between TBR of various lesions with their intensity. The figure is adopted from Reference [76].

Amount of the accumulated radioactive tracer in the lesion, is an index to determine the physiological activity of the tumor. This index also utilized as a metric to categorize aggressiveness of the tumors. Figure 21 shows the relation of the TBR of the lesions with their intensity in the reconstructed image.

3.4 Body mass index

Since performing imaging requires to be followed by a validated universal protocol, utilization of an index that expresses the physical characteristics of the patient's body becomes essential. Patients' weight or height is not a reliable index to categorize the physical condition of their bodies by themselves. This issue emphasizes the importance of using the universal index to classify patients based on the combination of their characteristics. Body mass index is a validated scale that represents the patient's physical condition based on the combination of their weight and height. BMI of the patients is calculated as:

$$BMI = \frac{W}{(H)^2} \tag{2}$$

Where W is the patient's weight (kg) and H is the height (m).

Based on the BMI value, each person can be categorized by a universal index into underweight, normal, overweight, obese, or clinically obese, as shown in Figure 22 [77].

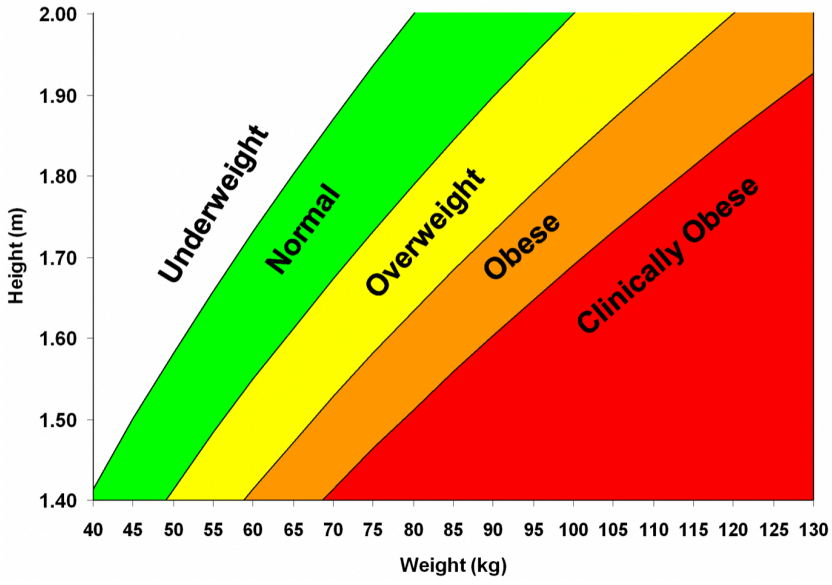

Figure 22: BMI value ranges of the various categories. The figure is adopted from dietary clinics [78].

4 The J-PET detector

The J-PET collaboration at Jagiellonian University presents novel methods in the designing of PET scanners. In opposition to the conventional PET systems, while the array of the inorganic crystal scintillators is arranged in radial configurations, J-PET utilizes an axial arrangement of the plastic scintillator equipped with silicon photomultiplier at each end. The tomographs based on the J-PET configuration allow significantly reducing the number of the required electronics and silicon photomultiplier. These feature made J-PET as a cost-efficient competitor for PET imaging [2, 79–83].

4.1 Principle of operation of the J-PET scanner

Interaction of the detected gamma photons by J-PET detectors generates optical photons that propagate to each end of plastic scintillators. The photomultipliers at each end of the scintillators convert the optical photons into voltage signals as shown in Figure 23.

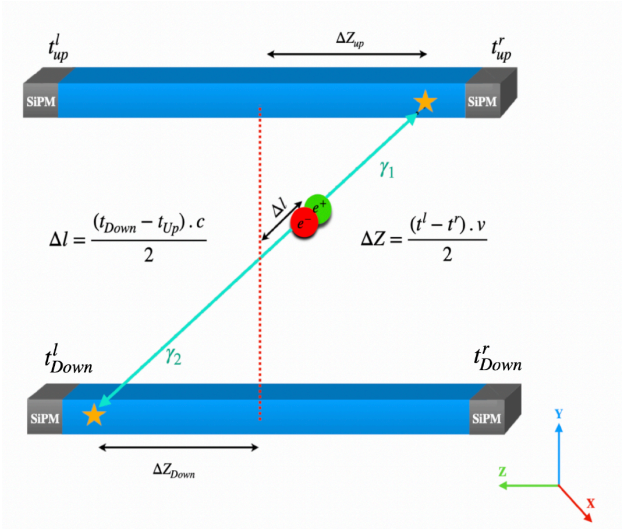

Figure 23: Illustration of scintillators arrangements, principle of detection and reconstruction of annihilation positions in the J-PET plastic scintillator based technology where the axially arranged scintillator (blue) is readout by two photomultiplier of both ends (gray).

The arrival time of the signal to the up (or down) SiPM is used to determine the interaction point of the gamma with the detector [2]. A similar process will evaluate the interaction point of the second gamma quanta with the down detector. The green line is a line of response (LOR) representing all possible places of the electron and positron annihilation. The annihilation point of the electron and positron along LOR is determined based on the difference between the arrival time of the gamma photons to the up and down detector.

The data achieved in this process is utilized to determine not only the interaction point of the gamma photons with scintillator materials but also further analysis can specify the annihilation point of the electron and positron [2].

4.2 Prototypes of the J-PET scanner

The first human grade prototype of J-PET detector comprises three cylindrical layers of EJ-230 plastic scintillator strips with dimensions of $7 \times 19 \times 500$ mm^3 coupled with Hamamatsu R9800 vacuum tube photomultipliers (PMT) at each end, as shown in Figure 24. This generation of J-PET scanners by 50 cm of AFOV was established to evaluate the scanners' performance [5]. It has been utilized to demonstrate the first positronium image [82], fundamental studies of discrete symmetries in the decays of positronium atoms [81], and to study multi-particle entanglement of photons originating from the decay of positronium [84].

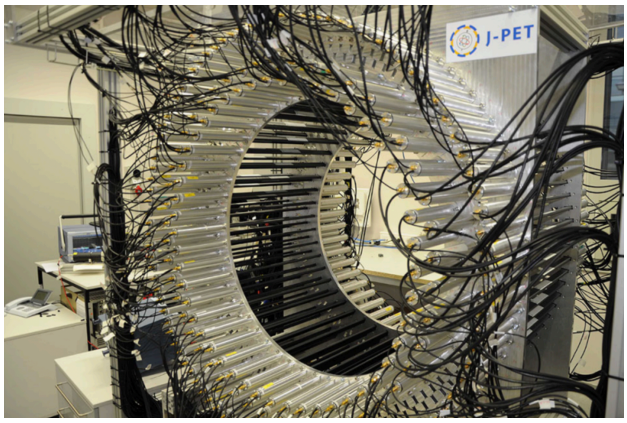

Figure 24: The first human scale prototype of the J-PET detector consist of 3 layers of EJ-230 plastic scintillator coupled with PMT at each end .

The latest prototype of the J-PET collaboration is constructed from 24 independent detection modules. Each module consists of 13 BC-404 axially arranged plastic scintillator strips with the dimensions of $6 \times 24 \times 50$ mm^3 equipped with S13361-6674 Hamamatsu SiPMs (Silicon PhotoMultipliers) with 1×4 matrix, to both ends as shown in the Figure 25. These modules are arranged in a cylindrical configuration to compose a 50 cm long AFOV PET scanner called 24 Modular J-PET.

4.3 Total Body J-PET scanner

A decade of experience designing, constructing, and developing tomographs based on plastic scintillators allows J-PET collaboration to introduce a cost-efficient Total-Body PET scanner. In addition to the lower construction price of Total-Body J-PET, large AFOV, higher sensitivity (as shown in the

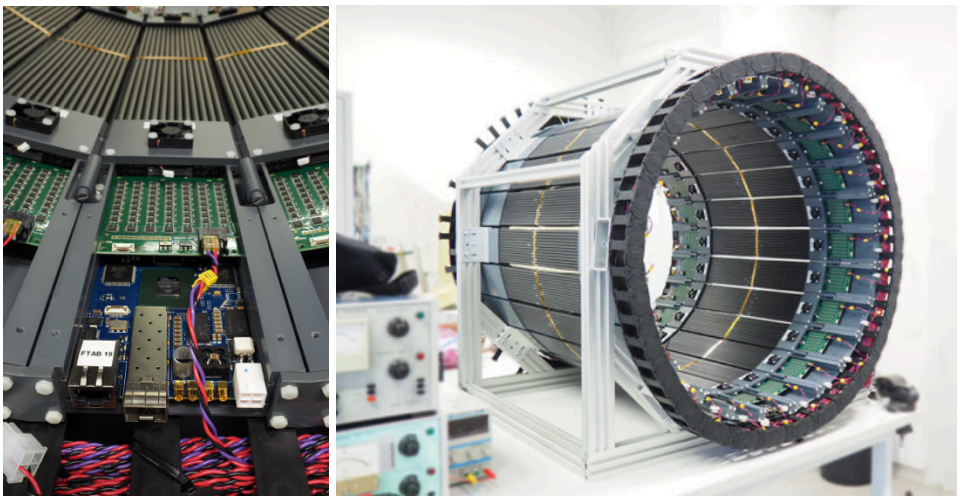

Figure 25: (Left) Photograph of the modules with the BC-404 plastic scintillator is axially located next to each other and electronic readout at each end. (Right) The cylindrical configuration of the 24 Modular J-PET with 50 cm of AFOV.

appendix A), low dose, and single bed position imaging can benefit this type of scanner compared to conventional PET scanners.

Total-Body J-PET scanner comprised of 2 layers of axially arranged modules as shown in Figure 26. Each layer consists of 24 detection units called Modules, including 16 EJ-230 plastic scintillators with the dimensions of $6 \times 30 \times 2000$ mm^3, as shown in Figure 26. This scanner has 200 cm of AFOV, which provide full detector coverage along the patient's body [1].

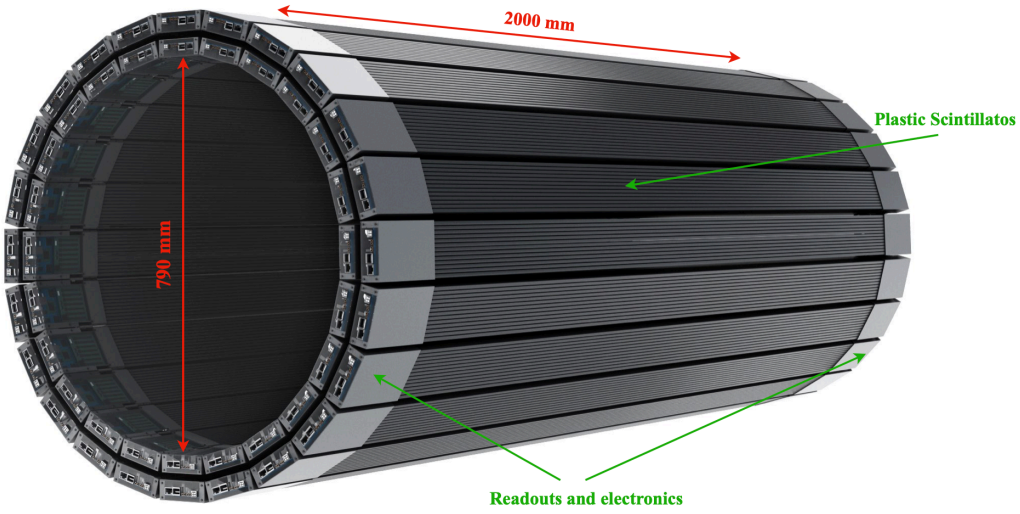

Figure 26: 3D rendered images of the Total-Body J-PET with dual layers of the axially arranged Modules. One layer consists of 24 modules each comprising 16 scintillator strips with dimensions of $6 \times 30 \times 2000$ mm^3 coupled with array of SiPM at each end.

However, the long AFOV of Total-Body PET scanners improve sensitivity, but the contribution of the oblique LORs, by increasing scatter coincidences, has a negative influence on their spatial resolution [85].

For the case of the presented study, alongside the configuration mentioned above, another arrangement of the plastic scintillator with a smaller cross-section has been utilized to investigate its effect on the scanner's performance. The proposed scanner has same geometrical dimensions as illustrated in Figure 26.

The main difference between these two configurations of Total-Body J-PET scanners is the division of the scintillator thickness in radial axes into the five smaller plastic scintillators named Mini-Bar configuration (Figure 45).

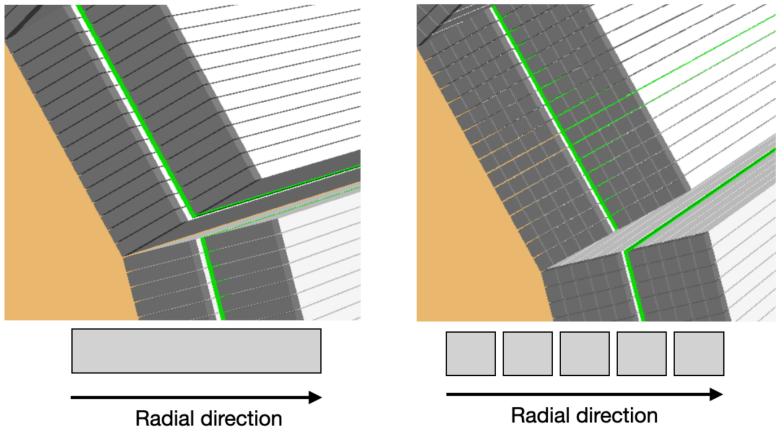

Figure 27: (Left) Illustration of the Total-Body J-PET scanner comprised from $6\times$ 30 $\times$ 2000 mm ^{3} strips and (right) Mini-Bar Total-Body J-PET consist of $6 \times 6 \times 2000$ mm^3 which has been repeated five times in radial direction.

4.4 Aim of the thesis

The main aim of this thesis is to determine the minor detectable lesion by Total-Body J-PET scanner and optimize this feature of tomograph. For this reason, spatial resolution and sensitivity of the Total-Body J-PET as two key parameters determining the smallest detectable lesions will be investigated. Enhancing any of the parameters mentioned above improves lesion detection of Total-Body J-PET. To estimate the clinical performance of the Total-Body J-PET, its lesion detectability will be investigated in the liver (as one of the most common organs for the formation of lesions) of the series of the XCAT anthropomorphic phantom. To investigate lesion detectability of the Total-Body J-PET in a realistic clinical situation, a series of the XCAT phantoms with various ages, gender, and BMI has been utilized.

5 Methodology

5.1 Simulations of the Total Body J-PET scanner

As a cost-effective method, simulation plays an essential role in the design, development, and performance improvement of molecular imaging systems. In this regard, GATE software, which is a simulation platform based on the Monte Carlo method, has been able to be in line with the trend of experimental systems through a development process over the last decades [12].

Nowadays, GATE is a validated simulation toolkit that can simulate a wide range of diagnostic and treatment systems based on radiation; it has become a comprehensive and specialized open-source software.

For the case of the presented thesis, Total-Body J-PET as the main scanner has been simulated. This scanner comprises 24 axially arranged detection panels in a cylindrical configuration with a length of 200 cm. Each panel consists of 2 modules where an array of wavelength-shifting (WLS) strips is located between them. The module as the detection unit includes 16 EJ-230 plastic scintillation strips with a dimension of $6 \times 30 \times 2000$ mm^3 while coupled with silicon photomultiplier at both ends [85] as shown in Figure 28.

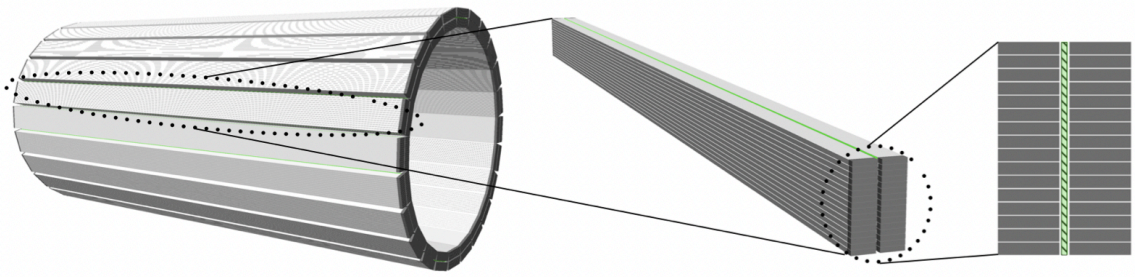

Figure 28: (Left) Visualization of the Total Body J-PET scanner. (Middle) illustration of the panel composed of two modules. (Right) Transvers illustration of the detection panels and WLS (hash line pattern) in between.

5.1.1 Utilized materials in simulation

GATE simulation software utilizes an adjustable database of various materials and elements. This database is used as the primary method, which contains all the information GATE requires to assign nuclear properties from the GEANT4 dataset and is easily modified by the user. Figure 29 shows the exemplary form of the implementation materials in the GATE database.

For the case of the presented thesis, the latest version of the GATE material database which is compatible with the J-PET application has been utilized [86].

```
[Elements]
Hydrogen:   S= H   ; Z=  1. ; A=   1.01  g/mole
Helium:     S= He  ; Z=  2. ; A=   4.003 g/mole
Lithium:    S= Li  ; Z=  3. ; A=   6.941 g/mole
Lithium6:   S= Li6 ; Z=  3. ; A=   6.015 g/mole
Lithium7:   S= Li7 ; Z=  3. ; A=   7.016 g/mole
Beryllium:  S= Be  ; Z=  4. ; A=   9.012 g/mole
Boron:      S= B   ; Z=  5. ; A=  10.811 g/mole
Boron10:    S= B10 ; Z=  5. ; A=  10.013 g/mole
Carbon:     S= C   ; Z=  6. ; A=  12.01  g/mole
Nitrogen:   S= N   ; Z=  7. ; A=  14.01  g/mole
Oxygen:     S= O   ; Z=  8. ; A=  16.00  g/mole
```

```
[Materials]
Vacuum: d=0.000001 mg/cm3 ; n=1
        +el: name=Hydrogen   ; n=1

Nickel: d=8.908 g/cm3 ; n=1 ; state=solid
        +el: name=auto       ; n=1

Gold: d=19.3 g/cm3 ; n=1 ; state=solid
        +el: name=auto       ; n=1

Carbon: d=2.1 g/cm3 ; n=1; state=solid
        +el: name=auto       ; n=1
```

Figure 29: An exemplary illustration of the GATE material database.

5.1.2 GATE output

Users can enable several types of output data files at the pre-acquisition level. GATE can generate various types of the output files such as ASCII, ROOT, Interfile, Sinogram, etc. ROOT is an object-oriented program and library designed by CERN and tailored to its needs to analyze particle physics data. ROOT's excellent performance led to its development using software such as GEANT4 and GATE in other fields. For the case of the presented thesis, all the simulation has been performed and saved in the ROOT format for further analysis.

5.2 Analysis of the GATE output

The ROOT file as the results of the GATE simulations, includes all the information about detected events, such as annihilation position, detection time and coordinates energy deposition, etc. To analyze these raw ROOT outputs, GATE Output J-PET Analyzer (GOJA) was used. It is a software developed by the J-PET Collaboration [87]. Alongside many capabilities that GOJA has, it can pre-select events and produce a listmode format (LMF) file, which may be used for image reconstruction. GOJA's LMF includes information about positions and times of the intraction and annihilation points, type of the coincidences, energy deposition etc [88].

5.2.1 Energy window

The term of the coincidences refers to the pair of the 511 keV photons that were emitted from a single electron-positron annihilation and detected in a 3 ns of the fixed time window, where there are exactly 2 interactions with the minimum 200 keV (as the energy threshold) deposited energy. [87].

5.2.2 Coincidences categorising

All of the detected coincidences in GATE simulation package categorised into the four types: true, phantom scattered, detector scattered, and random (Figure 30) [87].

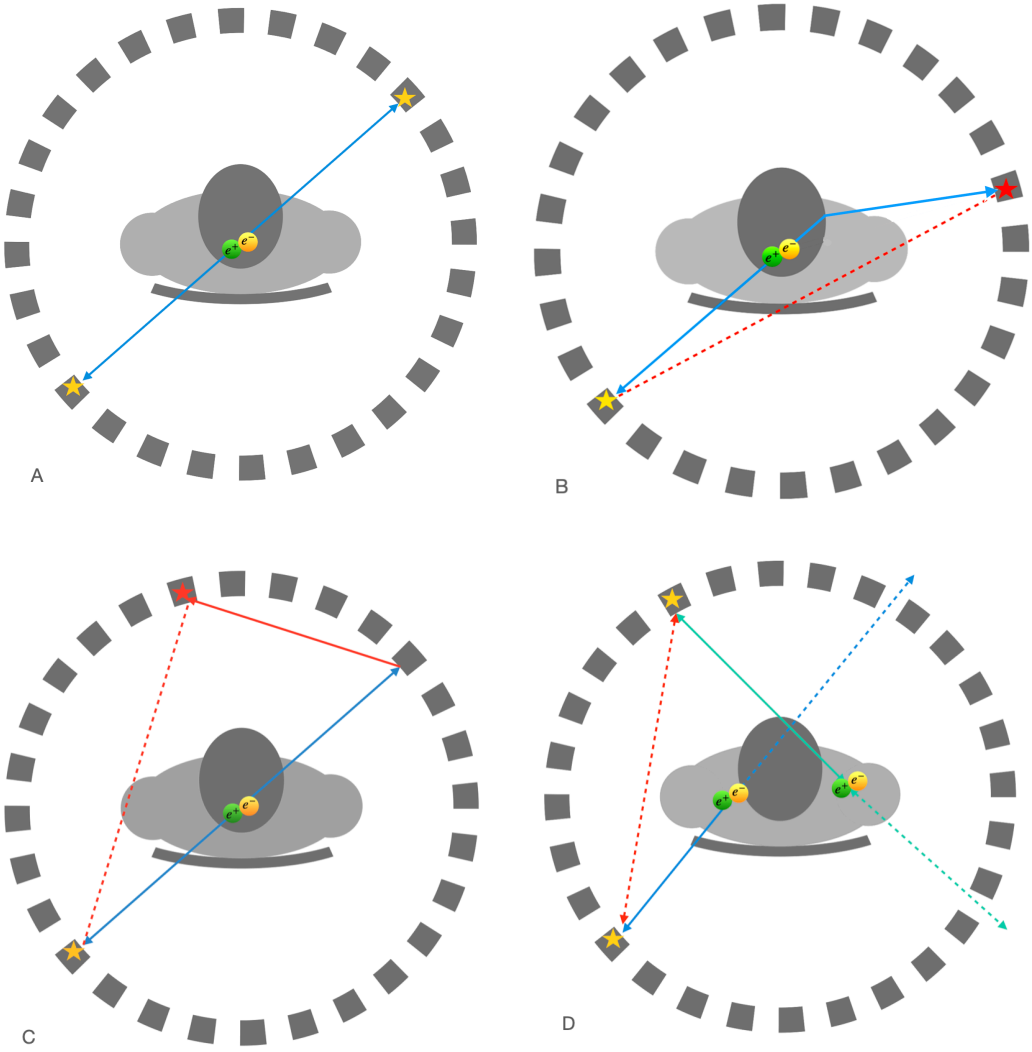

Figure 30: Schematic illustration of the (A) true, (B) phantom scatter, (C) detector scatter, and (D) accidental coincidences. Besides true, the rest of the coincidences results in wrong annihilation point reconstruction and contributes destructively to the image quality. The blue arrows are the path of the 511 keV gamma photons, and the red dashed lines are the wrong line of the response, giving a noncorrect annihilation position in the reconstructed images.

True coincidences refer to the detection of 2 photons emitted from a single e^+ e^- annihilation under the condition that none of them was scattered before detection. In phantom scattered coincidences, at least one of the detected photons was scattered in a phantom before the detection [88]. Random coincidences are events where each one of the gamma photons is from two

different (electron-positron) annihilations. Detector scattered coincidences called to those pairs of the detected gamma photons, that at least one of them scattered in the detector before final detection [88].

PET scanners determine the actual annihilation position of the electron and positron based on the detecting pair of the 511 KeV gamma photons along LOR. Among all four types of coincidences, only in true the LOR results in the the reconstruction of the actual position of the annihilation. In the rest of the situation, the LOR demonstrates the non-correct annihilation position. Based on this fact, true coincidences contribute constructively in image reconstruction, while random and scattered coincidences decrease the image quality [87].

5.2.3 Acceptance angle

The long AFOV in Total-Body PET scanners causes new challenges in data acquisition and consequently in image reconstruction. While detecting more coincidences improves the sensitivity of the scanner, the most oblique coincidences are contributing negatively to the spatial resolution of the scanner due to the unknown depth of interaction. Due to the longer path of the oblique LOR in the body of the patients and strong attenuation, the amount of scatter coincidences increases, which had a negative effect on the final reconstructed image. This issue forces to define new event selection criteria such as acceptance angle to prevent the contribution of oblique coincidences in the image reconstruction.

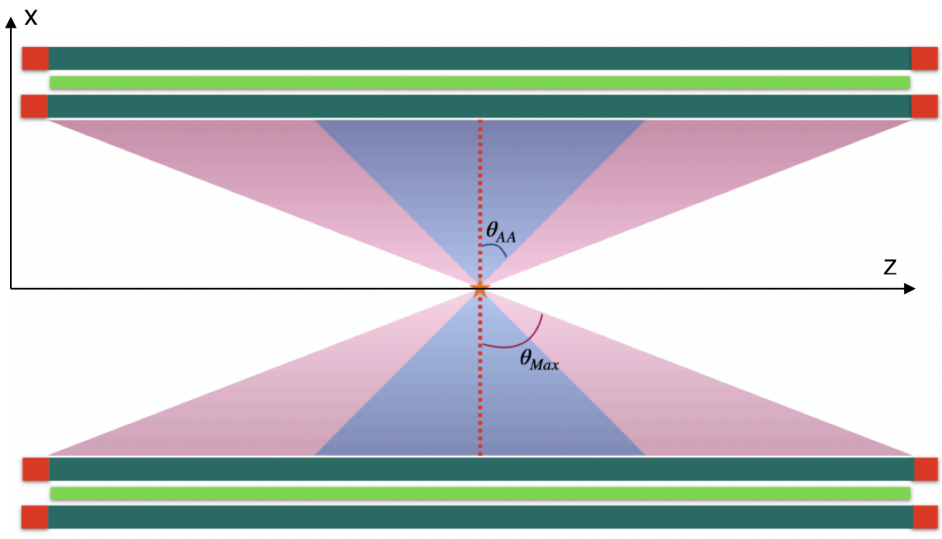

Figure 31: Schematic cross section view of TB J-PET scanner. The dark green strips are plastic scintillators where WLS illustrated with light green located between them. Each plastic scintillators equiped with SiPM (red) at each ends. The pink cone is created by the maximal angle θ_{Max}. The θ_{AA} denotes an exemplary acceptance angle.

The AA can be defined as the maximum polar angle of the coincidences as event selection criteria are taken into the final image reconstruction (Figure 31). This criterion which depends on the geometrical configuration of the PET scanners can be defined as acceptance angle-based (J-PET) or ring difference-wise (conventional tomographs). Applying such cuts improves spatial resolution with the cost of losing part of the sensitivity. This issue points to the importance of making a tradeoff between spatial resolution and sensitivity of the scanner, by determining the optimal acceptance angle cut. [85].

Two types of simulations have been performed using described geometry to investigate the determination of the optimum acceptance angle. The first simulation has been performed with a 183 cm line source with a 1mm diameter and the total activity of the 1 MBq. The study was conducted with a centrally located (parallel to the axial axes of the scanner) cylindrical phantom to evaluate the contribution of phantom coincidence events in all registered types of events. A cylindrical shape water-filled phantom with a diameter of 20 cm and length of 183 cm, first cold, then hot (with a 10:1 target/tumor background activity ratio) has been simulated. The second group of simulations has been performed by using a 1 MBq point-like source inside an air-filled cylindrical phantom with a diameter of 20 cm and axial length of 20 cm (with a 10:1 target/tumor background activity ratio).

5.3 Digital XCAT anthropomorphic phantoms

Performing accurate simulation of the medical imaging device is an essential condition in the estimation of the performance of the scanner in a realistic scenario. GATE simulation toolkit, by providing a Mont-Carlo-based method, allows for accurate modeling of the tomographs. On the other hand, there was a need for accessibility to the human-grade detailed phantom to be utilized in the simulation-based research. In addition, the main advantage of such phantoms is the lack of obstacles in human studies (Figure 32).

The XCAT phantoms, by providing virtual patients, opened a new horizon in detailed medical imaging simulation-based research. This software includes a series of anatomically precise male and female phantoms with various ages, races, gender, and physical characteristics. The XCAT generated phantoms by including thousands of the defined anatomical structures with the abilities such as heart beating and breathing. Alongside these features, the user can implement any abnormality in each specific organ for further studies [13].

These phantoms have the ability to be used as a phantom in GATE simulations. During the simulation, GATE software simulates all physical processes which exist in real scenarios, such as the annihilation of the electrons and positrons, interactions of 511 keV gamma photons with the tissue of the XCAT phantoms, and interactions of gamma photons with scintillators in the detectors.

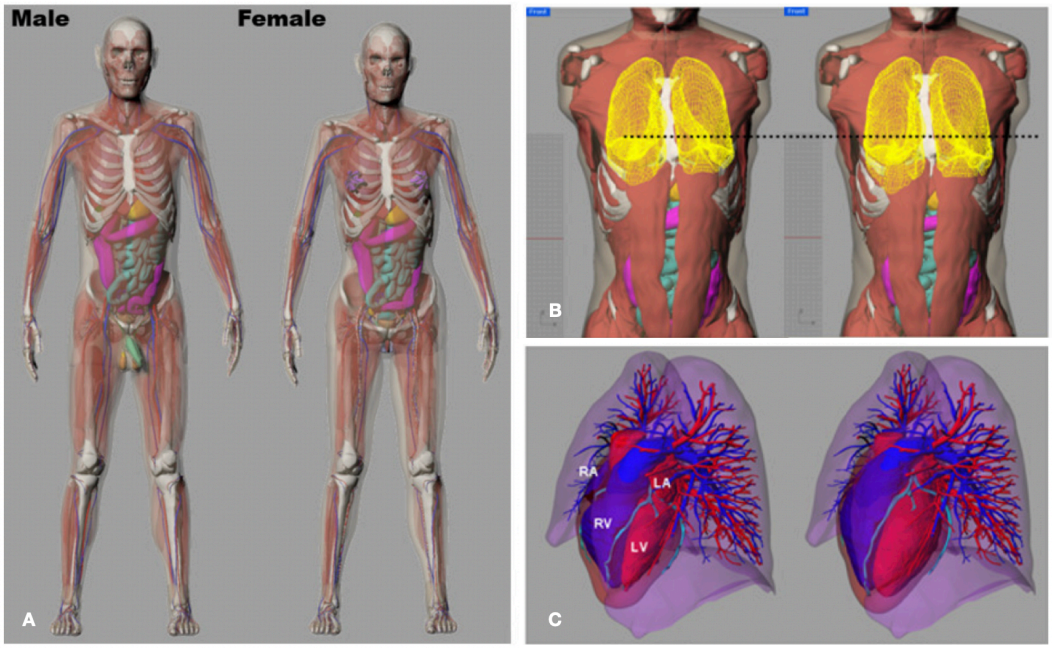

Figure 32: Visualisation of the (A) male and female XCAT phantom with the possibility of respiratory motion (B) and heart beating (C). The figure is adopted from the XCAT user guide by Duke University.

5.4 QETIR image reconstruction software

The new Quantitative Emission Tomography Iterative Reconstruction (QETIR) software has been developed by the MEDISIP group at the Ghent University in Belgium [89]. Initially, the software included only an MLEM reconstruction algorithm and was used only for local purposes. QETIR is created with C++ object-oriented programming and built with CMake tools. The input of the software is a TOF and non-TOF LM data, that can be transformed to TOF or non-TOF sinograms if necessary. One of the important features of QETIR is the possibility to parallelize reconstruction process on several processor cores with Message Passing Interface (MPI) system.

5.4.1 QETIR configuration files

QETIR consists of 4 main libraries. The ”config” library provides a reading of the parameters of the configuration files set by users. The ”core” library is responsible for data input and output. It also generates a sensitivity map of the scanner (a collection of all possible lines of response (LORs) for the normalization). The scanner’s geometry should be described by the user in a configuration file. The ”ext” library provides additional functionality for image reconstruction, such as image post-filtering, image analysis, and a raytracing method. Finally, the ”recon” library loops over events presented in the LM file and performs reconstruction. Currently, QETIR does not have a graphical

user interface (GUI), so users have to use the command line to start reconstruction. Users also have to describe configuration files. These files are simple text files: one for the scanner's geometry and another for reconstruction parameters. If necessary, the user can change the C++ code to add custom parameters and change the functionality of QETIR (Figure 33).

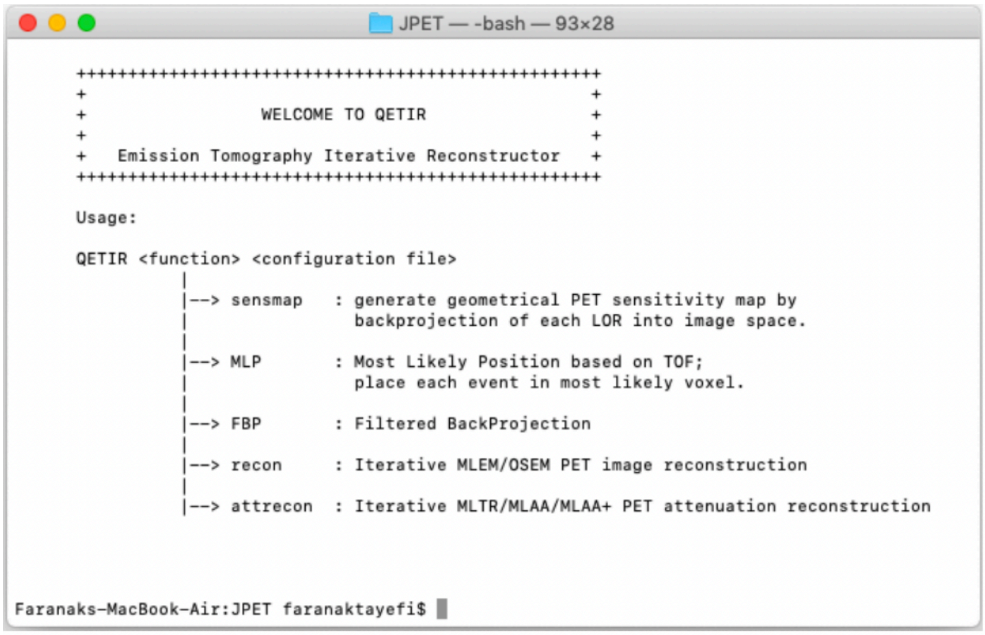

Figure 33: Main page of the QETIR image reconstruction software including short userguide about its utilization.

5.4.2 List-Mode data

There are 3 basic files that should be provided to the QETIR software as input data. The first file is an LM data file. QETIR works with binary files with 6 (non-TOF) or 7 (TOF) float numbers. Each line of this file corresponds to one coincidence event:

x_1, y_1, z_1, x_2, y_2, z_2, dt

Where x_1, y_1, z_1 are the coordinates in mm of the first event in a coincidence, x_2, y_2, z_2, are the coordinates in mm of the second event in the coincidence, dt is the time difference of the events in ps which can be as positive as well as negative. The reconstruction can be done either way, taking dt into account or not. For non-TOF PET scanners, the LM data file is the same, except absence of the dt (Figure 34).

5.4.3 Sensitivity map

The sensitivity map is another required file by QETIR for image reconstruction purposes. This map is utilized by QETIR to normalize the geometrical efficiency of the scanner. One of the main

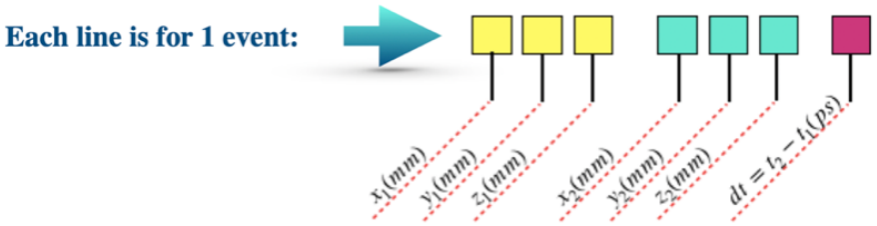

Figure 34: Schematic illustration of the LM file required by QETIR for image reconstruction application. (Yello) cordinate of the first hit, (green) coordinates of the second hit, (red) time difference between two hits.

advantages of QETIR image reconstruction software is its ability to generate a sensitivity map standalone. This feature makes QETIR an independent image reconstruction software that only requires LMF to operate. To generate a sensitivity map by QETIR, the user needs to execute sensitivity map configuration, which includes information about sensitivity map size, voxel size, number of back-to-back photons per voxel, etc. Figures 35 and 36 are an example sensitivity map of Total-Body J-PET, generated by QETIR image reconstruction software.

The generated sensitivity map is the sum of all the possible lines of the response from each specific voxel registered by the pair of detectors. A total number of the generated line of the response is defined by the user. As shown in Figure 35 the intensity of the line of the responses that represent detection probability is maximum at the center of the scanner (green), while by getting closer to the edge of the scanner first decreasing (lite blue) then increased due to the higher number of the line of responses in two neighbors modules and correspond strips.

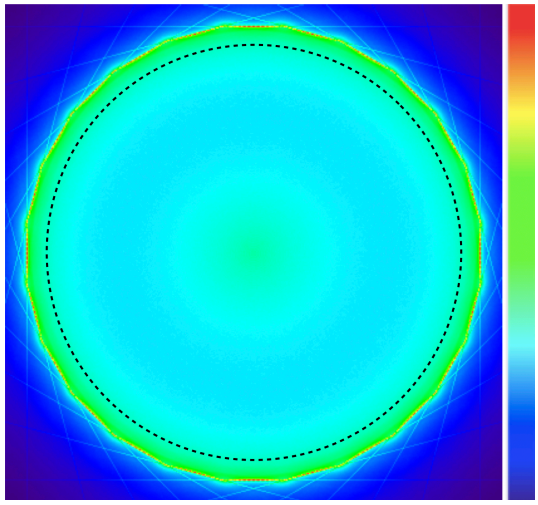

Figure 35: Transverse visualization from sensitivity map of Total-Body J-PET, generated by QETIR software. The black dashed circle indicates the inner part of the Total-Body J-PET.

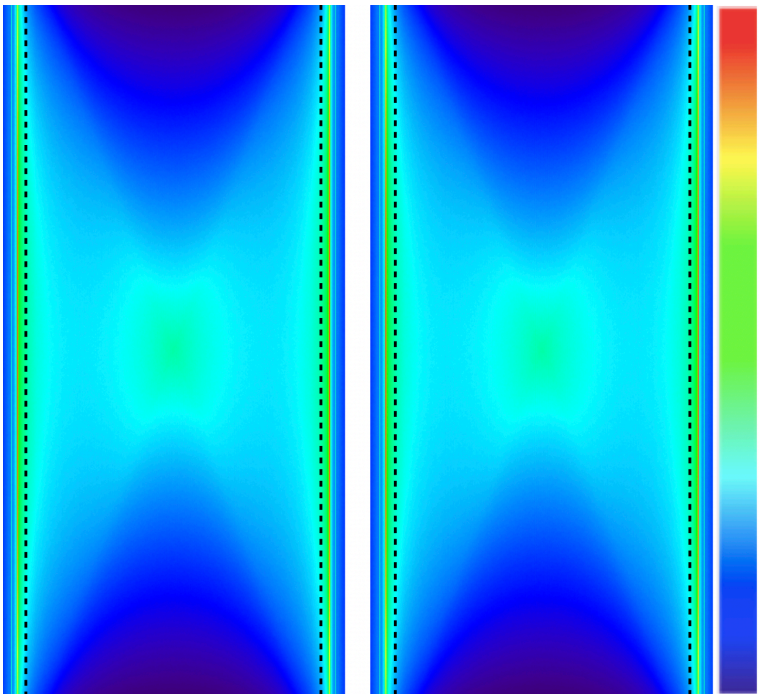

Figure 36: (Left) coronal and (right) sagittal visualization from sensitivity map of Total-Body J-PET.The black dashed lines indicate the inner part of the Total-Body J-PET.

5.5 AMIDE software

Amide's a Medical Image Data Examiner (AMIDE) is a free multimodality software for medical image analysis applications. It is user-friendly with a graphical user interface (GUI) for visualization and analysis of the 3D medical volumetric images and data sets such as PET, CT, and MRI [90]. All of the datasets mentioned above can be manipulated or customized by users with AMIDE software. In the presented thesis, AMIDE was used to visualize and analyze all the reconstructed images. Figure 37 illustrates the road map and essential requirements in the image reconstruction.

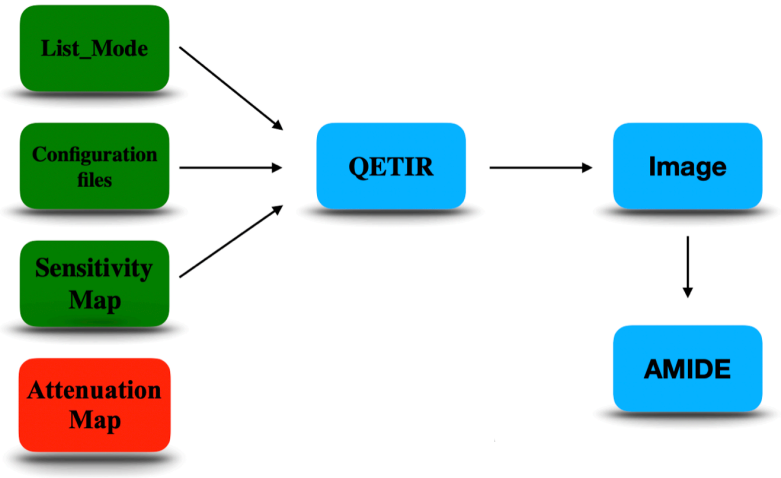

Figure 37: Schematic illustrations of the input files to QETIR software and visualisation of the reconstructed images.

6 Results

6.1 Acceptance angle of Total-Body J-PET

Several simulations have been performed to determine the optimum acceptance angle (AA) in the Total-Body J-PET scanner. The dependence of the different types of coincidences on the various value of the acceptance angle has been investigated. For this case, seven additional value between 10° up to 69° (maximum achievable angle) with the steps of the ten degrees has been examined. In addition to these degrees, 18 ° (as the maximum possible by conventional PET scanners), 45 ° and 57 ° (as the utilized criteria in Total-Body PET scanners), and 65 ° (as the maximum AA by other Total-Body PET scanners) has been investigated [85, 91, 92].

As shown in Figure 38, by enlarging AA, the total number of the different types of coincidences is increasing due to the higher detection probability. However, the increment rate of the total number of coincidences was decreased by choosing larger AA. Figure 38(Left) shows the percentage share of different types of coincidences as the function of the AA for a 1 MBq line source with a total length of 183 cm which is the average height of the male in the Netherlands (as the country with tallest people in the world). Figure 38 (Right) illustrates the same parameter in the presence of the 20 cm diameter cylindrical hot background (8:1, source to background activities ratio) phantom.

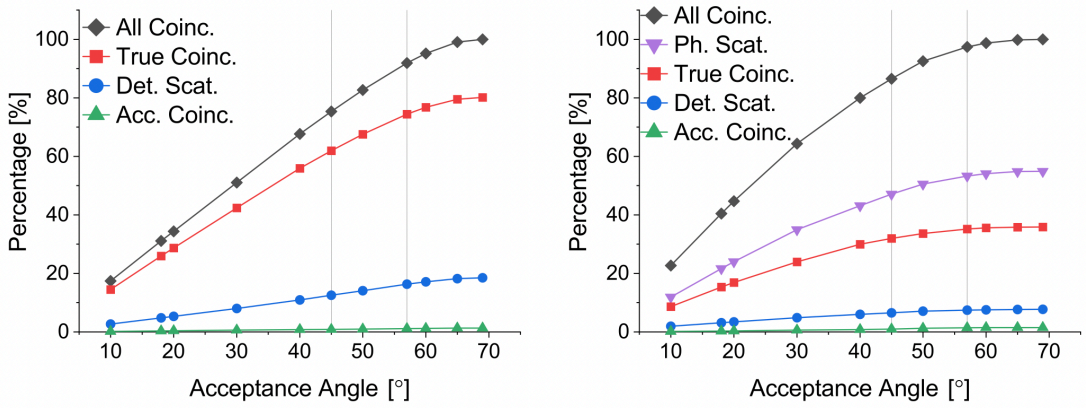

Figure 38: Percentage shares of the different types of coincidences as a function of the AA for a 183 cm line source (Left) and for the same line source inside a 20 cm diameter cylindrical hot background phantom (right).

Four types of coincidences have been shown in Figure 38, true (red square), detector scatters (blue circle), accidental coincidences (green triangle), and phantom scatter (violet inverse triangle), and the sum of all type of coincidences (black diamond). The characteristics and categorizing logic for each type of coincidence mentioned above have been illustrated in Figure 30.

As shown in Figure 38 the percentage share of the coincidences increases by applying a larger

acceptance angle. While in the absence of the phantom, the percentage of true coincidences (red square) is larger than other types of coincidences, but in the presence of the phantom, the phantom scatters (violet inverse triangle) constitute the highest percentage among all types of coincidences.

Fraction of the different types of coincidences with a 1MBq activity line source in the presence of the 20 cm diameter cold (activity less phantom) background phantoms with 183 cm length, has been investigated as shown in Figure 39 with similar behavior as the Figures 38.

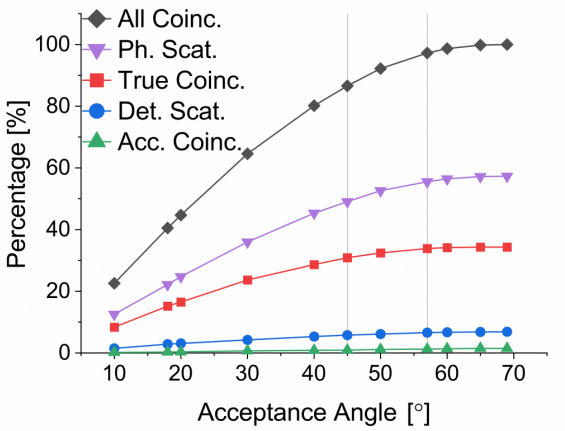

Figure 39: Percentage share of the different types of coincidences in cold phantom as a function of AA.

As shown in Figure 39, the percentage share of the coincidences is similar to Figure 38. However, the percentage of true coincidences (red square) in the phantom with cold background (Figure 39) is slightly less than what has been shown in Figure 38. This difference is due to the true coincidences from the uniform distribution of the activity as background in the hot phantom.

Since applying the acceptance angle changes the total count of the detected coincidences, this parameter has a direct influence on the sensitivity of the scanner as a parameter that explains the detection probability of the tomograph. In the second step, the effect of the AA on the sensitivity of the Total-Body J-PET has been investigated. In general, the sensitivity of the scanners refers to the fraction of the registered events divided by the activity per slice. To evaluate the influence of the utilization of AA on the scanner, total sensitivity (the mean values of the sensitivity for every slice) and sensitivity at the center (sensitivity at the central slice) of the Total-Body J-PET were investigated as shown in the Figures 40 and 41.

As shown in Figures 40 and 41, there is an obvious impact of the AA on the sensitivity of Total-Body J-PET, that enlarging AA, a higher number of the coincidences with larger polar angles are taking into account. Contributions of the oblique coincidences by enlarging AA cause the increment of the scanner's sensitivity. To investigate the effect of this event selection criteria on the spatial resolution of the scanner, 45 $^\circ$ and 57 $^\circ$ of AA were investigated explicitly based on the condition in similar Total-Body PET scanners. Two vertical lines in gray have been drawn in Figures 38, 39, 40

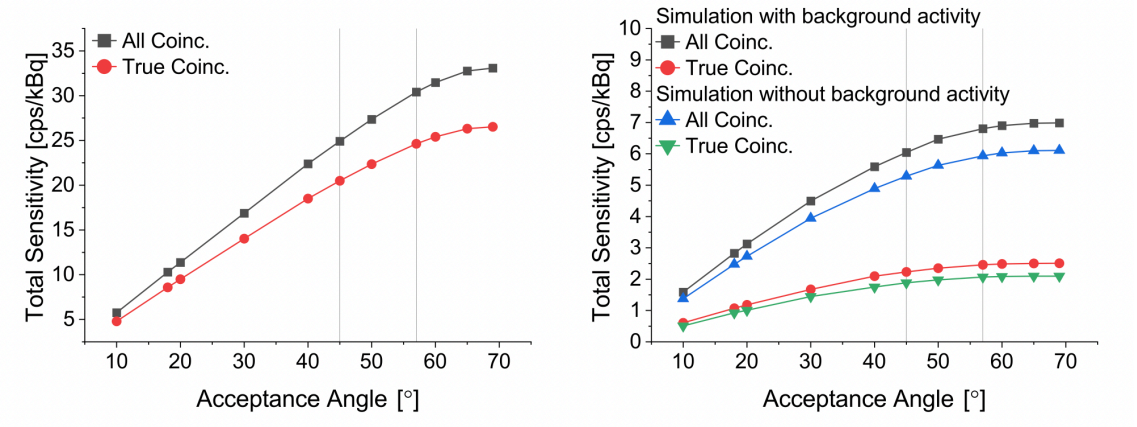

Figure 40: Dependence of the total sensitivity to the various values of the AA with a line source (left) and a line source located inside the cylindrical phantom (right) with (black square and red circle) and without (blue triangle and green inverse triangle) background activity.

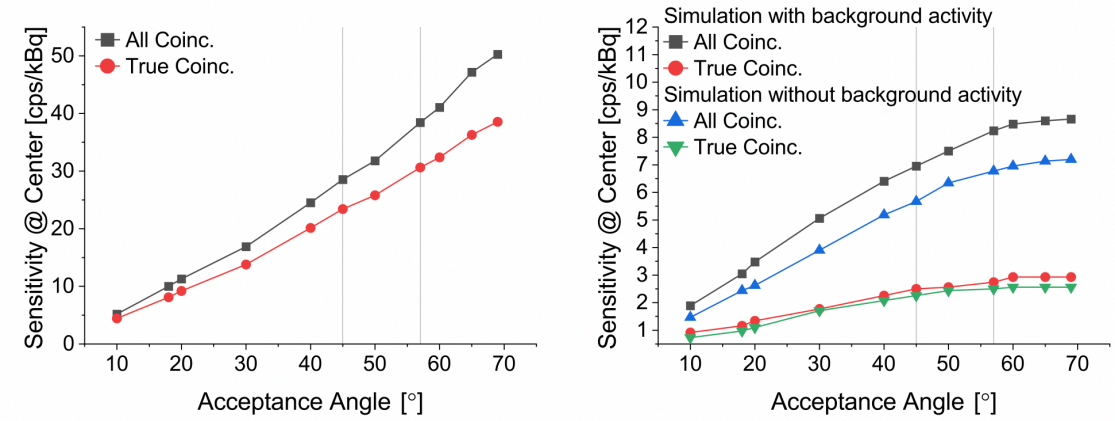

Figure 41: (Left) Dependence of the sensitivity of the Total-Body J-PET at the central slice to the various values of the AA. (Right) Sensitivity at the center of the Total-Body J-PET for all types of coincidences in the presence of the warm background phantom.

and 41, to indicate 45° and 57° as two under-investigation acceptance angles for spatial resolution. For the considered 45° and 57° of AA, 24.3% (22.7%) losses for all (true) type of coincidences has been observed.

6.2 Spatial Resolution

Spatial resolution, as one of the critical parameters in the performance of PET scanners, has a significant impact on the detection of small lesions. The point spread function (PSF) is the recommended approach to determine the spatial resolution of the tomograph. The PSF is the full width at half the maximum of the intensity profile over the point in the reconstructed images (Figure 42). A

point source inside of a hot background air-filled phantom with a ratio of 10:1 has been utilized to investigate the effect of the applying AA cut on the spatial resolution of the Total-Body J-PET.

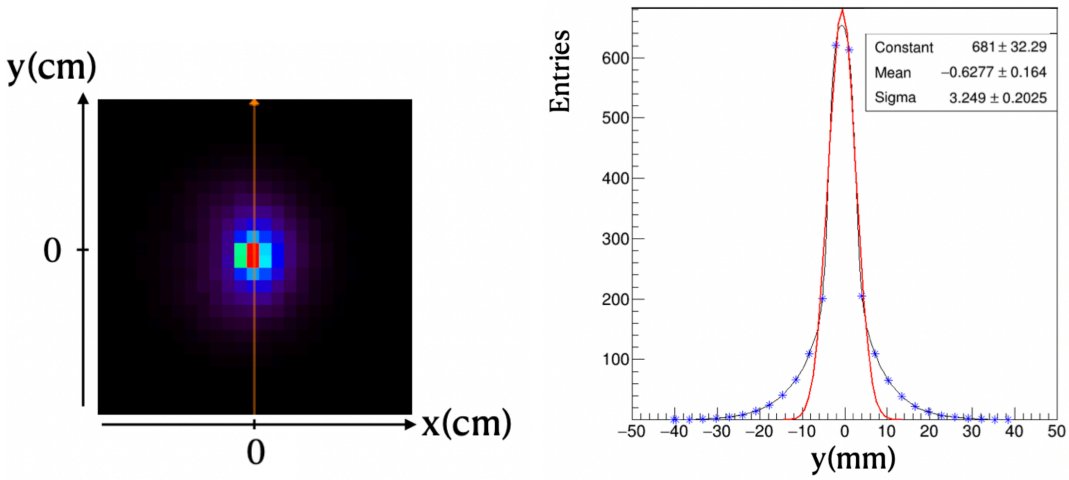

Figure 42: (Left) Exemplary line intensity profile over the reconstructed image of a single point source. (Right) the PSF values (blue stars) of the reconstructed images fitted with the Gaussian function (red line).

Figure 43 shows the PSF of the 1st iteration with 25 subsets reconstructed images for different AA. As shown in (Figure 43 left), choosing more extensive AA decreases the quality of the reconstructed image, especially in the axial direction. It shows that axial PSF equal to $\sim$ 5mm at 45° of AA is increases to $\sim$ 9 mm at 69° of AA.

The degradation of axial resolution in more extensive AA is due to the uncertainty in hit position determination from lack of depth of interaction (DOI). The calculated PSF values provide a solution to reduce the negative effect of lacking DOI with the cost of losing 25% of the sensitivity as the consequence of applying AA and removing most oblique coincidences.

As shown in Figure 40 the total sensitivity of the scanner by applying 45 and 57 degrees of acceptance angle are $\sim$20 and $\sim$ 25 (cps/kBq) respectively. However, as shown in Figure 43 (bottom), the axial resolution of the scanner by applying 45 degrees of acceptance angle has been improved by a factor of about two, compared to the 57° cut.

6.3 Sensitivity

To evaluate the sensitivity of the Total-Body J-PET scanner, a 200 cm line source with 1 MBq of activity has been simulated in the central axis of the tomograph. To investigate the effect of the removing contribution of the oblique coincidences by applying the acceptance angle, 57° cut was utilized as well. Figure 44 shows the sensitivity profile of the Total-Body J-PET with (black) and

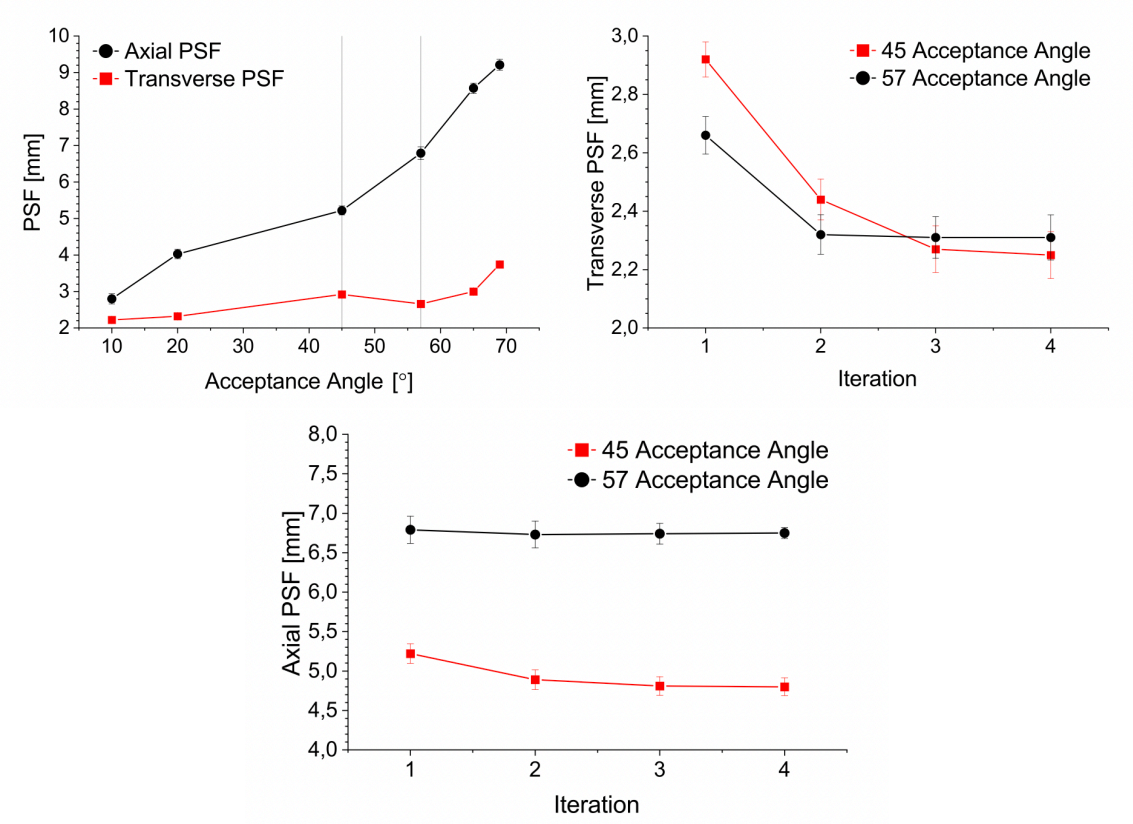

Figure 43: (left) Axial (black) and transverse (red) PSF values of a point source as the function of the AA. (Right) Transverse PSF values for 45° (red) and 57° (black) based on the number of the iteration.

without (red) acceptance angle. Due to the larger angular coverage by the detector at the center of the scanner, this region is sensitive to the applying acceptance angle cut.

6.4 DOI capable Total Body J-PET

Degradation of the axial resolution caused by the contribution of oblique coincidences, known as parallax error, led to defining AA cut. As shown in section 5.3, the cost of applying AA is losing the scanner's sensitivity. This is a comprehensive issue in all large AFOV PET scanners. The sensitivity of the scanner has a direct impact on the ability of the tomograph in the detection of smaller lesions.

One of the approaches to overcome this issue is providing depth of interaction capable detectors. For this case, a new configuration of the Total-Body J-PET with DOI capability called Mini-Bar Total-Body J-PET has been simulated for further investigation. This tomograph was designed based on the EJ-230 plastic scintillator with a smaller cross-section (6× 6× 2000 mm), as shown in Figure 45.

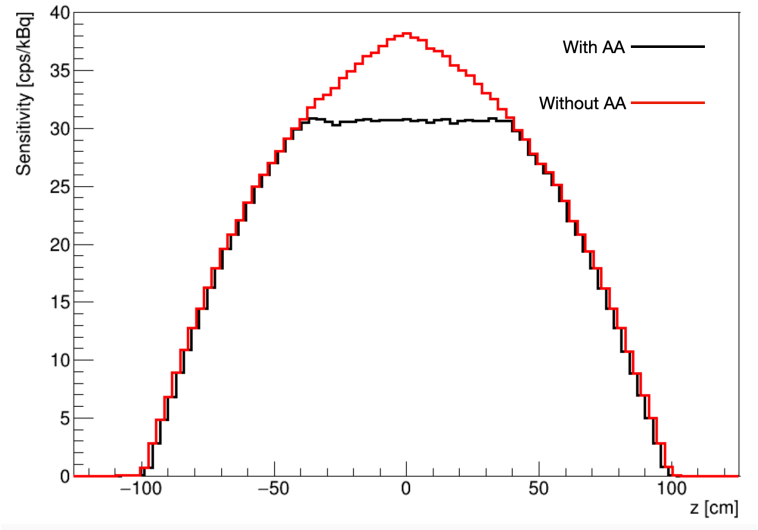

Figure 44: Sensitivity profile of the Total-Body J-PET with (black) and without (red) 57° of acceptance angle.

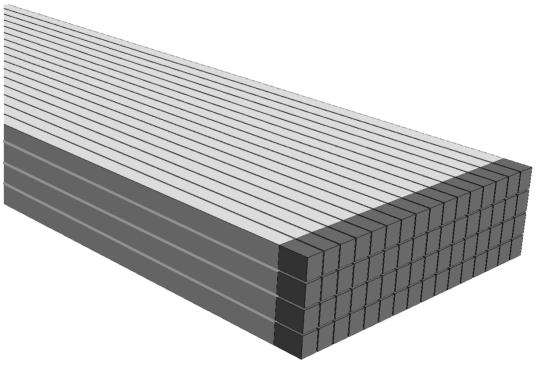

Figure 45: GATE visualisation of a single module of Mini-Bar Total-Body J-PET.

The Mini-Bar-based scanner has similar geometrical dimensions to the Total-Body J-PET. The only difference between these two scanners is the radial division of the plastic scintillator to minimize cross sections. The main aim of Mini-Bar configuration utilization in Total-Body J-PET is to improve axial resolution by reducing the uncertainty of the registered pulse. Figure 46 is a schematic visualization of Mini-Bar configuration and conventional J-PET strips.

A smaller cross-section of the scintillator in the Mini-Bar configuration leads to allocating the interaction point of the gamma photons with the scintillator with higher precision. This configuration can be known as a DOI-capable detector, which minimizes the effect of the parallax error. The main benefit of utilizing Mini-Bar Total-Body J-PET is achieving the highest possible sensitivity of the scanner without applying any acceptance angle.

To investigate the effect of the Mini-Bar configuration on the percentage share of the coinci-

Figure 46: Schematic illustration of the registration of pulse in strips and Mini-Bar Total-Body J-PET.

dences, a 70 cm cylindrical phantom with a diameter of 20 cm and a 70 cm line source has been simulated. As shown in Figure 47 percentage share of the coincidences in both scanners has the same value.

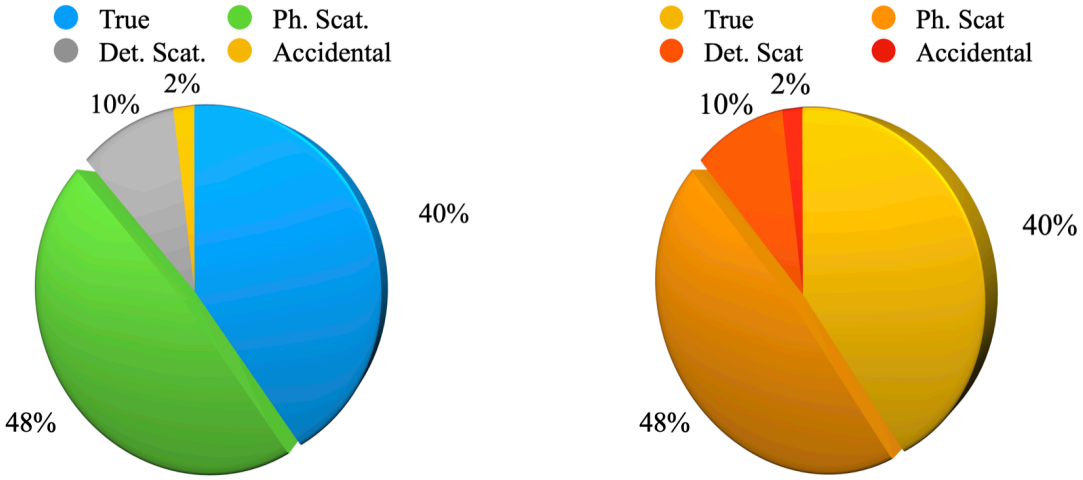

Figure 47: Percentage share of the coincidences in standard (left) and Mini-Bar (right) Total-Body J-PET.

To investigate the effect of the utilization of a smaller cross-section of the plastic scintillator in DOI capable Total-Body J-PET, the scatter fraction of this scanner has been calculated and compared with the standard Total-Body J-PET. For this porpose, two simulations has been performed for each one of tomographs, first with a 70 cm line source according to the NEMA NU-2-2018 standards, then with a 2m line as the adjusted source length for Total-Body PET tomographs. Table 1 shows the scatter fraction of these scanners based on the single slice rebining algorithm (SSRB) and true Mont Carlo methods.

Method	70 cm line source		200 cm line source	
	Standard Geometry	DOI Geometry	Standard Geometry	DOI Geometry
SSRB	36.71 ± 0.03 [%]	36.62 ± 0.03 [%]	35.9 ± 0.03 [%]	35.84 ± 0.03 [%]
True MC Ph. Scat. + Det.Scat.	59.17± 0.05 [%]	59.01 ± 0.05 [%]	63.93 ± 0.06 [%]	64.03 ± 0.06 [%]
Ture MC Ph. Scat.	54.85 ± 0.06 [%]	54.83 ± 0.06 [%]	60.92 ± 0.07 [%]	61.02 ± 0.07 [%]

Table 1: Scatter fraction values of the standard and DOI capable Total-Body J-PET.

To compare the performance of the Mini-Bar with standard Total-Body J-PET, additional simulations to estimate the sensitivity of these two scanners has been accomplished. As shown in Figure 48, the sensitivity profiles of these two scanners before and after applying the acceptance angle are the same.

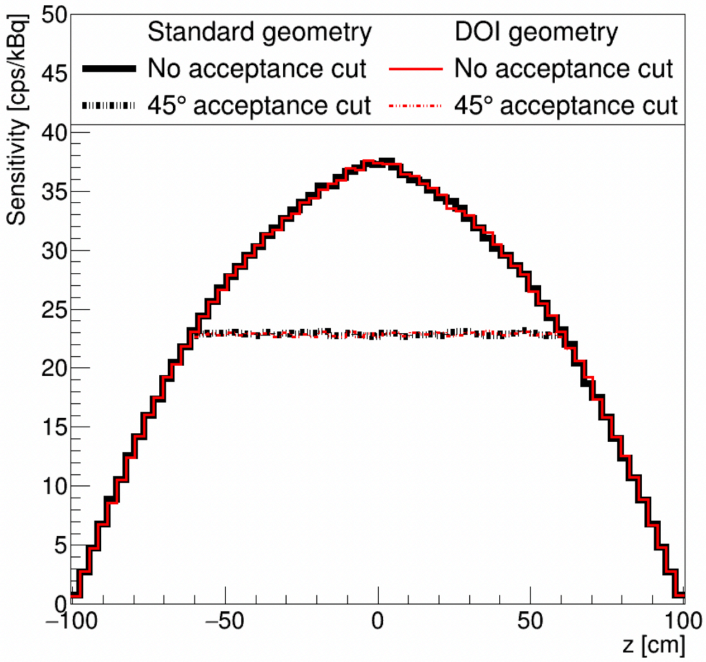

Figure 48: Sensitivity profile of the standard (black) and Mini-bar (red) Total-Body J-PET before (solid line) and after (dotted line) applying acceptance angle cut.

The main aim of introducing Mini-Bar Total-Body J-PET was to improve axial resolution without losing sensitivity by applying an acceptance angle. For this case, a point source in various cylindrical phantom which mimics different BMI has been simulated, and corresponding axial resolutions were calculated. Figure 49 shows the axial resolution of the point source for various BMI for Mini-Bar and standard Total-Body J-PET but with and without acceptance angle criteria.

Figure 49 illustrate a comparison between standard (black), DOI (red), and Standard with 45^o

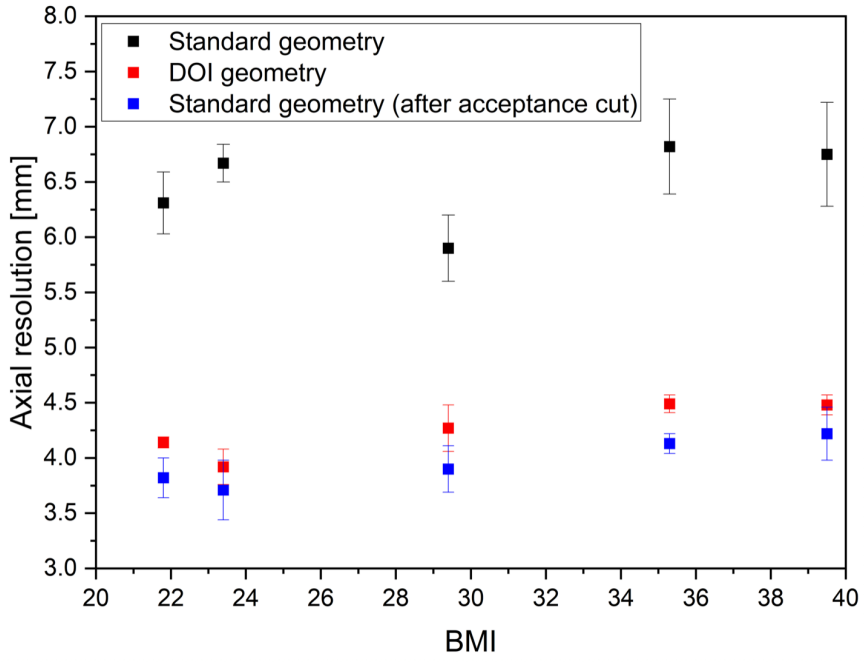

Figure 49: Dependance of the axial resolution of Standard (black) DOI geometry (red) and Standard after applying acceptance angle cut, to the BMI values of the phantoms.

AA(blue) based on their axial resolution as the function of the various BMI (in the form of cylindrical phantoms). As shown in Figure 49, applying AA cut over the coincidences to remove the contribution of the oblique coincidences in the reconstructed image caused an improvement in the axial resolution by the factor of ~ 2. While the Utilization of DOI geometry provided better axial resolution compared to the Standard geometry, the achieved results based on the AA had an optimized performance.

Among all of the investigated criteria, the 45^o acceptance angle (Figure 43 and Figure 49) had an optimized performance. For the case of this thesis, the lesion detectability of the Total-Body J-PET scanner, based on the standard geometry with 45 ^{o} of AA, will be investigated.

6.5 Lesion Detectability in XCAT Phantoms

In the presented thesis, 11 XCAT phantoms from both genders with various body mass index (BMI) and ages have been utilized. The BMI is a metric that represents the fatness of adults. This metric is utilized to classify people into different groups based on their fatness, as shown in Figure 50. The BMI is one of the major parameters in selecting the phantoms for this study. The characteristics of the utilized XCAT phantoms such as their ages, gender, BMI, etc., has been expressed in Table 2.

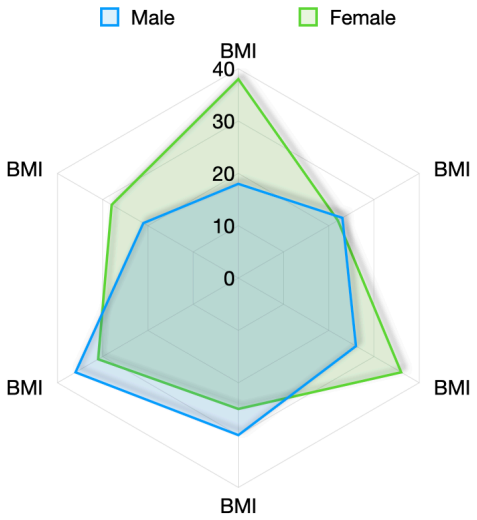

Category	BMI
Underweight	15-19.9
Normal weigth	20-24.9
Overweigth	25-29.9
Preobesity	-
Class I obesity	30-34.9
Class II obesity	35-39.9
Class III obesity	40

Figure 50: (Left) radar plot of the BMI values of the male (blue) and female (green) XCAT phantoms. (Right) numerical representation of the various category of the BMI and corresponding values.

Patient ID	Age (years)	Gender	Weight (Kg)	Height (cm)	Ethnicity
Pt-77	31	Male	77.9	185.2	Asian
Pt-150	18	Male	62.0	176.0	White
Pt-159	64	Male	106.1	175.3	White
Pt-163	67	Male	103.3	181.9	White
Pt-164	67	Male	89.9	178.5	White
Pt-171	64	Male	84.2	180.0	White
Pt-184	50	Male	120.0	177.8	White
Pt-71	27	Female	55.6	172.7	Black
Pt-143	52	Female	72.0	179.0	Withe
Pt-147	57	Female	105.5	165.1	Black
Pt-176	52	Female	86.0	153.0	White

Table 2: Characteristics of the utilizes XCAT phantoms.

6.6 lesion implementation within XCAT phantoms

XCAT software can generate a series of anthropomorphic digital phantoms without any abnormalities. The presence of the lesions in these series of phantoms is necessary to perform a reasonable study. For this purpose, XCAT software generates adjustable spherical lesions, while the amount of the activity, dimension, and location in the phantoms can be customized by the user. The induced lesions by XCAT software merge with the main phantom to produce a "cancerous phantom." Figure 51 is a XCAT generated 31 years old male phantom with the BMI of 22.71 Kg/m^2.

In the presented thesis, the liver has been chosen as the target organ to determine lesion de-

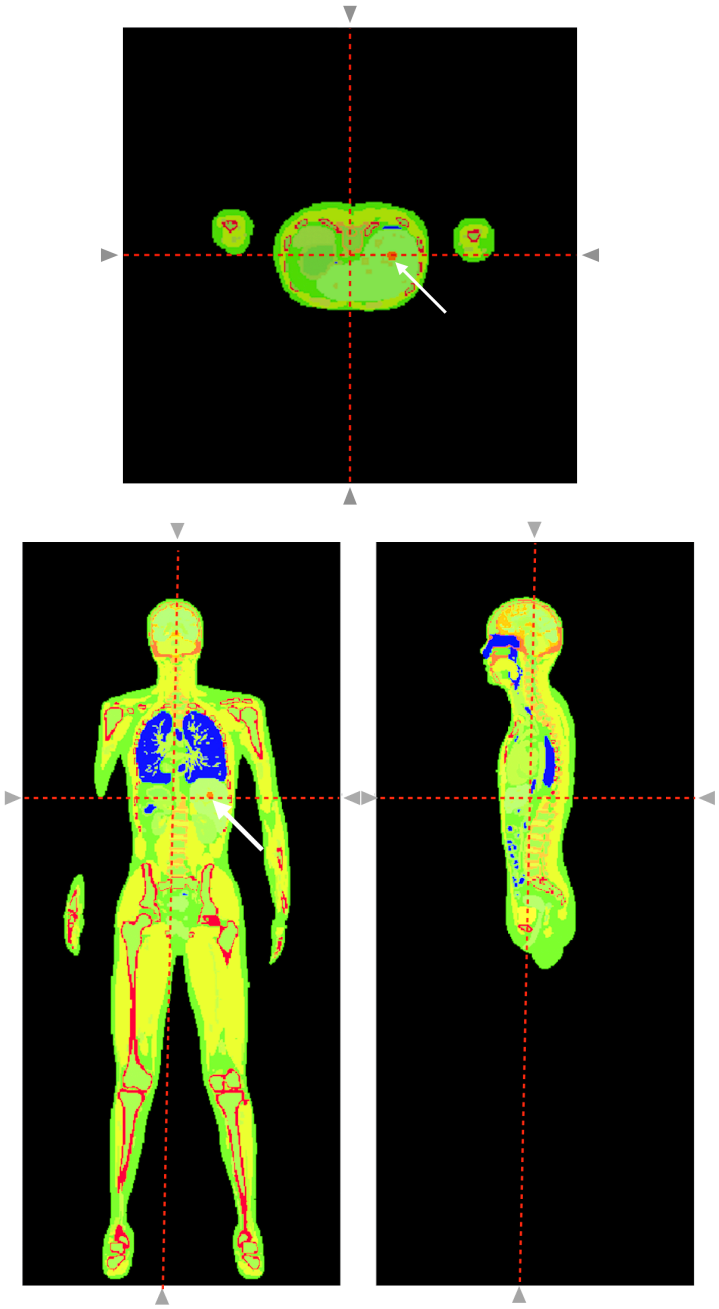

Figure 51: Illustration of the XCAT phantom in transverse (up) coronal (bottom left) and sagital (bottom right) planes.

tectability of the Total-Body J-PET. For this case, spherical lesions as the tumor have been implemented inside the liver of the XCAT phantoms. Figure 51 is an example illustration of the different visual cross sections where a red sphere is the lesions indicated by a white arrow inside the liver. This example (which is the activity distribution of the phantom) has been visualized by AMIDE software before the simulation to show the position of the lesion inside the body.

To investigate lesion detectability of the Total-Body J-PET, three series the simulation with various BMI of the XCAT phantoms, lesion dimension, and their uptake value, has been performed. To determine the dimensions of the detectable lesions, a 67 years old male XCAT phantom with a BMI of 28.22 (kg/m^2), which is the average BMI of the male in the EU [93], has been selected. The spherical lesions with a diameter of 5, 10, 15, 20, 25, and 30 mm and (TBR= 8:1) located in the liver have been simulated separately.

Figure 52 shows the total amount of the different types of coincidences (true, phantom scatter, detector scatter, and random coincidences) as a function of the dimensions of the lesions for mentioned above XCAT phantom. While larger lesions have a higher amount of accumulation of activity in a lesion area, as shown in Figure 52 this parameter does not have any influence on the percentage share of the coincidences in different simulations.

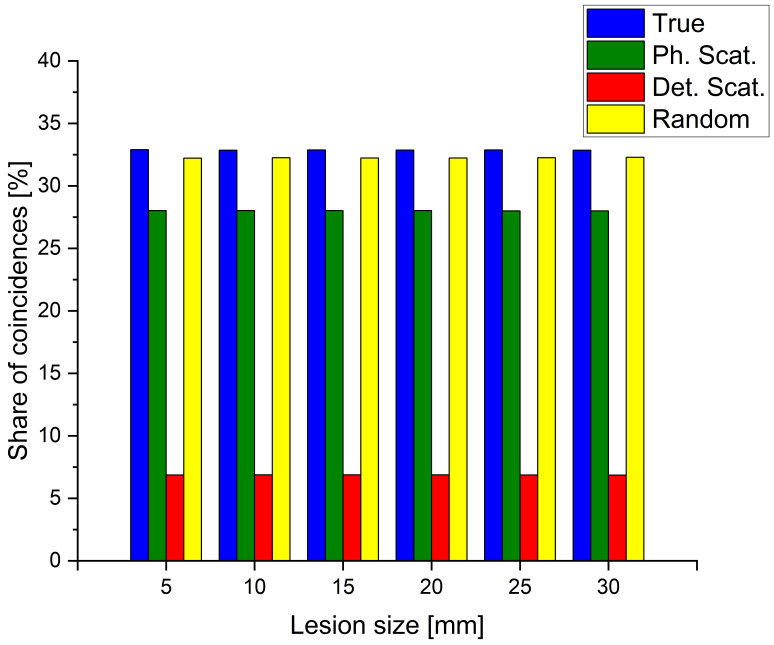

Figure 52: Share of different types of coincidences as the function of the lesion dimensions.

Figure 53 is an example of reconstructed image of this patient with the 30 mm lesions in the liver indicated by a white arrow. The figure shows the cross section of the reconstructed images in transverse (up), sagittal(bottom left) and coronal (bottom right).

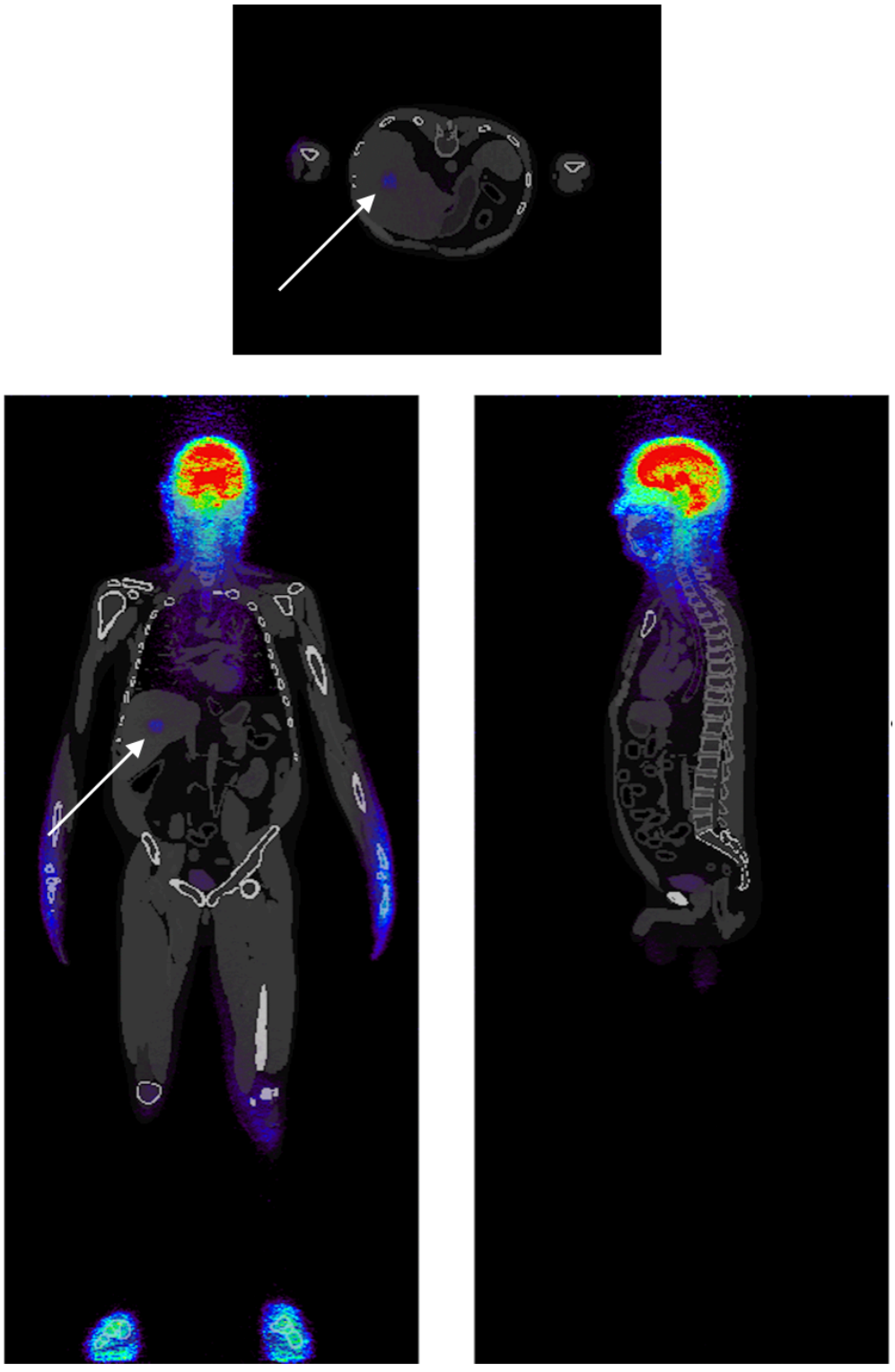

Figure 53: Illustration of the reconstructed image of a male XCAT phantom with a 30 mm lesion in the liver (marked by a white arrow).

The TBR values has been calculated based on the method explained in the 2.8 section (Tumor to background ratio). Figure 54, is an example illustration of how the region of interest has been chosen to include whole lesion's (red circle) and the tissue from liver (green circle) as the background.

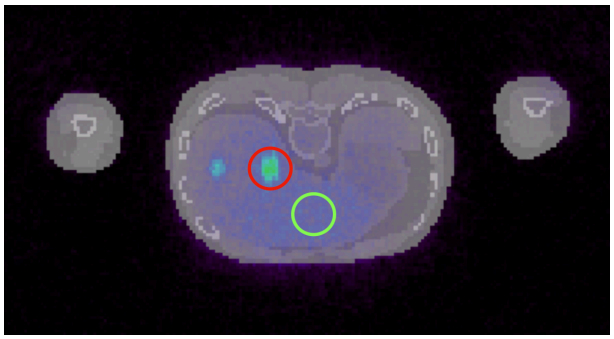

Figure 54: Illustration of a XCAT phantom (transverse image) with two lesions in its liver. One of the tumors selected (indicated by red circle) as the target, and a region from healthy part of the tissue (green circle) has been chosen to calculate TBR values.

Figure 55 shows the TBR values of the lesions with various dimensions. All the values are expressed as the mean (from a maximum of the intensity profiles in all corresponding voxels) ± standard deviation. To evaluate the effect of the number of iteration on the TBR values, the first, third, and sixth iteration has been investigated. The TBR values presented in Figure 55 are for the reconstructed image by contributing all detected coincidences without acceptance angle cut.

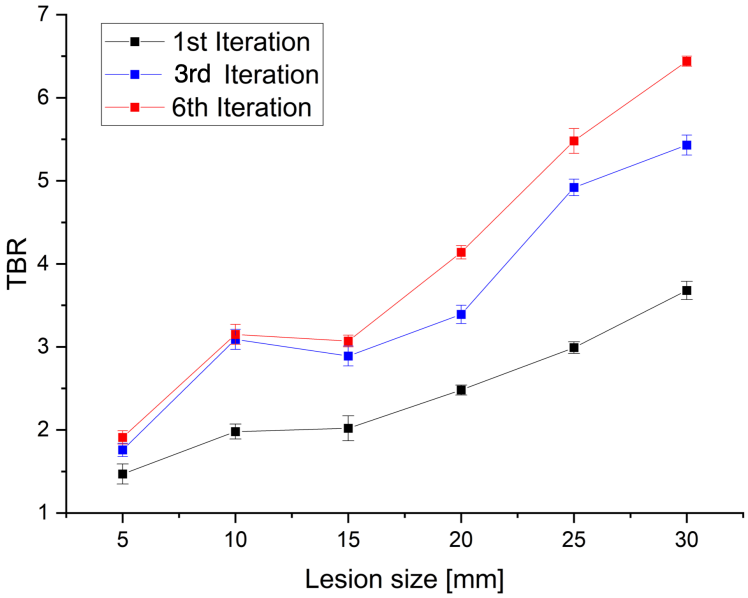

Figure 55: The TBR of the lesions with various diameters for 1st (black), 3rd (blue), and 6th (red) iterations without AA cut. In the presented Figure, lesions with the 8:1 ratio have been utilized.

As shown in Figure 55 all the lesions in the liver of the XCAT phantom with the BMI of 28.22

(kg/m^2) were visible and corresponding TBR values have been calculated. The results indicate that there is a direct relation between lesion size and TBR values. The presented results in Figure 55 also show that a higher number of iterations improves the TBR as well, especially in larger lesions.

To evaluate the effect of the acceptance angle (AA) cut on the TBR values of the lesions, the pre-reconstruction data of the phantom presented in Figure 55 has been used and a 45^o of AA cut was applied to the coincidences to remove the contribution of the most oblique coincidences in the image reconstruction. Figure 56 shows the achieved TBR values as the function of the size of the lesions for the male XCAT phantom with a BMI of 28.22 (kg/m^2).

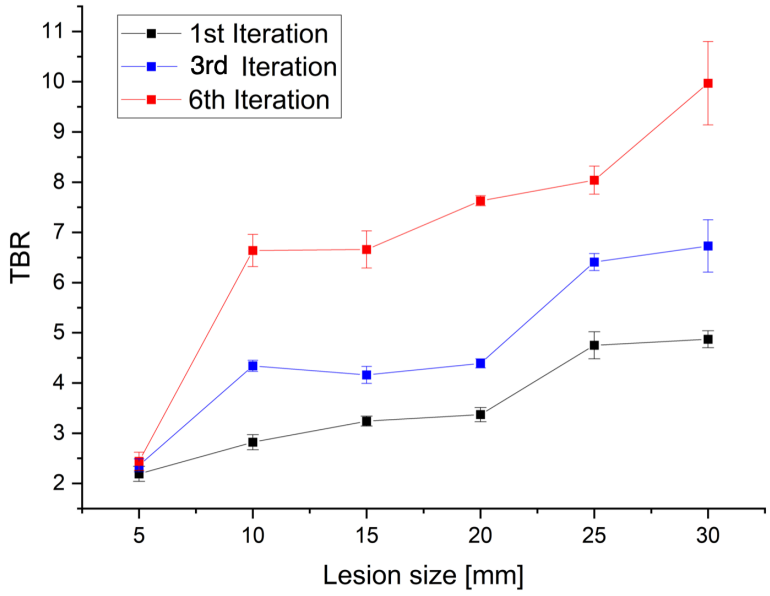

Figure 56: The TBR of the lesions with various diameters for 1st (black), 3rd (blue), and 6th (red) iterations with 45^o of AA cut. In the presented Figure, lesions with the 8:1 ratio have been utilized.

As shown in Figure 56, the higher number of iterations causes obtaining larger TBR values, same as the Figure55. However, the main advantage of applying 45^o of AA cut improves the TBR values in comparison to the results without AA cut.

Another series of these simulations have been performed to investigate lesion detectability of Total-Body J-PET by TBR ratio in XCAT phantoms with various BMI. For this case, three lesions with diameters of 5, 10, and 20 mm and a ratio of 8:1 (the ratio of the activity in spherical lesion to the activity of the liver) have been simulated. Figure 57 is the illustration from the raw file (before the GATE simulation and reconstruction) of the XCAT phantom, including three lesions with the 8:1 uptake ratio, indicated by the white arrows.

The reconstructed images after the GATE simulation, event selection, QETIR image reconstruction, and AMIDE visualization, have been shown in Figure 58 as an example, where white arrows

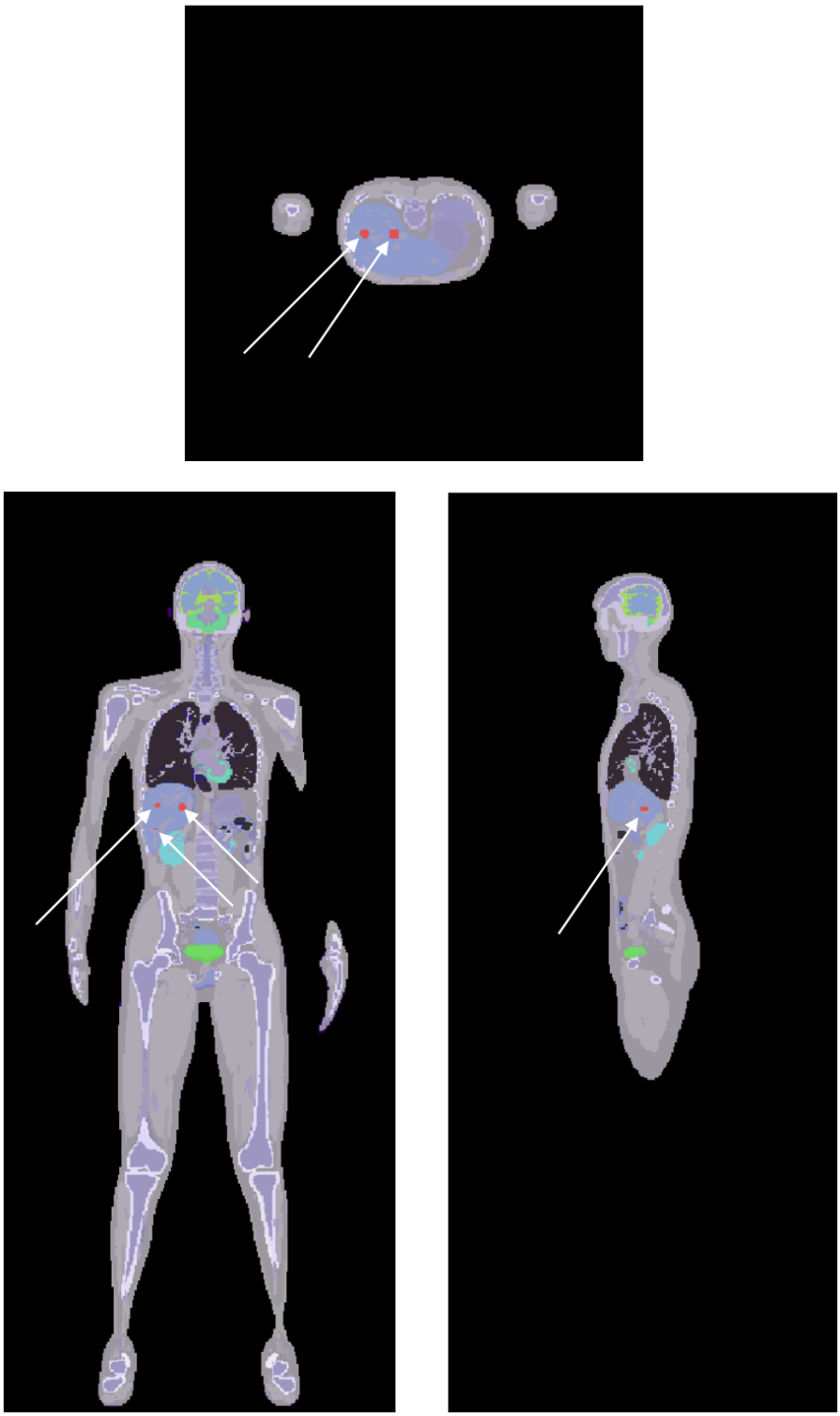

Figure 57: Illustration of the XCAT phantom in transverse (up) coronal (bottom left) and sagital (bottom right) planes, while three tumors in the liver indicated by white arrows.

have indicated the lesions. All the lesions have been implemented in XCAT phantom in the same sagittal plane to be able to visualize them at the same time.

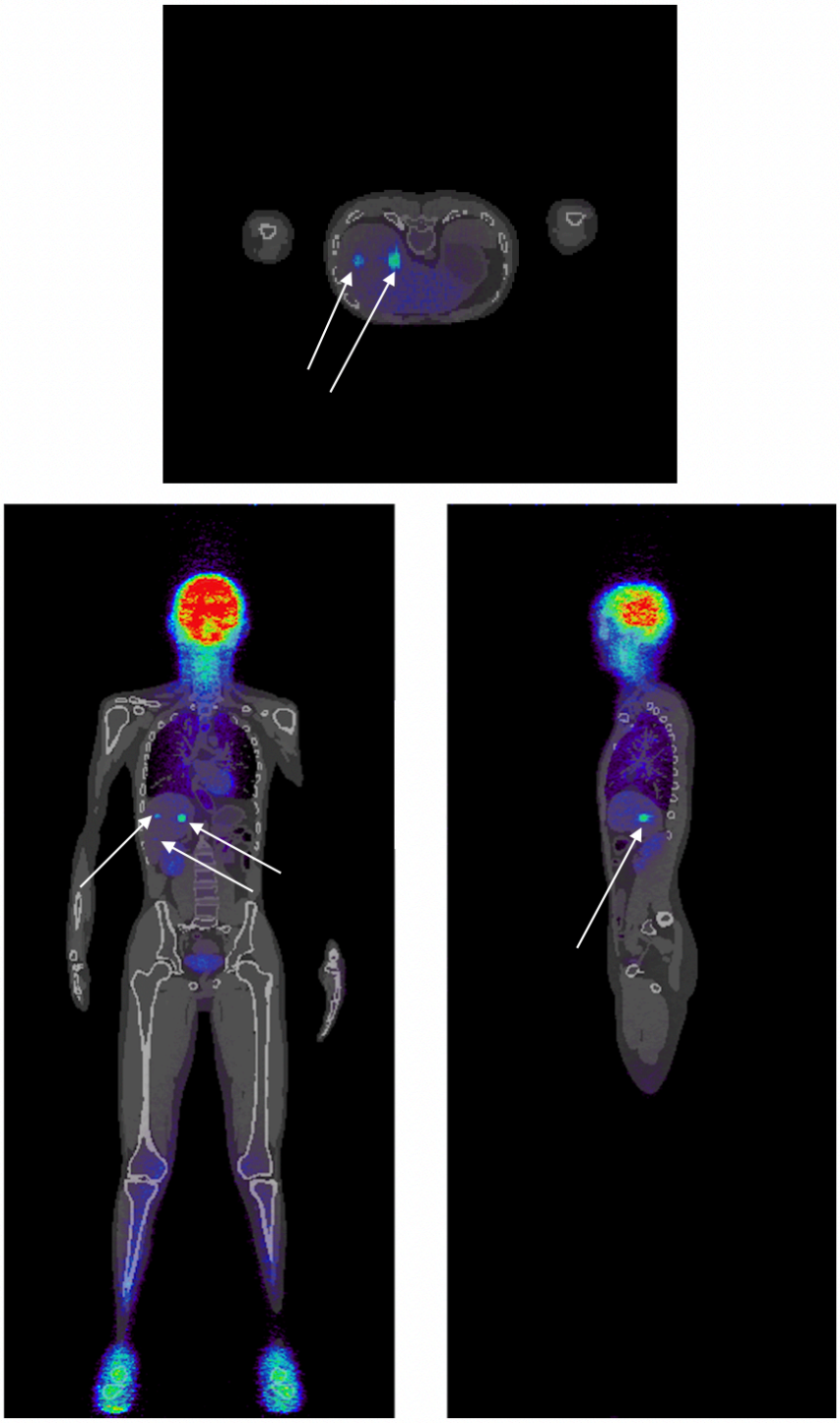

Figure 58: Illustration of the reconstructed image of a XCAT phantom and CT as the attenuation image, including three lesions with a diameter of 5, 10, and 20 mm in the liver with the 8:1 ratio .

Figure 59 shows the TBR values of the lesions in the XCAT phantoms with different BMI. As shown in Figure 59, there are no TBR values for the 5 mm diameter lesion for the XCAT phantoms with a higher BMI than 22.5 kg/m^2. This is due to the invisibility of the 5 mm lesions in the liver of the phantoms with larger BMI.

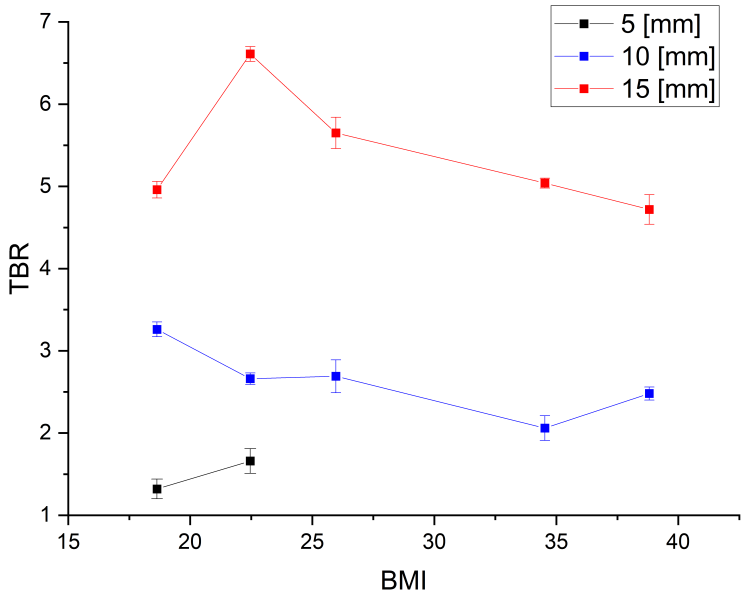

Figure 59: The TBR values of the lesions with the 8:1 uptake ratio in the Liver of the XCAT phantoms with different BMI.

The TBR values presented in Figure 59 have been calculated based on the 1st iteration of the reconstructed image without an acceptance angle cut. To investigate the effect of pre-selecting events in the lesion detectability of Total-Body J-PET additional reconstruction by considering optimized parameters has been performed. For this case, another series of the reconstruction after applying 45^o of AA has been performed. The TBR values of these reconstructions have been shown in Figure 60. As shown in Figure 60, applying AA cut, improved detectability of the lesions with 5 mm dimensions slightly than what has been presented in 59.

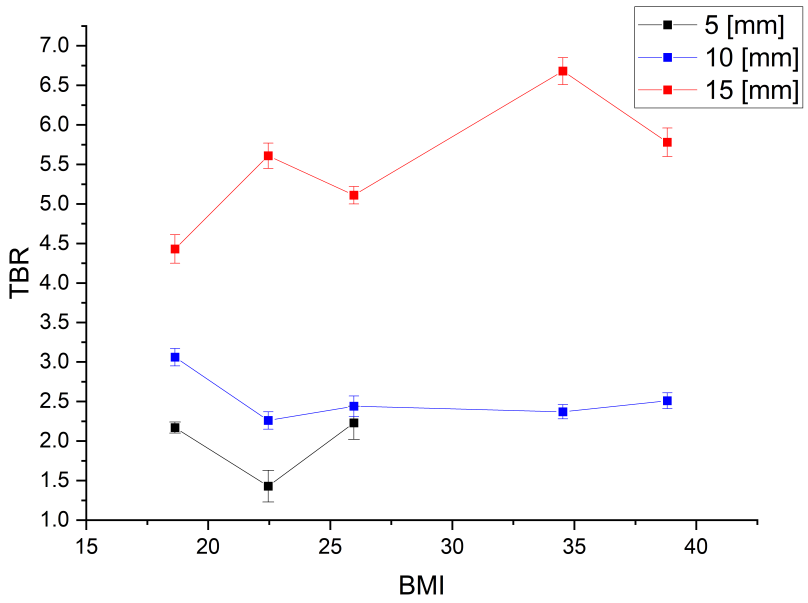

Figure 60: The TBR values of the lesions with the 8:1 uptake ratio in the Liver of the XCAT phantoms with different BMI after applying acceptance angle cut.

The effect of the higher number of the iteration in the obtained TBR values of the 5, 10, and 20 mm lesions in the XCAT phantoms with different BMI also has been investigated. Figure 61 and Figure 62 show the TBR values before and after applying the acceptance angle cut, respectively, in the third iteration of the reconstructed images.

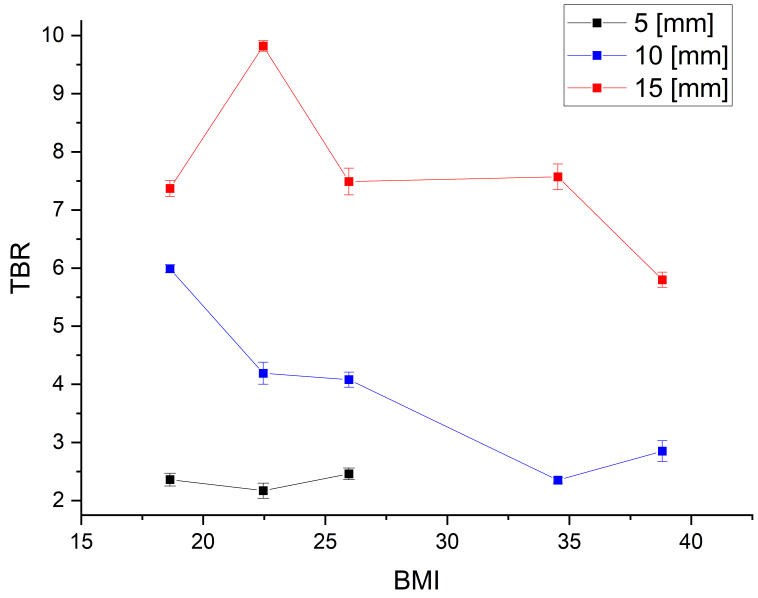

Figure 61: The TBR values of the lesions in the Liver of the XCAT phantoms with different BMI before applying the acceptance angle cut for the third iteration.

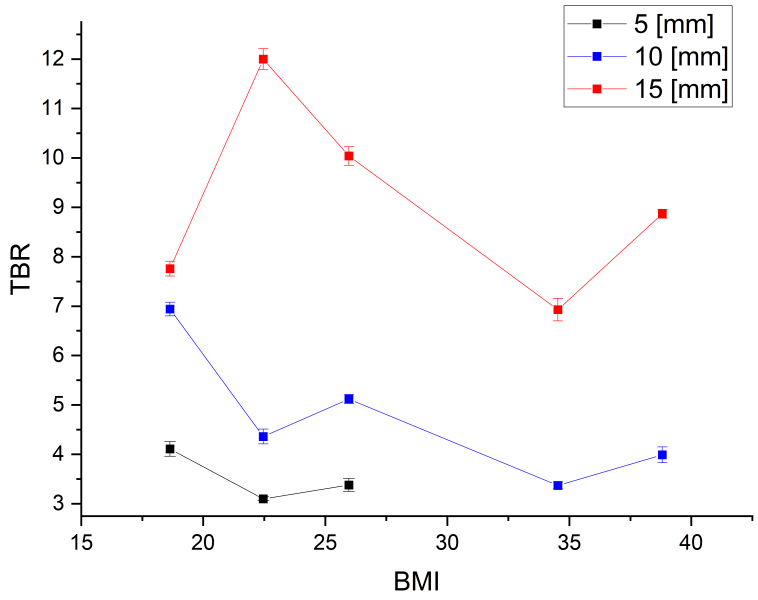

Figure 62: The TBR values of the lesions in the Liver of the XCAT phantoms with different BMI after applying of 45^{o} acceptance angle cut for the third iteration.

As shown in Figure 62, a higher number of the iteration provided the visibility of a 5 mm lesion in the XCAT phantom with a higher BMI. For this case, to investigate the visibility of the 5 mm lesions in the phantoms, the TBR values of the 6th iteration of the reconstructed image have been calculated before and after applying the acceptance angle cut, as shown in Figure 63 and Figure 64, respectively.

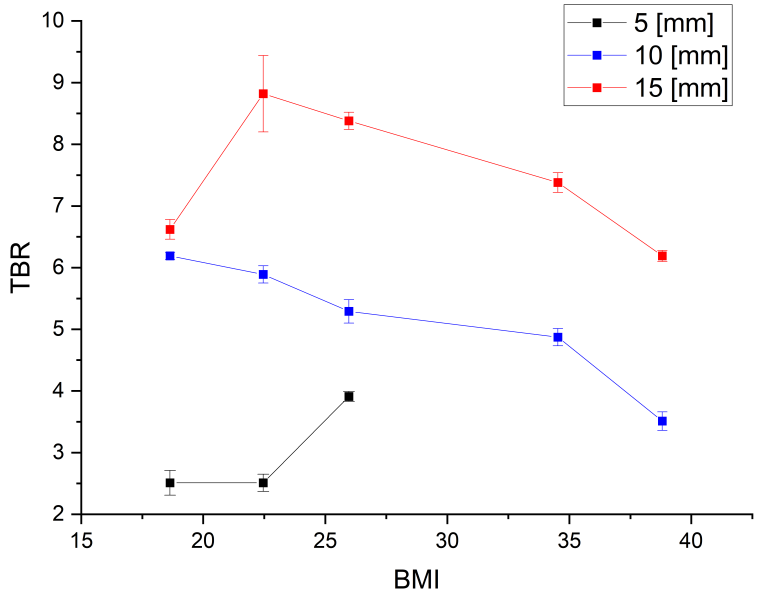

Figure 63: The TBR values of the lesions in the Liver of the XCAT phantoms with different BMI before applying the acceptance angle cut for the sixth iteration.

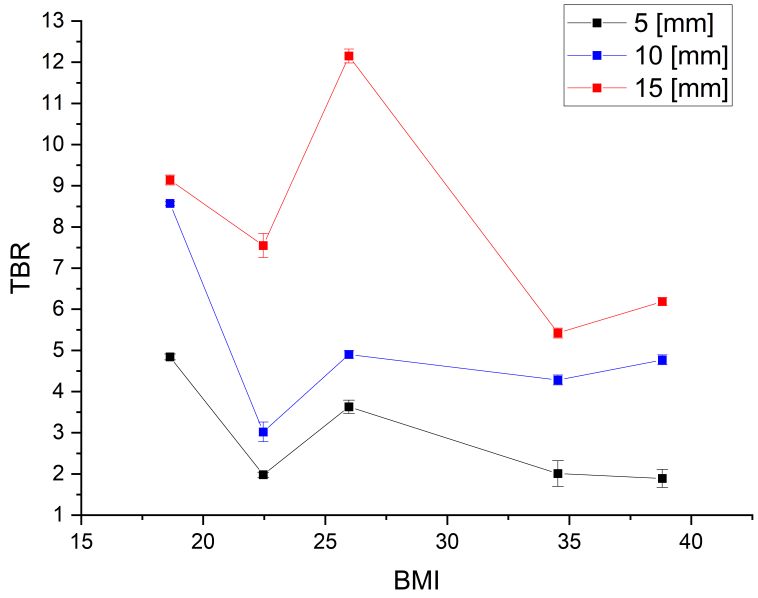

Figure 64: The TBR values of the lesions in the Liver of the XCAT phantoms with different BMI after applying of 45^o acceptance angle cut for the 6th iteration.

The performed investigation regarding lesion detectability of the Total-Body J-PET, in the XCAT phantoms with various BMI, emphasized the importance of the event selection. While 5 mm lesions as the smallest lesions in this thesis were not visible in the XCAT phantoms with higher BMI (Figure 59), applying event selection criteria along with proper reconstruction parameters, caused to detect of 5 mm lesions in all of the under investigating XCAT phantoms.

7 Summary and Discussion

The main aim of this thesis was to investigate the lesion detectability of the Total-Body J-PET by XCAT anthropomorphic digital phantom. This study has been conducted by the GATE simulation toolkit, advanced validated software for simulating medical imaging modalities. The GATE software is a simulation of all the physical processes and interactions between radiation and matter during real scan procedures. The results of the conducted simulation in this platform, contain all the necessary information such as the coordinates of the annihilations of electron-positron, the interaction of gamma quanta with scintillators, energy deposit, time, etc.

For the case of the presented thesis, all the output data has been stored as ROOT files, where all the data are in the form of histograms. These output files were raw file and there was needed to analyse them to apply predefined event selection criteria such as AA. For this case, the GOJA analyzer toolkit which has been developed by J-PET collaboration has been utilized. The list-mode file as the main output of the GOJA analyzer contains information on each coincidence such as interaction positions, time, deposited energy, type of the coincidences, etc. QETIR as the image reconstruction software requires list-mode data set. For this case, the list mode analyzed by GOJA software is used as the input file for QETIR image reconstruction software. All the reconstructed image has been visualized and analyzed by AMIDE software.

To enhance lesion detectability of the Total-Body J-PET scanner, sensitivity and spatial resolution as two critical parameters in the performance of the tomograph have been evaluated. While the large axial field-of-view (AFOV) in Total-Body PET scanners provides higher detector coverage along patients, these systems suffer from degradation of the axial resolution due to parallax error. Various acceptance angles cut as event selection criteria have been tested to overcome this issue (Figures 40, and 44). Among all the investigated values, 45^o of the acceptance angle had optimized performance by improving the axial resolution value by the factor of $\sqrt{2}$ (Figures 43 and 49).

The lesion detectability of the Total-Body J-PET scanner in XCAT phantom has been investigated both based on the diameter of the lesions (Figure 55) and the BMI of the phantom (Figure 59). As one of the most common organs with malignant lesions, the liver has been chosen as the host tissue for the lesions.

The detectability of the Total-Body J-PET as the function of the lesion size has been evaluated by utilization of an XCAT male phantom with a BMI of 28 kg/m^2 (as the average BMI of the male in the EU). Each lesion was implemented separately, three different iterations were evaluated, and the TBR value was calculated.

As shown in Table 3, applying the 45^o of acceptance angle increases the TBR ratio compared to without any acceptance angle scenario.

Applying the acceptance angle also significantly impacted the detection of the 5 mm lesions

	1st Iteration	3rd Iteration	6th Iteration
5 mm	+48.97 %	+34.09 %	+27.74%
10 mm	+42.42%	+40.45%	+110.79%
15 mm	+60.39%	+43.94%	+116.93%
20 mm	+35.89%	+29.49%	+84.29%
25 mm	+58.86%	+30.28%	+46.71%
30 mm	+32.34%	+23.94%	+54.81%

Table 3: Percentages of the change in the TBR ratios of the lesions with acceptance angle cut to all types of coincidences.

in the XCAT phantom with higher BMI. While 5 mm diameter lesions were not visible for the phantoms with BMI> 26(kg/m^2) (Figure 59), applying the 45 ^{o} of acceptance angle along with a higher number of iterations caused improved detection of the 5 mm lesions (as sub-centimeter grades lesions) even in the class II obesity patients (35<BMI<39.9) as shown in the Figure 64.

8 Conclusion

This thesis show that utilising extensive AFOV scanner than conventional PET, provide larger detector coverage and higher sensitivity as one of the key parameters in lesion detectability of PET tomographs (see Appendix A). The presented results by focusing on one of the challenges in large AFOV scanners which has been discussed as unknown DOI in Total-Body J-PET, investigated different event selection criteria (AA) and correction in the detector configurations. Based on the achieved results, AA in the standard Total-Body J-PET has been chosen as the final condition for rest of the research.

For the case of the presented thesis, series of human grade XCAT anthropomorphic phantoms with different BMI has been utilised to investigate lesion detectability of Total-Body J-PET. To determine lesion detectability of Total-Body J-PET in human grade XCAT phantom, the liver as the under investigation organ, has been chosen. For this reason, lesions with various dimensions (5-30 mm with the steps of five millimetres) has been implemented inside the liver with 8:1 tumor to background ratio.

Considering the challenges in detecting small lesions in obese people, 5, 10 and 15 mm spherical lesions in the series of XCAT phantoms with various range of the BMI has been investigated. The results show that utilization of 45 ^{o} AA cut along with higher number of the iteration, causes to detect the even 5 mm lesions in obese peoples by Total-Body J-PET.

As the final conclusion, the presented results in this thesis shows the ability of the Total-Body J-PET scanner in the detection of the lesions at their early stages. This feature, along with accurate localisation of tumors, can assess specialist to perform precise treatment planing and enhance survival rate of the patients.

List of Figures

References

[1] P Moskal, P Kowalski, R Shopa, and et al. Simulating nema characteristics of the modular total-body j-pet scanner—an economic total-body pet from plastic scintillators. *Phys Med Biol*, 66(17), 2021. doi.org/10.1088/1361-6560/ac16bd.

[2] P Moskal, S Niedzwiecki, T Bednarski, and et al. Test of a single module of the j-pet scanner based on plastic scintillators. *Nucl. Instr. and Meth. A*, 764:317–321, 2014. doi.org/10.1016/j.nima.2014.07.052.

[3] P Moskal and EŁ Stępień. Prospects and clinical perspectives of total-body pet imaging using plastic scintillators. *PET Clin.*, 15(4):439–452, 2020. doi.org/10.1016/j.cpet.2020.06.009.

[4] P Moskal, O Rundel, D Alfs, and Tet al. Bednarski. Time resolution of the plastic scintillator strips with matrix photomultiplier readout for j-pet tomograph. *Phys. Med. Biol.*, 61(5):2025–2047, 2016. doi.org/10.1088/0031-9155/61/5/2025.

[5] S Niedźwieckial, P Białasa, C Curceanu, and et al. J-pet: A new technology for the whole-body pet imaging. *Acta Phys. Pol. A*, 48(10):1567–1576, 2017. doi.org/10.5506/APhysPolB.48.1567.

[6] TN Seyfried and LC Huysentruyt. On the origin of cancer metastasis. *Crit Rev Oncog.*, 18(1-2):43–73, 2013. doi.org/10.1615/critrevoncog.v18.i1-2.40.

[7] YS Khan and A Farhana. *Histology, Cell*. In: StatPearls, Treasure Island (FL), 2022.

[8] HC Thoeny and BD Ross. Predicting and monitoring cancer treatment response with diffusion-weighted mri. *J Magn Reson Imaging*, 32(1):2–16, Jul 2010. doi.org/10.1002/jmri.22167.

[9] RD Badawi, H Shi, P Hu, and et al. First human imaging studies with the explorer total-body pet scanner. *J Nucl Med*, 60(3):299–303, 2019. doi.org/10.2967/jnumed.119.226498.

[10] BA Spencer, E Berg, JP Schmall, and et al. Performance evaluation of the uexplorer total-body pet/ct scanner based on nema nu 2-2018 with additional tests to characterize pet scanners with a long axial field of view. *J Nucl Med*, 62(6):861–870, Jun 2021. doi.org/10.2967/jnumed.120.250597.

[11] S Vandenberghe, P Moskal, and Karp JS. State of the art in total body pet. *EJNMMI Phys*, 7(35):1–33, 2020. doi.org/10.1186/s40658-020-00290-2.

[12] D Sarrut, M Bała, and et al. Advanced monte carlo simulations of emission tomography imaging systems with gate. *Phys Med Biol*, 66(10Tr03), 2021. doi.org/10.1088/1361-6560/abf276.

[13] D Costa, DAB Bonifácio, and et al. Optimization of gate simulations for whole-body planar scintigraphic acquisitions using the xcat male phantom with 177lu-dotatate biokinetics in a siemens symbia t2. *Phys Med.*, 42:292–297, Oct 2017. doi.org/10.1016/j.ejmp.2017.07.009.

[14] MEDISIP. Pet image reconstruction software qetir, 2022. http://wwwhttps://www.ugent.be/ea/ibitech/en/research/medisip/software-lab/software-lab13.htm, Last accessed on 2022-08-07.

[15] WHO. World health organization. (n.d.). cancer. world health organization. *https://www.who.int/news-room/fact-sheets/detail/cancer*, Retrieved August 8, 2022,.

[16] S Sarkar, G Horn, K Moulton, A Oza, S Byler, S Kokolus, and M Longacre. Cancer development, progression, and therapy: an epigenetic overview. *Int J Mol Sci*, 14(10):21087–21113, Oct 2013. doi.org/10.3390/ijms141021087.

[17] KK Dijkstra, CM Cattaneo, F Weeber, M Chalabi, J van de Haar, LF Fanchi, and et al. Generation of tumor-reactive t cells by co-culture of peripheral blood lymphocytes and tumor organoids. *J. Cell*, 174(6):1586–1598, Sep 2018. doi.org/10.1016/j.cell.2018.07.009.

[18] CB Blackadar. Historical review of the causes of cancer. *World J Clin Oncol*, 7(1):54–86, Feb 2016. doi.org/10.5306/wjco.v7.i1.54.

[19] SJ Jang, JM Gardner, and JY Roy. Diagnostic approach and prognostic factors of cancers. *Adv Anat Pathol*, 18(2):165–172, Mar 2011. doi.org/10.1097/PAP.0b013e31820cb39e.

[20] J Boutry, S Tissot, B Ujvari, JP Capp, M Giraudeau, AM Nedelcu, and et al. The evolution and ecology of benign tumors. *Biochim Biophys Acta Rev Cancer*, 1877(1):188643, Jan 2022. doi.org/10.1016/j.bbcan.2021.188643.

[21] AJ Perumpanani, JA Sherratt, and J Norbury. Mathematical modelling of capsule formation and multinodularity in benign tumour growth. *J. Nonlinearity*, 10(6):1599, 1997.

[22] M Fodor, F Primavesi, E Braunwarth, B Cardini, and et al. Indications for liver surgery in benign tumours. *Eur Surg*, 50(3):125–131, May 2018. doi.org/10.1007/s10353-018-0536-y.

[23] K Holtedahl. Challenges in early diagnosis of cancer: the fast track. *Scand J Prim Health Care*, 38(3):251–252, Sep 2020. doi.org/10.1080/02813432.2020.1794415.

[24] S Neragi-Miandoab, J Kim, and GJ Vlahakes. Malignant tumours of the heart: a review of tumour type, diagnosis and therapy. *Clin Oncol (R Coll Radiol)*, 19(10):748–756, Dec 2007. doi.org/10.1016/j.clon.2007.06.009.

[25] RL Anderson, T Balasas, J Callaghan, and et al. A framework for the development of effective anti-metastatic agents. *Nat Rev Clin Oncol*, 16:185–204, 2019. doi.org/10.1038/s41571-018-0134-8.

[26] N Jaffe. Chemotherapy for malignant bone tumors. *Orthop Clin North Am*, 20(3):487–503, Jul 1989.

[27] M Artac, H Bozcuk, M Ozdogan, and et al. Different clinical features of primary and secondary tumors in patients with multiple malignancies. *Tumori*, 91(4):317–320, Jul 2005.

[28] A Chambers, A Groom, and I MacDonald. Dissemination and growth of cancer cells in metastatic sites. *Nat Rev Cancer*, 2:563–572, 2002. doi.org/10.1038/nrc865.

[29] C Demoor-Goldschmidt and F de Vathaire. Review of risk factors of secondary cancers among cancer survivors. *Br J Radiol*, 92(1093):20180390, Sep 2019. doi.org/10.1259/bjr.20180390.

[30] P Humphrey. Gleason grading and prognostic factors in carcinoma of the prostate. *Mod Pathol*, 17:292–306, 2004. doi.org/10.1038/modpathol.3800054.

[31] SM Telloni. Tumor staging and grading: A primer. *Methods Mol Biol*, 1606:1–17, 2017. doi.org/10.1007/978-1-4939-6990-61.

[32] RJ Nijveldt, T Teerlink, MP Siroen, and et al. The liver is an important organ in the metabolism of asymmetrical dimethylarginine. *Clin Nutr*, 22(1):17–22, Feb 2002. doi.org/10.1054/clnu.2002.0612.

[33] S Kanungo, K Wells, T Tribett, and et al. Glycogen metabolism and glycogen storage disorders. *Ann Transl Med*, 6(24):474, Dec 2018. doi.org/10.21037/atm.2018.10.59.

[34] E Trefts, M Gannon, and DH Wasserman. The liver. *Current Biology*, 27(21):1147–1151, Nov 2017.

[35] F. Faure and et al. *SOFA: A Multi-Model Framework for Interactive Physical Simulation*. Payan, Springer, Berlin, Heidelberg, 2012.

[36] P Ginès, A Krag, JG Abraldes, E Solà, N Fabrellas, and PS Kamath. Liver cirrhosis. *Lancet*, 938(10308):1359–1376, Oct 2021. doi.org/10.1016/S0140-6736(21)01374-X.

[37] SR Abdel-Misih and M Bloomston. Liver anatomy. *Surg Clin North Am*, 9(4):643–653, Aug 2010. doi.org/10.1016/j.suc.2010.04.017.

[38] H Ellis. Anatomy of the liver. *Surgery (Oxford)*, 29(12):589–592, Dec 2011. doi.org/10.1016/j.mpsur.2011.09.012.

[39] A Karla, E Yetiskul, CJ Wehrle, and F Tuma. Physiology, liver. *StatPearls*, (30571059), Jan 2022.

[40] SK Asrani, H Devarbhavi, J Eaton, and PS Kamath. Burden of liver diseases in the world. *J Hepatol*, 70(1):151–171, Jan 2019. doi.org/10.1016/j.jhep.2018.09.014.

[41] WH Clark. Tumour progression and the nature of cancer. *Br J Cancer*, 64(4):631–634, Oct 1991. doi.org/10.1038/bjc.1991.375.

[42] JW Koten, JP Neijt, BA Zonnenberg, and et al. The difference between benign and malignant tumours explained with the 4-mutation paradigm for carcinogenesis. *Anticancer Res*, 13(4):1179–1182, Jul 1993.

[43] D Mathieu, V Vilgrain, AE Mahfouz, and et al. Benign liver tumors. *Magn Reson Imaging Clin N Am*, 5(2):255–288, May 1997.

[44] A Aguayo and YZ Patt. Liver cancer. *Clin Liver Dis*, 5(2):479–507, May 2001. doi.org/10.1016/s1089-3261(05)70175-6.

[45] MH Attwa and SA El-Etreby. Guide for diagnosis and treatment of hepatocellular carcinoma. *Magn Reson Imaging Clin N Am*, 7(12):1632–1651, Jun 2015. doi.org/10.4254/wjh.v7.i12.1632.

[46] PR Patel and De Jesus O. *CT Scan*. StatPearls Publishing, Treasure Island (FL), 2022.

[47] MR Oliva and S Saini. Liver cancer imaging: role of ct, mri, us and pet. *Cancer Imaging*, 4(Spec No A):42–46, May 2004. doi.org/10.1102/1470-7330.2004.0011.

[48] A Rutten and M Prokopi. Contrast agents in x-ray computed tomography and its applications in oncology. *Anticancer Agents Med Chem*, 7(3):307–316, May 2007. doi.org/10.2174/187152007780618162.

[49] Computed tomography (CT) scan for cancer. https://www.cancercenter.com/diagnosing-cancer/diagnostic-imaging/ct-scans last accessed 11 october 2022.

[50] B Moosavi, AS Shenoy-Bhangle, LL Tsai, and et al. Mri characterization of focal liver lesions in non-cirrhotic patients: assessment of added value of gadoxetic acid-enhanced hepatobiliary phase imaging. *Insights Imaging*, 11(101), May 2020. doi.org/10.1186/s13244-020-00894-3.

[51] M Ghadimi and A Sapra. Magnetic resonance imaging contraindications. *[Updated 2022 May 8]. In: StatPearls [Internet]. Treasure Island (FL): StatPearls Publishing; 2022 Jan-.*

[52] R Lo Gullo, I Daimiel, C Rossi Saccarelli, P Gibbs, and et al. Improved characterization of sub-centimeter enhancing breast masses on mri with radiomics and machine learning in brca mutation carriers. *Eur Radiol*, 30(12):21087–21113, Dec 2020. doi.org/10.1007/s00330-020-06991-7.

[53] A Alavi, TJ Werner, EŁ Stępień, and P Moska. Unparalleled and revolutionary impact of pet imaging on research and day to day practice of medicine. *Bio-Algorithms and Med-Systems*, 17(4):203–212, 2021. doi.org/10.1515/bams-2021-0186.

[54] T Saga, K Yoshikawa, and K Ishizu. Positron emission tomography: basic principle and radionuclides/probes for metabolic/functional analysis. *Rinsho Byori*, 55(7):630–638, Jul 2007.

[55] DW Townsend. Positron emission tomography/computed tomography. *Semin Nucl Med.*, 38(3):152–166, May 2008. doi: 10.1053/j.semnuclmed.2008.01.003.

[56] PE Kinahan, DW Townsend, T Beyer, and D Sashin. Attenuation correction for a combined 3d pet/ct scanner. *Med Phys.*, 25(10):2046–2053, Oct 1998. doi: 10.1118/1.598392.

[57] MA. Ashraf and A. Goyal. *Fludeoxyglucose (18F)*. StatPearls, Treasure Island (FL), 2022. PMID: 32491585.

[58] W Lei, DX Zeng, B Zhang, YH Zhu, and et al. (18)f-fdg pet-ct: a powerful tool for the diagnosis and treatment of relapsing polychondritis. *Br J Radiol*, 89(1057):20150695, Nov 2016. doi.org/10.1259/bjr.20150695.

[59] L Cole, MN Stewart, and et al. Radiosyntheses using fluorine-18: the art and science of late stage fluorination. *Curr Top Med Chem.*, 14(7):875–900, Dec 2014. doi:10.2174/1568026614666140202205035.

[60] J Castelli, B De Bari, A Depeursinge, and et al. Overview of the predictive value of quantitative 18 fdg pet in head and neck cancer treated with chemoradiotherapy. *Crit Rev Oncol Hematol.*, 108:40–51, Dec 2016. doi: 10.1016/j.critrevonc.2016.10.009.

[61] J Ermert and B Neumaier. *Radiopharmaceutical Chemistry*. Example, 2019.

[62] M Conti and L Eriksson. Physics of pure and non-pure positron emitters for pet: a review and a discussion. *EJNMMI Phys*, 3(8), 2016. doi.org/10.1186/s40658-016-0144-5.

[63] S Adler, J Seidel, and et al. Minimum lesion detectability as a measure of pet system performance. *EJNMMI Phys.*, 14(1(13)), Dec 2007. doi: 10.1186/s40658-017-0179-2.

[64] R García-Figueiras, S Baleato-González, AR Padhani, and et al. How clinical imaging can assess cancer biology. *Insights Imaging*, 10(1):30830470, Mar 2019. doi.org/10.1186/s13244-019-0703-0.

[65] H Bal, L Guerin, ME Casey, M Conti, and et al. Improving pet spatial resolution and detectability for prostate cancer imaging. *Phys Med Biol*, 59(12):4411–4426, Aug 2014. doi.org/10.1088/0031-9155/59/15/4411.

[66] B Kunnen, C Beijst, M Lam, and et al. Comparison of the biograph vision and biograph mct for quantitative 90y pet/ct imaging for radioembolisation. *EJNMMI Phys.*, 7(1):32130554, Mar 2020. doi.org/10.1186/s40658-020-0283-6.

[67] K Gong, SR Cherry, and J Qi. On the assessment of spatial resolution of pet systems with iterative image reconstruction. *Phys Med Biol*, 61(5):193–202, Mar 2016. doi.org/10.1088/0031-9155/61/5/N193.

[68] WW Moses. Fundamental limits of spatial resolution in pet. *Nucl Instrum Methods Phys Res A*, 648(1):236–240, Aug 2011. doi: doi:10.1016/j.nima.2010.11.092.

[69] K Murakami and M Murakami. Fdg-pet for hepatobiliary and pancreatic cancer: Advances and current limitations. *World J Clin Oncol*, 2(5):229–236, 2011. doi: 10.5306/wjco.v2.i5.229.

[70] JS Karp, R Freifelder, MJ Geagan, and et al. Three-dimensional imaging characteristics of the head penn-pet scanner. *J Nucl Med.*, 38(4):636–43, Apr 1997. PMID: 9098216.

[71] P Moskal, D Kisielewska, Z Bura, and et al. Performance assessment of the 2gamma positronium imaging with the total-body pet scanners. *EJNMMI Phys.*, 7(44), 2020. doi.org/10.1186/s40658-020-00307-w.

[72] YQ Zhang, PC Hu, RZ Wu, and et al. The image quality, lesion detectability, and acquisition time of 18f-fdg total-body pet/ct in oncological patients. *Eur J Nucl Med Mol Imaging*, 47:2507–2515, 2020. doi.org/10.1007/s00259-020-04823-w.

[73] S Cherry, T Jones, J Karp, and et al. Total-body pet: Maximizing sensitivity to create new opportunities for clinical research and patient care. *J Nucl Med*, 59(1):3–12, 2018. doi.org/10.2967/jnumed.119.226498.

[74] JP He, Y Hao, M Li, J Wang, and et al. Tumor-to-background ratio to predict response to chemotherapy of osteosarcoma better than standard uptake values. *Orthop Surg.*, 6(2):145–153, May 2014. doi.org/10.1111/os.12102.

[75] JM Rogasch, IG Steffen, F Hofheinz, S Hofheinz, C Furth, and et al. The association of tumor-to-background ratios and suvmax deviations related to point spread function and time-of-flight f18-fdg-pet/ct reconstruction in colorectal liver metastases. *EJNMMI Research*, 5(31), 2015. doi.org/10.1186/s13550-015-0111-5.

[76] T Utsunomiya, K Ogawa, N Funamizu, K Sakamoto, and et al. The tumor-to-liver ratio of the standardized uptake value is a useful fdg-pet/ ct parameter for predicting malignant intraductal papillary mucinous neoplasm of the pancreas. *Ann Gastroenterol Surg.*, 00:1–9, Feb 2022. doi.org/10.1002/ags3.12562.

[77] I Gutin. In bmi we trust: Reframing the body mass index as a measure of health. *Ann Gastroenterol Surg.*, 16(3):256–271, Aug 2018. doi.org/10.1057/s41285-017-0055-0.

[78] BMI Weight Chart shradha madan's dietary clinic. (n.d.). http://www.dietaryclinic.co.in last accessed 2 october 2022.

[79] P Moskal and E Stepien. New trends in theranostics. *Bio-Algorithms and Med-Systems*, 17(4):199–202, 2021. doi.org/10.1515/bams-2021-0204.

[80] P Moskal, P Rzaca, and E Stepien. Novel biomarker and drug delivery systems for theranostics – extracellular vesicles. *Bio-Algorithms and Med-Systems*, 17(4):301–399, 2021. doi.org/10.1515/bams-2021-0183.

[81] P Moskal, A Gajos, M Mohammad, and et al. Testing cpt symmetry in ortho-positronium decays with positronium annihilation tomography. *Nat Commun*, 5658, 2021. doi.org/10.1038/s41467-021-25905-9.

[82] P Moskal, K Dulski, N Chung, and et al. Positronium imaging with the novel multiphoton pet scanner. *Sci. Adv.*, 7(42):4394, 2021. doi.org/10.1126/sciadv.abh4394.

[83] P Moskal, D Kisielewska, C Curceanu, and et al. Feasibility study of the positronium imaging with the j-pet tomograph. *Phys Med Biol*, 7(64):055017, 2019. doi.org/10.1088/1361-6560/aafe20.

[84] P Moskal, N Krawczyk, B Hiesmayr, and et al. Feasibility studies of the polarization of photons beyond the optical wavelength regime with the j-pet detector. *Eur. Phys. J. C*, 78(970), 2018. doi.org/10.1140/epjc/s10052-018-6461-1.

[85] M Dadgar, S Parzych, and F Tayefi. A simulation study to estimate optimum lor angular acceptance for the image reconstruction with the total-body j-pet. *In: Smith, Y. (ed.) Medical*

Image Understanding and Analysis Lecture Notes in Computer Science, Lect. Notes Comput. Sci., pages 189–200, 2021. doi.org/10.1007/978-3-030-80432-9-15.

[86] Gate Collaboration. Opengate. (n.d.).gate/gatematerials.db at develop · opengate/gate. *https://github.com/OpenGATE/Gate/blob/develop/GateMaterials.db*, Retrieved September 29, 2022,.

[87] M Dadgar and P Kowalski. Gate simulation study of the 24-module j-pet scanner: Data analysis and image reconstruction. *Acta Phys. Pol. B*, 50(1):309–315, 2020. doi.org/10.5506/APhysPolB.51.309.

[88] M Dadgar and P Kowalski. Gate simulation study of the 24 modular j-pet scanner: Data analysis and image reconstruction. *Acta Phys. Pol. B*, 51(1):309–315, 2017. doi.org/10.5506/APhysPolB.51.309.

[89] Quantitative Emission Tomography Iterative Reconstruction at the MEDISIP. https://ugent.be/ea/ibitech/en/research/medisip/software-lab/software-lab13.htm last accessed 26 august 2022.

[90] AM Loening and SS Gambhir. Amide: a free software tool for multimodality medical image analysis. *Mol Imaging*, 2(3):131–137, Jul 2003. doi.org/10.1162/153535003322556877.

[91] S Cherry and et al. Abstracts of the total body pet conference 2018, pp1-2. *EJNMMI, Ghent, Belgium*, 2018.

[92] X Zhang, Z Xie, and et al. Total-body dynamic reconstruction and para- metric imaging on the uexplorer. *Journal of Nuclear Medicine*, 61(2):285–291, 2019. doi.org/10.2967/jnumed.119.230565.

[93] WHO EUROPEAN REGIONAL OBESITY REPORT 2022. https://apps.who.int/iris/bitstream/handle/10665/353747/9789289057738-eng.pdf last accessed 26 august 2022.

cite natbib

Appendix

Appendix A

The high price of Total-Body PET scanners encouraged trials to find alternative cost-efficient solutions. Utilization of the BGO scintillation crystals instead of the LYSO or LSO due to the lower cost is one of the solutions. But due to the radial configuration of the detectors in conventional tomographs, this solution only reduces the price of the scintillator crystals. At the same time, the number of electronics is similar [3]. While utilization of the BGO instead of the LYSO reduces the portion of the price related to the scintillation crystals, the number of the SiPM and electronic units remain the same, and the final construction and maintenance price will not change significantly. The other recently suggested approach is the utilization of the sparse configuration in tomographs, where the total number of detectors reduces by half due to the adding intervals between detectors in axial axes as shown in Figure 65.

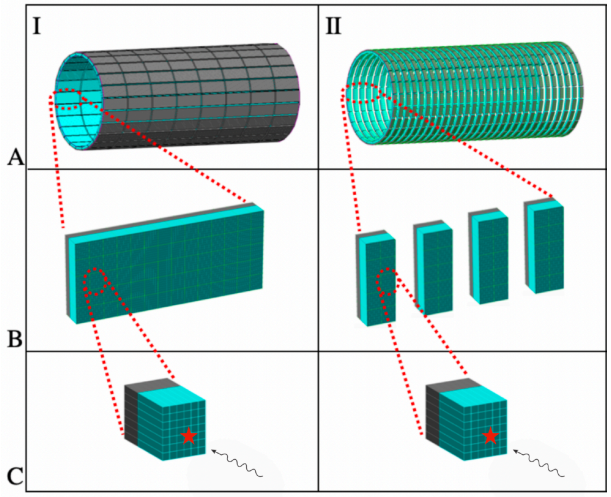

Figure 65: GATE visualisations of (I) uEXPLORER scanner with 194.7 cm AFOV and (II) sparse confirmation with 194.7 cm AFOV.

In the best possible scenario, this solution reduces final construction cost by half while providing nonuniform sensitivity due to its specific configuration. Since the sensitivity of the scanners represents their ability to detect smaller lesions, a series of simulations to compare the sensitivity of the existing and under investigation Total-Body PET systems has been performed. Figure 66 shows the sensitivity profiles of all existing and under investigation Total-Body PET scanners by performing GATE simulation with a 2.5 m line source located at their central axial axes.

Utilization of the acceptance angle cut is necessary for crystal-based Total-Body PET scanners such as uEXPLORER. As shown in Figure 65, these types of scanners are composed of several rings located next to each other to provide larger axial FOV. For this case, non-J-PET-based Total-Body scanners apply ring-wise cut to improve their axial resolution.

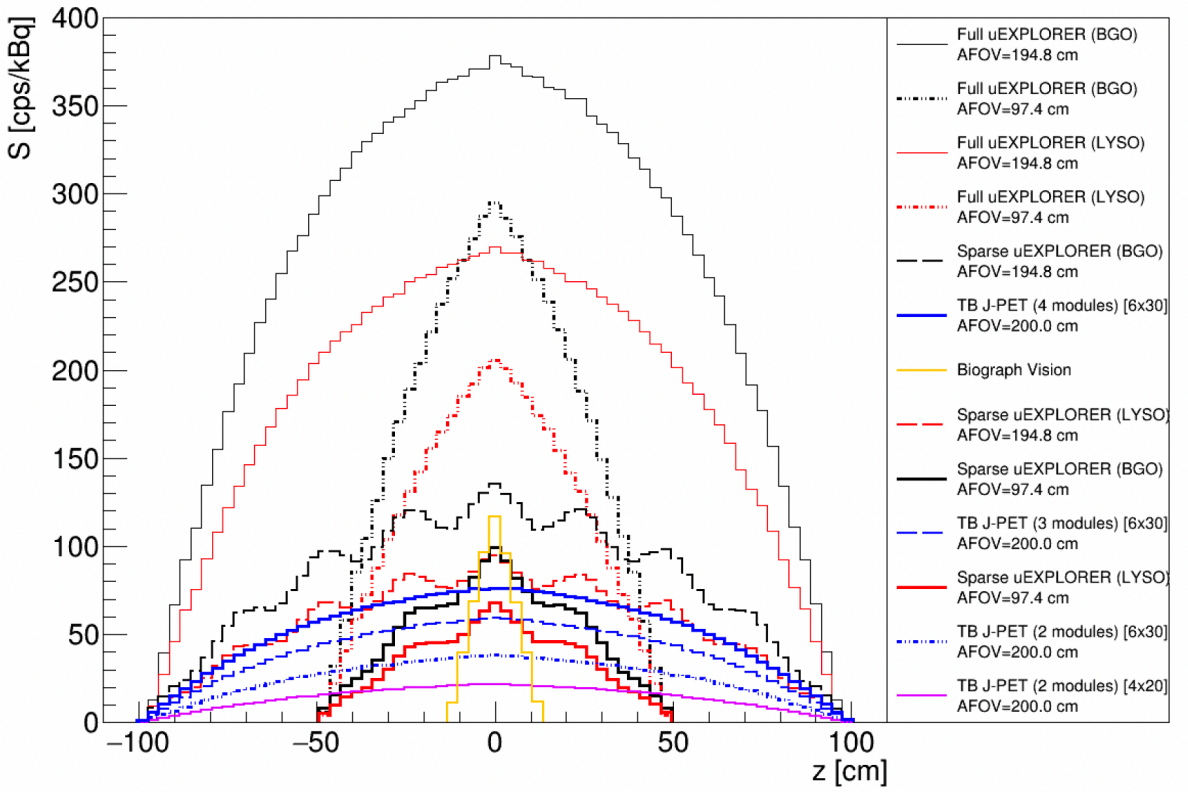

Figure 66: Sensitivity profiles of the all possible and under investigation Total-Body PET scanners.

The effect of applying cut on the scanner presented in Figure 66 has been investigated as well. Figure 67 shows the sensitivity profiles of these scanner after applying cut to remove most oblique coincidences.

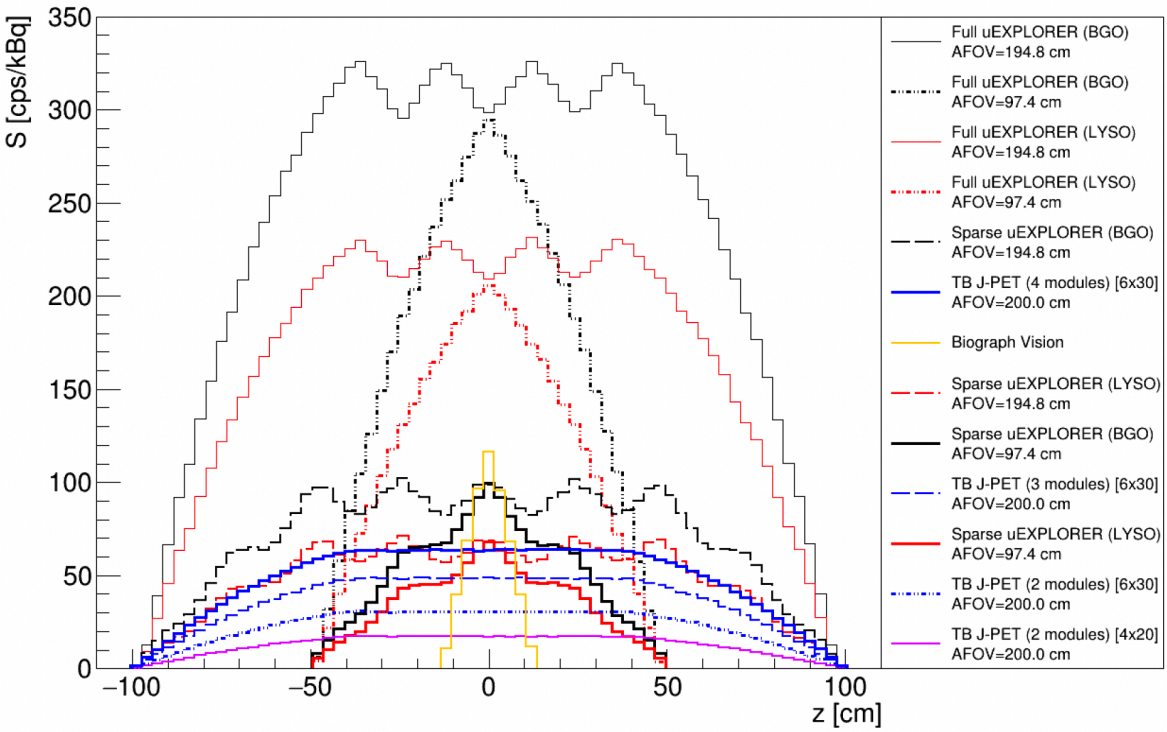

Figure 67: Sensitivity profiles of the all possible and under investigation Total-Body PET scanners after applying cut over the oblique coincidences.